POLITECNICO DI TORINO

Corso di Laurea Magistrale in

Ingegneria Biomedica

Tesi di Laurea Magistrale

Additive Manufacturing of hydroxyapatite scaffolds for bone repair

Relatori

Prof. Francesco Baino

Prof.ssa. Enrica Vernè

Dr. Martin Schwentenwein

…….

…….

…….

Candidato

Giulia Magnaterra

……..

Luglio 2020

A Christine & Giotto

Index

Abstract

Negli ultimi decenni, la rigenerazione del tessuto osseo (Bone Tissue Engineering, BTE) è stato uno dei temi di ricerca più discussi nel campo della medicina rigenerativa (Tissue Engineering, TE).
L'osso è in grado di rigenerarsi da solo, ma, in presenza di estesi difetti ossei dovuti a traumi, rimozione di tumori o malattie congenite, potrebbe essere necessario ricorrere all'intervento chirurgico e inserire un innesto osseo per promuoverne la guarigione.
Ogni anno, più di 2,2 milioni di persone in tutto il mondo necessitano di essere sottoposti a interventi chirurgici riguardanti la rigenerazione di tessuto osseo.
Attualmente sia gli innesti di tipo naturale che sintetico sono molto utilizzati, anche se un materiale propriamente ideale per l'innesto ancora non esiste.
Generalmente, gli innesti naturali mostrano diversi vantaggi, tra cui buona biocompatibilità e osteoconduttività, ma allo stesso tempo sono caratterizzati da svantaggi intrinseci (basso numero di donatori, rischio di risposta immunologica e questioni etico-religiose) che ne limitano l'uso.
Laddove non è possibile utilizzare l'innesto natuale, gli innesti ossei sintetici, comunemente noti con il nome di scaffolds o matrici sintetiche, possono rappresentare una buona alternativa.
Gli scaffolds sono strutture 3D porose in grado di imitare la matrice extracellulare (ECM) dell'osso naturale; devono fornire un modello strutturale in grado di resistere alle condizioni di carico fisiologico, promuovendo al contempo la crescita e la proliferazione cellulare attraverso specifiche interazioni materiale/ambiente.
La biodegradabilità, la porosità interconnessa, la dimensione controllata dei pori, l'architettura trabecolare e il materiale di partenza sono solo alcuni dei principali requisiti che uno scaffold per BTE deve possedere pr soddisfare i tempi e la qualità della rigenerazione ossea.

Rispetto ai biomateriali utilizzabili per la produzione di matrici ossee, particolare attenzione è attualmente rivolta ai fosfati di calcio (CaPs); tra questi, l'idrossiapatite sintetica (HA, $Ca_{10}(PO_4)_6(OH)_2$) risulta una delle più apprezzate grazie alla sua somiglianza con l'HA naturale, che costituisce oltre il 60% della matrice ossea inorganica. Tra i vantaggi derivanti dall'utilizzo dell'HA come materiale da impalcatura, la sua eccellente osteoconduttività e le sue proprietà bioattive sono quelle principalmente coinvolte nella promozione dell'adesione cellulare, della proliferazione e della sintesi di nuovi tessuti.
Inoltre, da prove sperimentali risulta che le strutture in HA hannoo proprietà meccaniche più elevate, rispetto ad altre bioceramiche, come i vetri bioattivi o il fosfato tricalcico (TCP); in alcuni casi però, il suo lento tasso di degradazione può essere incompatibile con i requisiti dell'impianto.

Tecniche di Additive Manufacturing (AM) conosciute anche con il nome di Rapid Prototyping (RP) giocano un ruolo importante nella creazione di impalcature altamente porose e interconnesse, e garantiscono una maggiore riproducibilità e affidabilità del processo produttivo rispetto alla produzione tradizionale di impalcature.
Le tecniche RP sono caratterizzate da una costruzione layer-by-layer della struttura 3D, seguendo un modello software di progettazione assistita (computer-aided design (CAD) software model).

Esistono molte tecniche AM adatte alla lavorazione di materiali ceramici, come: select laser sintering (SLS), 3D printing (3DP), direct ink writing (DIW), stereolithography (SLA) and digital light processing (DLP) based on SLA.
La litografia, in combinazione con la DLP, costruisce gli oggetti 3D strato per strato polimerizzando selettivamente una sospensione liquida fotosensibile contenente particelle ceramiche omogeneamente disperse.
Viene creato un singolo strato alla volta attraverso un Digital Micromirror Device (DMD) che, accoppiato ad un sistema di illuminazione, si comporta come una maschera dinamica.
Il metodo di stampa permette di ottenere il cosiddetto "green body" formato da polveri ceramiche e da una matrice organica che verrà eliminata attraverso un trattamento ad alta temperatura (sinterizzazione) durante la fase di post-processing.
I modelli CAD possono essere creati sulla base di immagini ottenute da microtomografia (micro-computed tomography, μ-CT) o da risonanza magnetica (MRI), le quali permettono di ottenere modelli unici del difetto da trattare, quindi specifici per il paziente.
È anche possibile produrre scaffolds su larga scala, commercializzabili e standardizzati, utilizzando modelli CAD che replicano forme regolari 3D ottenute dalla ripetizione di unità cellulari di geometria e proprietà note, disposte in un array tridimensionale. Tuttavia, questo approccio porta solitamente all'ottenimento di modelli grezzi che difficilmente replicano l'effettiva architettura trabecolare dell'osso.

Lo scopo del presente lavoro sperimentale ha previsto la produzione di scaffolds porosi in HA che fossero in grado di imitare l'architettura trabecolare dell'osso spongioso, garantendo al contempo un'elevata standardizzazione e riproducibilità del processo di fabbricazione.
Per raggiungere tale obbiettivo ci si è serviti della tecnica DLP basata su SLA, ed è stato utilizzato un modello CAD ottenuto dalla ricostruzione microtomografica dell'architettura 3D di una spugna commerciale di poliuretano.
Il processo di stampa ha portato alla produzione di strutture 3D (Figura 0) che presentavano un'elevata affinità morfologica e compositiva con il tessuto nativo.

Presso l'azienda austriaca Lithoz GmbH sono stati prodotti scaffolds ceramici di geometria cubica e cilindrica, utilizzando il loro sistema stereolitografico CeraFab 7500.
Durante la permanenza in Lithoz, è stata dedicata particolare attenzione anche alla realizzazione e alla caratterizzazione del materiale di partenza (slurry LithaBone 480E). In particolar modo, è stata valutata la sua stabilità rispetto ad un periodo di 5 settimane, durante le quali sono state monitorate le proprietà reologiche, la densità relativa, la massima resistenza alla flessione e la tendenza all'agglomerazione delle particelle ceramiche.
Il materiale è stato considerato reologicamente stabile nel periodo studiato ed è stato dimostrato che le particelle ceramiche tendevao a non agglomerarsi tra loro.
Durante i vari tests condotti, sono stati riscontrati difetti superficiali in alcuni tipi di campioni compatti; ciò può essere ricondotto a diversi fattori, quali un legante poco volatile, un basso wall thickness e alcuni parametri di stampa non ancora ottimizzati.
Inizialmente sono stari realizzati scaffolds cubici utilizzando il file CAD della spugna polimerica; in seguito è stato creato un secondo file CAD per ottenere gli scaffolds cilindrici con aspect ratio 2:1.

Gli scaffolds cubici hanno una dimensione pari a 4,72×5,15×5 mm, mentre gli altri hanno un diametro di 5 mm e un'altezza di 10 mm.
In totale sono stati stampati 30 scaffolds cubici e 90 cilindrici.
Nonostante l'elevata porosità e una struttura caratterizzata da trabecole estremamente fini, gli scaffolds sono stati stampati correttamente e non sono stati riscontrati difetti superficiali.
L'evaporazione della matrice organica e la sinterizzazione di tutti i green bodies realizzati, sono state effettuate in un forno Nabertherm P330 per 99 h, ed è stata raggiunta una temperatura massima pari a 1300 °C, mantenuta per 2 ore.
Presso il laboratorio DISAT del Politecnico di Torino è stata effettuata la caratterizzazione microstrutturale, compositiva e morfologica degli scaffolds.
L'analisi di diffrazione a raggi X (XRD) ha confermato che gli scaffolds sono costituiti unicamente da idrossiapatite, e quindi, non sono avvenute transizioni di fase durante il trattamento di sinterizzazione ad alta temperatura.
L'analisi morfologica al microscopio elettronico a scansione (SEM) ha rivelato la presenza di macropori altamente interconnessi nell'intervallo 200-800 μm; inoltre è stata rilevata una minima porosità interstiziale, prova del raggiungimento di un buon livello di sinterizzazione.
È stato ottenuto un rapporto atomico Ca/P di 1,89 ± 0,092, molto vicino a quello stechiometrico.

Alla luce dei risultati ottenuti, l'accoppiamento della tecnologia DLP e della spugna polimerica μ-CTs può essere considerata una strategia promettente per la realizzazione di scaffolds ceramici a base di HA, in grado di riprodurre fedelmente l'architettura naturale dell'osso spongioso, nonostante sia stato utilizzato un template di spugna commerciale..
In futuro sarà necessario condurre ulteriore analisi valutare le proprietà meccaniche e biologiche delle impalcature prodotte sia *in vitro* che *in vivo*.

Figure 0. Scaffolds porosi cilindrici ottenuti con tecnica DLP.

Abstract

In the last decades, Bone Tissue Engineering (BTE) has been one of the most discussed research topics in the field of regenerative medicine (Tissue Engineering).
Bone tissue is able to regenerate itself, but, in the presence of extensive bone defects due to trauma, tumor removalor bone congenital diseases, it could be necessary to go into surgery and insert a bone graft to promote tissue healing.
Every year, more than 2.2 million people worldwide undergo surgery to repair critical bone defects.
Currently, both natural and synthetic grafts are used, even though the ideal grafting material does not yet exist. In general, natural grafts show several advantages, including good biocompatibility and osteoconductivity, but at the same time they are characterized by intrinsic drawbacks (low number of donors, risk of immunological response and ethical-religious issues) that limit their use.
Where the use of natural bone grafts is impossible, synthetic bone grafts, commonly known as scaffolds or synthetic matrices, could represent a good alternative.
Scaffolds are porous 3D structures capable of mimicking the extracellular matrix (ECM) of natural bone; they must provide a structural model that can withstand the physiological loading conditions while promoting cell growth and proliferation by specific material/environment interactions.
Biodegradability, interconnected porosity, controlled pore size and trabecular architecture and source material are just some of the main requirements that a BTE scaffold must meet to optimize time and quality of bone regeneration.

With regard to the biomaterials that can be used for the production of bone scaffolds, particular attention is currently paid to calcium phosphates (CaPs); among these, synthetic hydroxyapatite (HA, $Ca_{10}(PO_4)_6(OH)_2$) is one of the most appreciated due to its similarity to natural HA, which constitutes more than 60% of the inorganic bone matrix. Among the advantages resulting from using HA as scaffold material, its excellent osteoconductivity and bioactive properties are the ones mainly involved in promoting cell adhesion, proliferation and new tissue synthesis.
Moreover, there are experimental evidences of the higher mechanical properties of HA struts when compared to other bioceramics, such as bioactive glasses or tricalcium phosphate (TCP), although, in some cases, its slow rate of degradation may be incompatible with implant requirements.
Additive Manufacturing (AM) or Rapid Prototyping (RP) techniques play an important role in the creation of highly porous and interconnected scaffolds, guaranteeing higher reproducibility and reliability of the production process compared to traditional scaffold manufacturing.
RP techniques are characterized by a layer-by-layer construction of the 3D structure, following a computer-aided design (CAD) software model.
There are many AM techniques suitable for the processing of ceramic materials, such as select laser sintering (SLS), 3D printing (3DP), direct ink writing (DIW), stereolithography (SLA) and digital light processing (DLP) based on SLA.
Lithography, in combination with DLP, builds the 3D objects layer by layer by selectively polymerizing a photosensitive liquid suspension containing homogeneously dispersed ceramic particles.
A single layer is generated at a time through a Digital Micromirror Device (DMD) which behaves like a dynamic mask coupled with a projection system.

The printing method makes it possible to obtain the so-called "green body" formed by ceramic powders and an organic matrix that will be eliminated through a high-temperature treatment (sintering) during the post-processing phase.
CAD models can be created on the basis of micro-computed tomography (μ-CT) or medical magnetic resonance imaging (MRI) that allow to obtain unique patient-specific models of the defect to be treated. Otherwise, large-scale, marketable and standardized scaffolds can be produced using CAD models that replicate regular 3D shapes obtained from the repetition of cellular units of known geometry and properties, arranged in a three-dimensional array. However, this approach usually led to rough models which hardly replicate the actual trabecular architecture of bone.

The present experimental work aimed at the production of HA highly-interconnected porous scaffolds able to imitate the trabecular architecture of spongy bone while guaranteeing at the same time high standardization and reproducibility of the manufacturing process.
In order to do that, DLP technology based on SLA was used in order to reproduce the 3D architecture of commercial polyurethane sponges, basing on CAD models deriving from microtomographic reconstruction.
The printing process led to the production of 3D structures (Figure 0) exhibiting high morphological and compositional affinity to the native tissue.

HA ceramic scaffolds of cubic and cylindrical geometry (2:1 aspect ratio) were manufactured at the Austrian company Lithoz GmbH using their CeraFab 7500 stereolithographic system.During the stay in Lithoz, much management has been dedicated to the definition of the slurry composition (LithaBone 480E) and its characterization. In particular, the slurry stability was carefully evaluated over a period of 5 weeks, monitoring rheological properties, relative density, maximum bending strength and agglomeration tendency of suspended ceramic particles.

The material was considered rheologically stable over the period studied and it was demonstrated that ceramic particles tend to not agglomerate with each other.
Due to several factors such as a low volatile binder, low wall thickness and some non-optimized printing parameters, or an excessively rapid heat treatment, some types of compact samples created for testing and printing trials, had post-sintering surface defects.
At first, cubic scaffolds were made using the sponge CAD file; then a second CAD file was created to obtain cylindrical scaffolds with an aspect ratio of 2:1. The cubic scaffolds have a dimension equal to 4.72×5.15×5 mm, while the others have a diameter of 5 mm and height 10 mm.
A total of 30 cubic and 90 cylindrical scaffolds were printed.
Despite the high porosity and the extremely fine trabeculae of the structure, the scaffolds were printed correctly and no defects were detected after their sintering.
The evaporation of the organic matrix and the sintering of all the green bodies made with LithaBone 480E were carried out in a Nabertherm P330 furnace for 99 h. The maximum sintering temperature of 1300 °C was maintained for 2 hours.
Microstructural, compositional and morphological characterization of HA-scaffolds was carried out at the DISAT laboratory of the Politecnico di Torino.
Hydroxyapatite was the only crystalline phase detected by X-ray diffraction (XRD), proving that no phase transitions occurred upon high temperature sintering treatment.

The Scanning Electron Microscopy (SEM) morphological analysis revealed the presence of highly interconnected macropores in the range 200-800 μm and minimal interstitial porosity was observed, thus indicating that a good sintering level was achieved. Ca/P atomic ratio was 1.89 ± 0.092, really close to the stoichiometric one.
In light of the results obtained, the coupling of DLP technology and polymeric sponge μ-CTs can be considered a promising strategy for the realization of HA-based ceramic scaffolds, very faithful to the natural architecture of the spongy bone even though an industrial template was used.
Future analysis will be necessary to evaluate the mechanical and biological properties of the manufactured scaffolds both *in vitro* and *in vivo*.

Figure 0. Cylindrical porous scaffolds obtained by applying DLP technique.

Chapter 1

Ceramic Materials in Bone Tissue Engineering

Every year, the number of people affected by bone tissue problems is dramatically increasing, due to both ageing global population and the increase in obesity, which still make pathological bone treatment one of the major clinical challenges of our time.
In the presence of bone tumours, congenital diseases and extreme traumas, bone rarely manages to repair itself and surgery is usually required.
For this reason, Bone Tissue Engineering (BTE) is investing sources on the realization of 3D scaffolds able to mimic the natural bone extracellular matrix niche, while providing mechanical support to the bone healing process.
Scaffolds, combined with growth factors, cells and nutritious, can induce the formation and the vascularization of new bone tissue, thus restoring the starting physiological picture (Figure 1).
Several synthetic biomaterials are currently investigated in BTE for bone scaffold manufacturing. Special attention is devoted to calcium phosphates (CaPs) such as hydroxyapatite (HA), thanks to their excellent osteoconductive and bioactive properties.

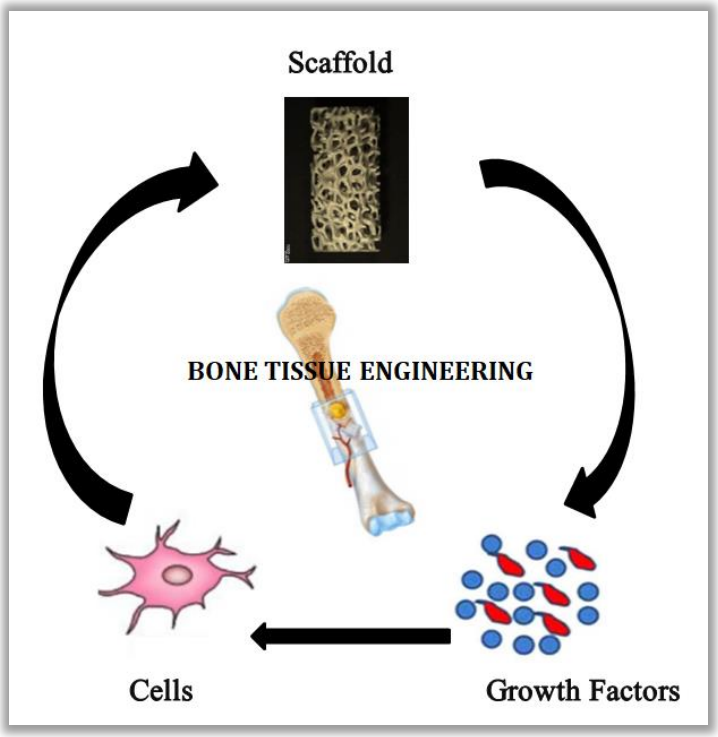

Figure 1. The three essential components in Bone Tissue Engineering (BTE).

1.1 Human Bone

Bone tissue is a particular connective tissue characterized by remarkable mechanical strength and hardness, due to the presence of a highly calcified extracellular matrix (ECM).
Bone tissue mainly performs a function of support of the body, protection of internal vital organs and storage of mineral salts. In addition, together with the muscles, it allows movement [1].
From a materials science point of view, bone can be assumed as an anisotropic composite material with a complex hierarchical structure, as shown in Figure 2 [2].

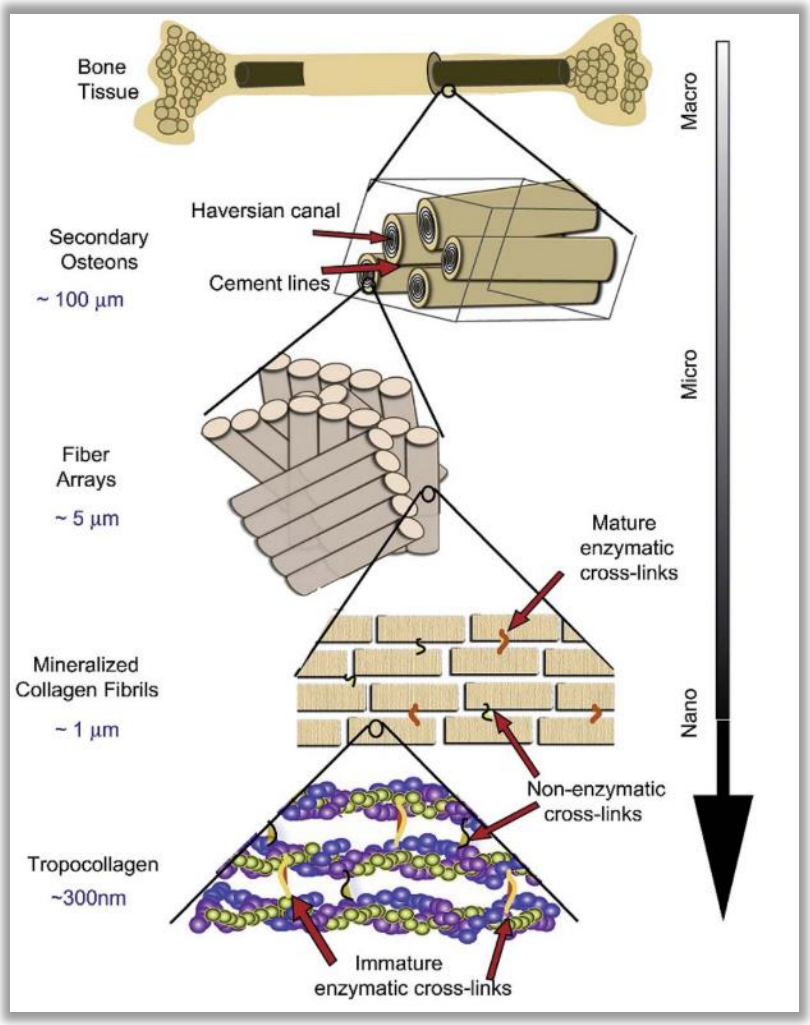

Figure 2. Hierarchical structure of natural bone [3].

Bones can be classified into three different types based on their morphology:

1. **Long bones** develop along a preferential direction and are composed of a central part called diaphysis, and two ends called epiphyses [4].
   Inside the diaphysis, there is the diaphyseal cavity occupied entirely by yellow bone marrow. The walls of the cavity are made of compact bone tissue.
   The epiphyses consist of spongy bone tissue, reinforced by the presence of bone trabeculae. The epiphyses contain red bone marrow, responsible for hematopoiesis [4].

During development, a layer of cartilage, called growth cartilage or epiphyseal disc, can be distinguished between epiphysis and diaphysis. Bone lengthening is possible until this cartilage undergoes mineralization and ossifications.
Examples of long bones are the humerus, femur, radius, ulna [5].

2. **Flat bones** have a very slight thickness compared to the other two dimensions. They consist of a layer of spongy tissue between two layers of compact tissue. These bones mainly have a function of protecting neighbouring organs.
Examples of flat bones are the scapula, the skullcap, and the sternum [5].

3. **Short bones** are small, approximately cuboid, and all three dimensions are similar. They consist of spongy bone surrounded by a thin layer of compact bone tissue; therefore, they do not contain bone marrow.
Examples are the vertebrae and bones of the carpus [5].

In general, human bone is composed of an organic phase (30 - 35 %), an inorganic phase (65 - 75 %) and water (20%) [5].

The complete composition of human bone is summarized in Table 1.

Table 1. Chemical composition of bone (wt%) [3].

Inorganic Phase	**Organic Phase**
Hydroxyapatite (HA) ~ 60 H_2O ~ 9 Carbonates ~ 4 Citrate ~ 0.9 Na^+ ~ 0.7 Mg^{2+} ~ 0.5 Cl^- Others ~ K^+, F^-, Zn^{2+}, Fe^{2+}, Cu^{2+}, Sr^{2+} and Pb^{2+}	Collagen ~ 30 Non-collagenous proteins ~ 3 Traces: polysaccharides, lipids, and cytokines Primary bone cell: osteoblasts, osteocytes, and osteoclasts

1.1.1 Inorganic bone tissue matrix

One of the distinctive characteristics of bone tissue, which distinguishes it from other types of connective tissue, is that it possesses mineral elements in its matrix, which form a hard and compact structure essential for the locomotion functions and support.
The mineralization process already begins during the embryonic development of vertebrates, but increases and reaches completion only during postnatal development. In an adult individual, the mineral component constitutes about 65% of the dry weight of bone tissue. This mineral component consists mainly of calcium (Ca), combined with phosphorus (P), hydrogen (H) and oxygen (O) to form a crystalline molecule called hydroxyapatite (HA) [1].

HA is the most important mineral component of all vertebrate bones and it is responsible for the mechanical properties of the tissue [6].
Biological HA has hexagonal structure and its chemical formula is $[Ca_5(PO_4)_3]OH$ [7]; the size of its crystals in bone is very small (approximately 2x20x40 nm) [5], and they have an elongated shape that expand along intercellular collagen networks [8], as it is possible to see in Figure 3.
Around 60 wt% of human bone is composed of hydroxyapatite (HA), and this is the reason why HA has been extensively investigated in BTE as eligible material for scaffold manufacturing aimed at bone repair [9].

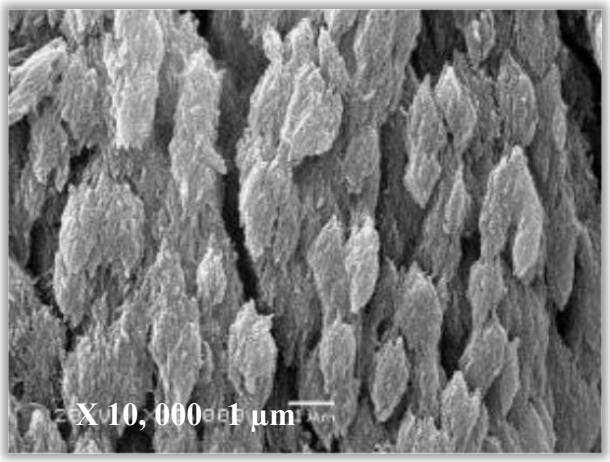

Figure 3. Hydroxyapatite in bone tissue [5].

Hydroxyapatite deficiency can lead to the development of severe bone diseases, such as osteoporosis [10]. It is a skeletal disorder, common especially among women, characterized by compromised bone strength and increased risk of fracture, and attributed to the disruption in the crystalline structure of HA (decrease of the crystalline size and hardness) [10].
Besides being present in bones, hydroxyapatite can be found in tooth enamel; in fact, the latter consists of about 96% hydroxyapatite, 1% organic matrix, and 3% water [6].

1.1.2 Organic Matrix of Bone Tissue

The organic matrix of bone, also called osteoid substance or tissue, consists of collagen and different kind of cells.
Collagen is a jelly – like sclereoprotein, with a triple helix structure.
The fibrils are the fundamental units of collagen; as they aggregate, they form fibres.
Collagen fibres are oriented parallel to each other and HA crystals [5], [3] dispose themselves on top of them.
Surrounded by an amorphous organic cement, the fibres are arranged in bundles, thus creating a lamellar structure [5].
Collagen is the main constituent of cartilage, connective tissue, skin and bone, conferring them strength and elasticity [3].
Bone tissue has several cell types arranged within the lamellas. they are cells of mesodermal derivation and can be distinguished into:

- **Osteoblasts** are rounded cells characterized by a wrinkled endoplasmic reticulum and an extensive Golgi apparatus as well as numerous ribosomes and mitochondria that guarantee the production of collagen and other constituents of the bone matrix [1].
  Osteoblasts are the precursors of osteocytes and take part in the formation and calcification processes of new bone [1].
  Once the production of organic matter is complete, osteoblasts settle into bone gaps, which are non-mineralized ellipsoidal cavities dug into the matrix itself.
  In this phase, osteoblasts become osteocytes and, while remaining viable cells, enter a dormant state [1].

- **Osteocytes** are characterized by an endoplasmic reticulum and a poorly developed Golgi apparatus.
  They have long cytoplasmic extensions through which the cells draw nutrients inside micro canals called bone channels.
  These bone channels intersect, permitting the interaction with other osteocytes and allowing the interstitial fluid to reach cells further away from the nutrient source.
  Osteocytes regulate the balance between the organic and the inorganic phase, calcium and phosphorus levels, the exchange of matter between bone matrix and biological fluids [5].

- **Osteoclasts** are cells that produce and secrete enzymes that degrade the calcified matrix, thus determing bone resorption. They have a multinucleated appearance; the cellular membrane in contact with the tissue to be reabsorbed presents a series of juxtaposed estroflexions, also called "brush hem" [1].
  Osteoclasts come into play in growth processes of new bone, when immature (non-lamellar) tissue is replaced by mature bone tissue, [1] or during bone-remodeling processes [5].

1.1.3 Bone Tissue Morphology: from the micro– to the macro-scale

Depending on its level of structural maturity, bone can be divided into immature or lamellar bone.

Primary or Immature bone is characterized by high cell density and low hardness because of a lower density of hydroxyapatite crystals; it includes a large number of roundish-shaped osteocytes, which are contained in large osteocyte gaps.
During the development stage, the primary bone turns into secondary bone, acquiring the characteristic lamellar architecture, with a higher mineral content [1].

Secondary or lamellar (mature) bone, unlike primary bone, has a higher content of hydroxyapatite crystals, a lower cell density, and its collagen fibres have well-organized spatial arrangement [1].
Lamellar bone tissue can be further classified into cancellous bone and compact bone (Figure 4).

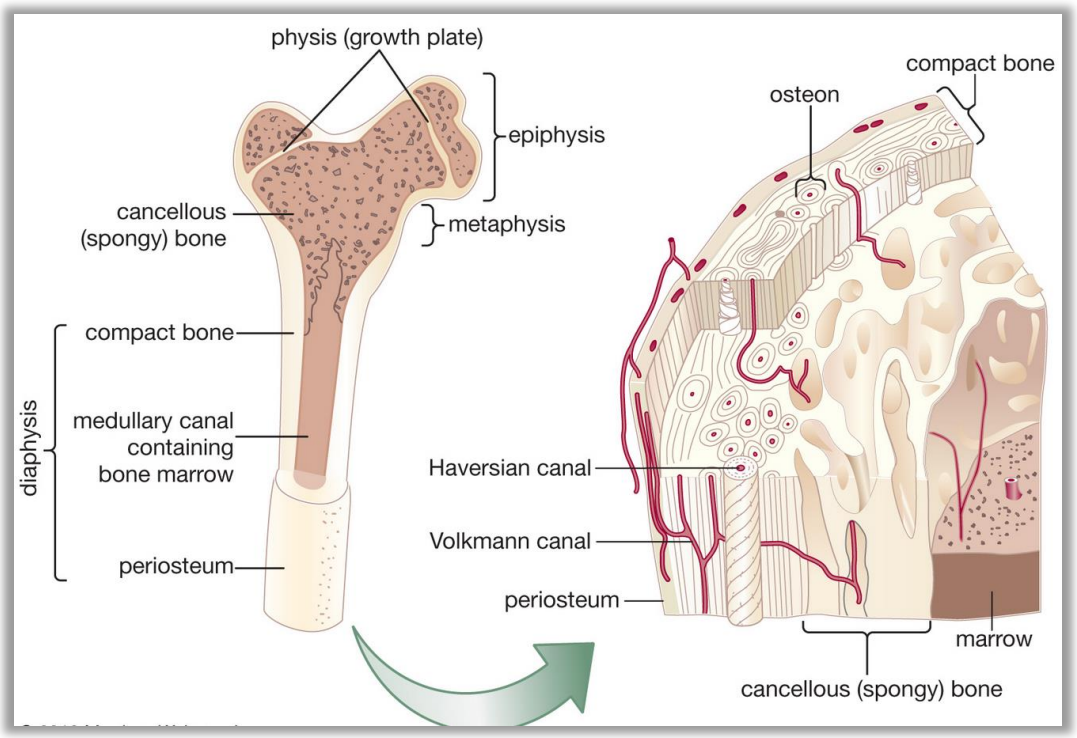

Figure 4. Internal structure of long (mature) bone tissue and cross section of the interior [4].

Compact or cortical bone constitutes the entire central part of the long bones (diaphysis), the outer part of their extremities (epiphysis), the outer part of the short bones and the outer planks of the flat bones [1].

As possible to see in Figure 4, the outer surface of human bone is covered by a connective sheath named periosteum [4].

It is characterized by mineralized lamellae organized to form osteonic or Haversian systems, with the typical closely packed concentric arrangement. This allows for metabolism of bone cells and provides cortical bone with structural support [4].

Osteocytes can be found inside cavities between concentric rings. The canals have capillaries that transport nutrients and oxygen and remove wastes [4].

Compact bone is a material with a range density between 1.6 - 2 kg/ dm^3 [11] and a compressive strength ranging from 130 – 200 MPa [12], tensile strength of 50 – 150 MPa, Young's Modulus 7 – 30 GPa [13], [12] and a porosity of 5 - 13% [2].

Cancellous or trabecular bone is a porous and light bone characterized by a great number of spaces that give a spongy appearance (similar to honeycombed) [4]. It has a lamellar architecture that is structured in trabeculae [12], oriented according to the directions of stress transmission to which the bone is subjected [1], [2].

The density of cancellous bone is lower than that of cortical bone and varies between 0.1 and 0.9 kg/dm^3 [14].

It has a compressive strength of 0.1 – 16 MPa [12] , tensile strength of 10 – 20 MPa [13], Young's modulus of 0.05 – 0.5 [12] and a porosity of about 50 - 90% [15].

Trabecular bone constitutes about 20% of the human skeleton [4]; due to its particular structure, this type of bone tissue is well suited to resist compression forces [1] and it is usually surrounded by a cortical bone, which provides greater rigidity and strength [4].
Its open structure allows for stress relief, like load transmission through the joints. It was showed the spongy bone also has a high level of metabolic activity [4].

1.1.4 Bone Remodelling

Bone is a dynamic tissue that is able to grow and regenerate thanks to the complementary activity of osteoclasts and osteoblasts [5].
The process which leads to the formation of new bone matrix is called osteogenesis or ossification. As Osteogenesis occurs during embryonic development, the early stages of growth but also during healing [5].
Osteoclasts produce acids that dissolve the bone matrix, releasing the mineral salts contained therein [5].
Osteoblasts are responsible for the formation of new bone; they synthesize the organic components of the bone matrix, producing the osteoid (resulting mixture of collagen fibers, proteoglycans and glycoproteins) [5].
Depending on the type of tissue in which the osteoblast is formed, we can have either a membranous (or direct) ossification or an enchondral (indirect) ossification [1].
In membranous ossification, the osteoblast forms into a fibrous connective tissue, while in endochondral ossification, the osteoblast differentiates into a cartilaginous model.
Most of the development of the human skeleton occurs through endochondral ossification; the bones formed in this way are called cartilaginous and are generally bones with a supporting function, such as long bones and vertebrae.
Bones formed via membranous ossification are called membranous bones and usually have no supporting function (the bones of the skull cap, mandible, clavicle).
In conditions of homeostasis, there is a balance between bone synthesis and bone resorption [2]; instead if one of the two actions prevails, diseases such as osteoporosis may arise. In this case, for example, bones become weaker and brittle due to an overwork by osteoclasts [5].
It has been calculated that within a single year, fractures caused by osteoporosis amount to roughly 8.9 million, and in order to manage this issue more than 2 million bone replacement operations are performed annually worldwide [16].
As it is possible to see in Figure 5, the cycle of bone remodelling can be divided in different steps. The process starts with the activation of bone surface with the retraction of cells of bone lining and and the digestion of the endosteal membrane thanks to the collagenase. Then there is the recruitment and activation of osteoclasts at the site concerned, that start to decompose the osteoid matrix. This step is followed by an intermediate (or reversal) phase during which macrophage clean area by old bone matrix. In the same time osteoblast precursors are recruited, they grow and differentiate into mature osteoblasts and they secrete the osteoid material. 30 days later the mineralization begins and will finish after another 130 days in the cortical bone and 90 days in the cancellous bone [17].

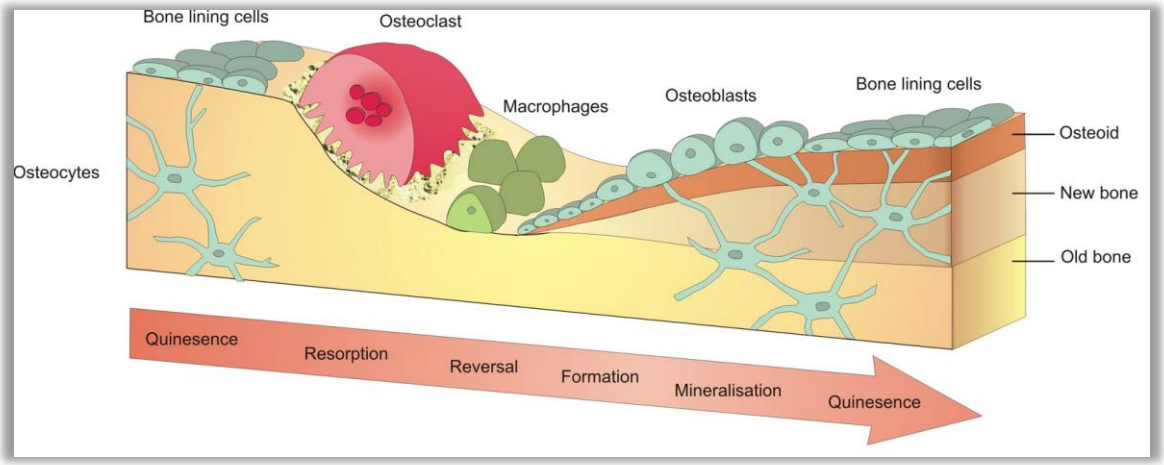

Figure 5. The human bone remodelling process [17].

The mechanism can be influenced by several factors including inflammation process and the application of external mechanical loads [2].
According to Wolff's law, in fact, [2] the bone is able to change its shape, density and properties depending on external factors [5].
The cyclical application of external loads stimulates cells and blood to produce appropriate substances responsible for bone remodelling [5].
This process of bone remodelling, which occurs naturally throughout a person's life, is similar to what happens after injuries or invasive surgeries [5].
However, when a large volume of tissue is removed (due to a tumour resection, or extended infections or when the regenerative process is compromised due to congenital pathologies) [18] , bone self – repair is not possible anymore [19].
In all these cases, artificial substitutes are usually used in clinical practice, in order to support and guide physiologic bone regeneration during the whole healing process, until the complete restoration of the physiological function. [19].

1.2 The use of grafts in Bone Tissue engineering

Transplantation of bone is the second most common tissue grafting in the world after transfusion of blood [20],[21]. Over 2 million bone substitute are estimated every year, with over 500,000 implanted in the US alone [20].
Bone grafts are used in oncologic surgery, orthopaedic surgery, traumatology, and spine surgery to repair large bone defects of critical size [20].
A bone graft can be defined as:

"A synthetic, inorganic or biologically organic combination which can be inserted for the treatment of a bone defect instead of autogenous or allogenous bone"[20].

An ideal bone substitute should promote [21]:

- **Osteogenesis** : the possibility to differentiate osteoblastic cells from the osteoprogenital cells to create new bone tissue [22].
- **Osseointegration** : promote the direct anchorage thanks to a chemical bond between graft and the physiological tissue without growth of a fibrous tissue at the interface [22],[23].
- **Osteoconduction :** the possibility to sustain the development of new tissue at the graft - tissue interface and the creation of new Haversian system and the new oriented and structured vascularization [22].
- **Osteoinduction** : the ability to promote the differentiation of undifferentiated, primitive, and pluripotent cells in the lineage of bone forming cells [23].

In addition, the graft must be biocompatible (potential of the material to give an adequate response in particular applications [24]) and have to stimulate a right response from the near biological ambient with no unwanted toxic effects [22], [20] .
According to the function it is to perform, the graft must satisfy precise mechanical properties comparable with those of host bone and should be assure good interfacial stability and good adhesion with the original tissue [20] so as to avoid mechanical failures under load –bearing condition [24].
During the last 50 years a great variety of bone transplant grafts have been development [20] and they can be divided into natural grafts (transplant of natural bone tissue from human or animal origin) , or synthetic implantable graft; the first category includes:

Autograft: is a part of bone taken from the patient himself [21] from a donor site.
Autograft has high osteogenic properties due to the presence of the bone marrow portion, which is rich in growth factors and totipotent stem cells and is therefore considered the "gold standard" among bone grafts.
This method, however, leads to long hospitalization times, as two surgical procedures are required. In addition, there is a high risk of post-operative complications such as infection and prolonged pain [20],[25].

Allograft: is a part of bone taken from human living donors or corpses after being devitalized, either by freezing or through irradiation [2].
This method avoids the need for two surgeries, but there are risks of infections and undesired immune response [26], [27].
New treatment methods have significantly lowered the risk of disease transmission, but as a consequence of the processing conditions, the natural biological and mechanical properties of bone are weakened, thus reducing the effectiveness of the graft.

Xenograft: is a part of bone taken from a species other than human, for example porcine bone or bovine bone; the latter was first introduced by Maatz and Bauermesteir in 1957 [20].
They have some advantages such as low cost and easy availability [20].
Other authors are very critical about the use of xenografts, due to their high immunity and often insufficient biomechanical properties [28]; in addition, some cases of infections complication were registered, so their use is still limited [20].
In the past demineralized and cell – free xenografts have been used but have been seen to demolish bone morphogenic proteins and other growth factor [28].

Chemically – treated biological materials: Some very special types of xenografts could be also obtained from non-animal biological materials but taken inspiration from nature; an example are grafts obtained from the treatment of some marine corals, which are known as coralline xenografts [20].
Marine corals are made of calcium carbonate and an high proportion of fluorides. Under proper treatments conditions (hydrothermal processes), it is possible to turn coral's carbonates into HA [20].
In January 2010 some Italian scientists proposed the possibility to use wood as a bone substitute, showing a better and quicker bone growth [20]. Their challenge was the development of a bone graft with a biomimetic hierarchical structure on the micrometer scale , to improve biological response and to obtained a better and quicker bone growth [29].
To summarize, natural grafts either from animal or human sources, have intrinsic limitations (like limited number of donors, risk of immunological response and ethical/religious issues). In order to overcome this disadvantages (BTE) has been focusing on use synthetic grafts made with biocompatible materials [22], [25].
This synthetic grafts, known as scaffolds, serve a 3D structural function, able to mimic the bone structure [22] and used in combination with growth factors and cells can be considered a great chance for new tissue growth.
Thanks to new developments in 3D printing techniques and new discovering in biomaterial field, scaffolds are a great alternative to conventionally used tissue grafts. [30], [31].

1.2.1 Biomaterials in BTE for synthetic grafts

"Biomaterial is a non-living substance used in the manufacture of a medical device that at some point has an interface with living tissue".
(Consensus Development Conference, Chester, UK, 1986)

"A biomaterial is a substance that has been engineered to take a form which, alone or as part of a complex system, is used to direct, by control of interactions with components of living systems, the course of any therapeutic or diagnostic procedure, in human or veterinary medicine"
(Williams DF. On the nature of biomaterials, Biomaterials 2009)

The term "biomaterial" refers to particular type of materials that has direct interaction with organic structures to act as a treatment, cure or substitute for a tissue, organ or body function. [32].
Everything that comes from outside and interacts with a living body must be compatible with the latter and must not create any kind of inflammatory reaction and/or rejection.
What differentiates biomaterials from other categories of materials is their capacity to stay in a biological context and not to damage the surrounding environment. [33].
Depending on the response they cause in the host tissue, biomaterials can be classified into:

Inert Biomaterials: cause minimal or no reaction in the host tissue [7] and therefore, after implantation, they do not interfere with body functions [27].

Examples of inert biomaterials are some metals (such as titanium or titanium alloys), ceramics (for example zirconia and aluminia) and synthetic polymers (as PEEK and PMMA) [3].

Bioactive Biomaterials: cause a positive reaction after implantation, exhibiting an intermediate behaviour between bioresorbable and bioinert materials.
Bioactive materials cause a reaction that may be categorized as being between that of bioabsorbable materials and bioinert materials.
A bioactive material is able to create an compatible environment with the growth of healthy tissue (osteogenesis, if we refer to bone tissue), resulting in a mineralized interface that acts as a natural junction between tissue and material [34].
Bonding mechanisms, bonding times, interface thickness and bonding strength change depending on the type of material chosen.
Biomaterials for bone regeneration are able to speed up and strengthen growth of new bone.
Examples of bioactive materials are bioactive glasses, calcium carbonate, calcium phosphates (tricalcium phosphate (TCP), hydroxyapatite (HA) and several formulations of calcium sulphate (CS)) [27],[3].

Bioactive material for bone regeneration can be divided into two different categories [34],[35]:

Class A: osteoproductive materials
The implant is settled by the osteogenic cells present in the surrounding biological space.
These materials can bind to both soft tissue and hard tissue [34].
Class B: osteoconductive materials
Prosthetic implants provide a biocompatible interface on which tissue of bone can grow [34].

Biomaterials commonly used in BTE can be grouped into four major classes: [7], [36]

1. metals
2. synthetic polymers and natural polymers
3. ceramics
4. composites

Metals are usually inert and are mainly used for applications subjected to loads, with sufficient fatigue strength to withstand the daily activity of the individual.
However, metals have several disadvantages such as a lack of adhesion capacity of tissue cells and slow and poor degradation of the implant. [37]
To replace or repair damaged bone, the most commonly used metals are stainless steel, titanium-based alloys, tantalum and cobalt.

Natural and synthetic polymers are applied in different BTE fields of application, especially for scaffold construction. They are easier to process than metals.
The natural polymers have the great benefit of being easily biocompatible and biodegradable and are very similar to the structure constituents of different kinds of tissues (e.g. collagen).
Natural polymers most used in BTE are collagen, starch and chitosan.[38]

Synthetic polymers can be obtained in the laboratory under monitored conditions. They have expected and reproducible physical and mechanical qualities like degradation rate, tensile strength and elastic modulus.
There are different classes of synthetic polymers that are used in the manufacture of scaffolds as bone substitutes, for example: polyesters, polyorthoesters, polyanhydrides, polycaprolactone [9].

Ceramic materials are biomimetic materials famous in BTE for having a mineralogical composition similar to that of human bone and good biocompatibility and osteoconductive properties. [8]
Thanks to these characteristics, they are utilized to repair, reconstruction and replacement of damaged and sick parts of the body's human skeletal structure.
Table 2 shows some types of bioceramic materials and their application in the biomedical field.

Table 2. Bioceramics and their applications in TE, adapted from [39].

	Application	Material
Orthopedics	Bone filler	HA, α/β-TCP granules, bioglass
	Total knee arthoplasty	Al_2O_3, ZrO_2, $Al_2O_3 + ZrO_2$ composite
	Femoral stem fixation	Bone cement or HA coating
	Bone scaffold	HA, α/β-TCP, bioglass
	Bone screw	Al_2O_3
	Femoral head	Al_2O_3, ZrO_2, $Al_2O_3 + ZrO_2$ composite
	Acetabular cup fixation	Bone cement or HA coating
	Posterolateral spinal fusion	α/β-TCP
Dental	Fixed partial denture	Al_2O_3, ZrO_2, $Al_2O_3 + ZrO_2$ composite
	Periodontal pocket obliteration	Al_2O_3, HA
	Dental crown	ZrO_2
	Coating on dental screw	HA
Cranio-maxilofacial	Facial reconstruction	HA, α/β-TCP, bone cement, bioglass
	Alveolar ridge	Al_2O_3
	Reconstruction	Al_2O_3, HA
ENT [1]	Middle ear ossicular replacements	Al_2O_3
Drug delivery	Osteomyelitis	Nano HA as drug carrier
	Bone tumor/cancer	Nano HA with cancer drugs, bone cement loaded with cancer drugs

ENT [1]: ear, nose, and throat.

According to their properties and their behaviour inside the human body, bioceramics can be divided into two main categories: inert ceramics and bioactive ceramics; bioactive ceramics can be resorbable or no-resorbable.
An example of inert ceramics is Aluminia (Al_2O_3), which has good mechanical properties and for this reason it is among the most used ceramics in the orthopaedic and dental field [40].
Within the class of active ceramics, we find calcium phosphate - based ceramics (CaPs), bioactive glasses [7], [41].
The most commonly used CaPs in BTE for the treatment of bone defects and fractures and for various dental applications are hydroxyapatite (HA), α- and β-tricalcium phosphates (α-TCP and β-TCP), amorphous calcium phosphate (ACP), octacalcium phosphates (OCP), biphasic calcium phosphates (BCP), the last one is a mix of two distinct phases of CaPs [42].
All types of CaPs are produced in dense or porous forms as powders, bulks, granules,coatings [42].

1.3 Calcium Phosphate-based Bioceramics (CaPs)

Starting from 1900, the scientific community began to be interested in CaPs as materials for the production of bone substitutes in biomedical applications. The first study dates back to 1920, in which has improved bone regeneration was noted in rabbits as the result of the using of CaPs to stuff extended defect of bone [24].
Thanks to their mechanical qualities, similar to those of human bone, their osteogenic potential both *in vivo* and *in vitro* [8], today CaPs are widely used in different fields of medicine, such as otolaryngology, skull - maxillofacial reconstruction, spinal surgery, orthopaedics, treatment of fractures, bone disorders, percutaneous implants, such as dental fillers and periodontal surgery [7].
A study conducted in the USA showed that in 2010 about 1.3 billion dollars were invested in CaPs-based bone substitutes only [33].
CaPs is the useful name to indicate a minerals family containing calcium cations (Ca^{2+}) and metaphosphate (PO^{-}_3), orthophosphate (PO^{3-}_4), or pyrophosphate ($P_2O^{4-}_7$) anions [7] and also hydroxide (OH^-) ions or hydrogen (H^+) ions [24].
CaPs are the main constituent of tooth enamel (~ 90 %) and bone (~ 60 wt % of bone) [24] and this is the principal reason why they are studied in BTE.
They have a crystalline structure and chemical properties very similar to those of bone apatite, [43] and excellent biocompatibility properties [41], [44].
Thanks their bioactive and biocompatible properties [25] result to have good osteoconductive [25] and osteoinductive properties [19], that permit the attaching, the proliferation, the migration and the differentiation of the bone cells, bringing about the growth of new bone[38], no matter of which phase (amorphous or crystalline) or which way in which they are used in BTE (coating, powder, bulk or porous) [9].
During their permanence into the human body CaPs can be partial dissoluted by body fluid causing a local increment of Ca^{2+} e PO_4^{3-} near the bone / implant interface. In this state the environment is supersaturated with carbonate apatite (CHO), that causes the precipitation of apatite nanocarbonate crystals on the surface of CaPs [25]. New bioactive layer adsorbs the near proteins and it leads the progenitor cells to attach themselves to it so that they can proliferate and mature and differentiate

into osteoblasts. This will cause tissue mineralization and the formation of osteoids. The angiogenesis progression will finally result in local bone induction and potential incorporation with the natural bone [25].
The apatite layer formation occurs in different periods of time depending on the type of ceramic; for hydroxyapatite it takes 30 days, while for TCP about 14 days [45].
Qui and Ducheyne have schematized in 11 steps the reactions that happen at the interface between the biological environment and bioceramic [25]:

1. Dissolving the CaPs;
2. Precipitation from the solution on the CaPs;
3. Ion transfer and structured adjustment at the tissue surface / CaPs;
4. Dispersion from the boundary surface layer in the CaPs;
5. Effects mediated by the solution on cell activity;
6. Organic and mineral phase deposition without integration into the CaPs surface;
7. Depositing with the integration of CaPs into the surface;
8. Chemotaxis to the surface of CaPs;
9. Cells attack and replication;
10. Differentiation of cells;
11. ECM formation.

CaPs are also good vectors for bioactive peptides, growth factors and various cell types [33].
They are helpful in the mesenchymal stem cell differentiation and influence the expression of osteoblastic differentiation markers such as Alkaline Phosphatase (ALP), bone morphogenetic protein (BMPs), Collagen Type I (COL1) [7].
The intrinsic pores of bioceramic materials have a filtering effect and store the growth factors of the surrounding body fluid within micropores [27].
The osteoinduction property is strongly influenced not only by porosity but also by other parameters such as their type, degree of crystallinity (high crystallinity indicates low degradation rates) and surface area (granular vs blocks) [46].
Generally, by increasing the degradation rate, a better osteoinductive potential is obtained [25].
Sometimes the osteoinductivity of CaPs can be increased by adding particular osteoinductive signal molecules (extrinsic osteoinductivity) or by chemical and/or structural optimization of the material itself (intrinsic osteoinductivity) [42].
The various types of CaPs differ for the specific Ca/P ratio of each, which involves a precise emission of calcium ions and phosphate ions on which the subsequent bone mineralization will depend [43], [7].
The stability of phosphates is influenced by pH changes and conditions of reaction as temperature, solvent, pressure, and the kind of the precursors [47].
One way to control dissolution is to limit the available surface area by changing the sintering temperature. By decreasing the sintering temperature during synthesis, the number of micropores increases and, consequently, so does the specific surface. In contrast, by raising the sintering temperature, the size of the pores decreases, leading to a decrease in the specific surface [25].

Despite CaPs have many advantages, some limits exist, including the lack of an organic phase (e.g. collagen), low mechanical strength, especially when compared to metals, and they are not very ductile and often fragile.
The brittleness of CaPs means that there is no slippage before rupture, but ceramics fail in a dramatic manner.
For dense bioceramics, their strength is a function of the grain size: the smaller the grains, the more resistant the ceramic will be.
Mechanical properties increase as the crystalline phase increases and porosity decreases. If the crystalline phase is greater than the amorphous part, CaPs will be characterized by greater compressive and tensile strength and fracture toughness [33], [9].
In general, for bioceramics to be resistant and robust, they must be made of small, homogeneous powders. However, for maximum packing and minimum shrinkage after sintering, it is advisable to use a percentage of coarse powders equal to 70% of the total, and the remaining 30% of fine powders.[33]
So, from a mechanical point of view, we can say that CaPs are brittle polycrystalline materials, with low impact and fracture resistance and their mechanical properties strictly depend on the composition, crystallinity, grain boundaries, and grain size.
A strategy to obtain a material with better mechanical strength properties is to make a multi-phase CaPs compound. This approach is characterized by the formation of homogeneous mixtures of two (biphasic), three (triphasic), or more (multiphasic) single phases of CaPs with different solubilities.
In general, most scientific activities related to CaPs - based biomaterials have as their primary objective the production of a carbonate-substituted hydroxyapatite ceramics, with a composition similar to that of natural bone.
The preparation must be fast and reproducible in order to be marketable.
The final product must be thermally stable and must not decompose into unwanted secondary phases during sintering and calcination [47].
Table 3 shows the main CaPs used in BTE and their characteristics.

Table.3 Existing CaPs and their major properties, adapted from [33].

Material	Chemical formula	Ca/P molar ratio	Solubility at 25°C, g/L	pH stability range in aqueous solutions (25 °C)
Monocalcium phosphate monohydrate (MCPM)	$Ca(H_2PO_4)_2 \cdot H_2O$	0.5	~ 18	0.0-2.0
Dicalcium phosphate dehydrate (DCPD), mineral brushite	$CaHPO_4 \cdot 2H_2O$	1.0	~ 0.088	2.0-6.0
Octacalcium phosphate (OCP)	$Ca_8(HPO_4)_2(PO_4)_4 \cdot 5H_2O$	1.33	~ 0.0081	5.5-7.0
α – Tricalcium Phosphate (α - TCP)	α - $Ca_3(PO_4)_2$	1.5	~ 0.0025	a
β – Tricalcium Phosphate (β - TCP)	β - $Ca_3(PO_4)_2$	1.5	~ 0.0005	a
Amorphous calcium phosphate (ACP)	$Ca_xH_y(PO_4)_z \cdot {}_nH_2O$, n= 3 - 4.5, 15-20% H_2O	b	b	5.0-12.0
Hydroxyapatite (HA, HA_p, OHA_p)	$Ca_{10}(PO_4)_6(OH)_2$	1.67	~0.0003	9.5-12.0
Fluorapatite (FA or FA_p)	$Ca_{10}(PO_4)_6F_2$	1.67	~ 0.0002	7.0-12.0
Oxyapatite (OA, OA_p)	$Ca_{10}(PO_4)_6O$	1.67	~ 0.087	a
Tetracalcium phosphate (TTC)	$Ca_{10}(PO_4)_2$°	2.0	~ 0.0007	a

CaPs are used in TE in the way of cements, coatings, scaffolds or paste [24] More recently they have started being used to create nano-objects (e.g. nano-tubes or nano-needles) [36]; or in the form of dispersed nanoparticles.

There are also CaPs injectable. These can also be transported easily through a non-invasive method in the defect as a water-based paste. They subsequently fix, complete the defect and support the regeneration of the tissue over time. This allows them to be used as a drug delivery agent or to treat a defect in difficult areas, such as the craniofacial complex or vertebroplasty [46].

Some example of CaPs which are commercialized are: BoneSource® (Stryker Leibinger, Germany), Norian® (Synthes Craniomaxillofacial, USA), and Mimix® (Walter Lorenz Surgical, USA) [46].

Among the many existing CaPs, undoubtedly hydroxyapatite (HA) and tricalcium phosphate (TCP) play a very important role in the realization of BTE products [38], [44].

TCP is an osteoconductive material and supports the formation of new bone through the release of calcium and phosphate ions; it also degrades quickly on contact with human body fluids.

HA, as already pointed out, is known for its biocompatibility, bioactivity and high osteoconductivity. together with a higher chemical stability in contact with body fluids than TCP [6].
Thanks to these properties, HA has been and still is among the most studied and used materials in the field of Bone Tissue Engineering [44].
Table 4 shows the major properties of HA and two allotropic forms of TCP (α –TCP e β – TCP); these CaPs will be described following more in details.

Table 4. The major properties of HA and TCP, adapted from [42].

Material	**Stoichiometry**	**Crystallography**	**Molar ratio (Ca/P)**	**Molar mass g/mol**	**Density g/cm^3**
HA	$Ca_{10}(PO_4)_6(OH)_2$	Hexagonal	1.67	988.62	3.156
β –TCP	β - $Ca_3(PO_4)_2$	Rhombohedral	1.5	310.17	3.066
α - TCP	α - $Ca_3(PO_4)_2$	α = monoclinic α' = hexagonal	1.5	310.17	α = 2.866 α'= 2.702

1.4 Hydroxyapatite (HA)

1.4.1 Chemical structure of HA and its properties

"Apatite" (from the Greek for *"apatáo"* that means "I dupe"), was first used by Werner in 1786, and includes a family of compounds with similar structure (hexagonal system, space group, P63/m); however, the exact structure of apatites is not yet clear due to the different types of morphology and non-stychiometric variations that exist.

The general formula for apatite is :

$$M_{10}(XO_4)_6Z_2$$

M = bivalent cation
X = trivalent anion
Z= monovalent anion

The specific name of each apatite will depend on M, X and Z. [30]
For HA the bivalent cation (M) corresponds to calcium (Ca^{2+}), X to phosphorus (P^{5+}) and Z to the hydroxyl radical (OH^-).
Its chemical formula appears to be:

$$[Ca_5(PO_4)_3]\ OH$$

but it can also be found in the following form:

$$[Ca_{10}(PO_4)_6]\ (OH)_2$$

To display there are two formula units in the cell of the crystallographic unit [48].

Calcium, hydroxide and phosphorus are present by weight in the following percentages (Table 5):

Table 5. wt% of ions present in HA.

Elements	**wt %**
Ca^{2+}	39.84
PO_4^{3-}	56.77
OH^-	3.39

As we can see in Figure 6, hydroxyapatite is composed of a rather complex crystalline structure, consisting of phosphate ions (PO_4^{3-}) hydroxyl ions (OH^-) and calcium ions (Ca^{2+}).
The elementary cell has a structure like an hexagon, with space group P63/m and cell parameters a = b = 9.4225 Å , c = 6.8850 Å [49].

Crystal growth/degradation oriented on the c-axis is attributed to its single latex parameter (a = 0,95 c = 0,68 nm) and hexagonal symmetry [8].
In comparison with other calcium phosphate ceramics it is stable in an aqueous environment, in a pH range of 4.2 - 8.0 [40].
In each crystalline cell the PO_4^{3-} are divided into two planes, at a crystal height of ¼ and ¾ respectively; this results in the creation of two different types of channels across the c axis: channel A and channel B. [50]
In channel A there are oxygen atoms of the phosphate group and ions of calcium type II (Ca(II)) arranged at the vertices of two equilateral triangles that are rotated 60 degrees from each other.
The type B channel, with a diameter of 2 Å, contains type I calcium ions (Ca(I)).
Due to a different distribution of OH- ions it is possible to distinguish two types of HA: stoichiometric HA or (hexagonal HA) and monoclinic HA.

In the stoichiometric HA, at the centres of type A canals, there are OH^- radicals, with alternate orientations.

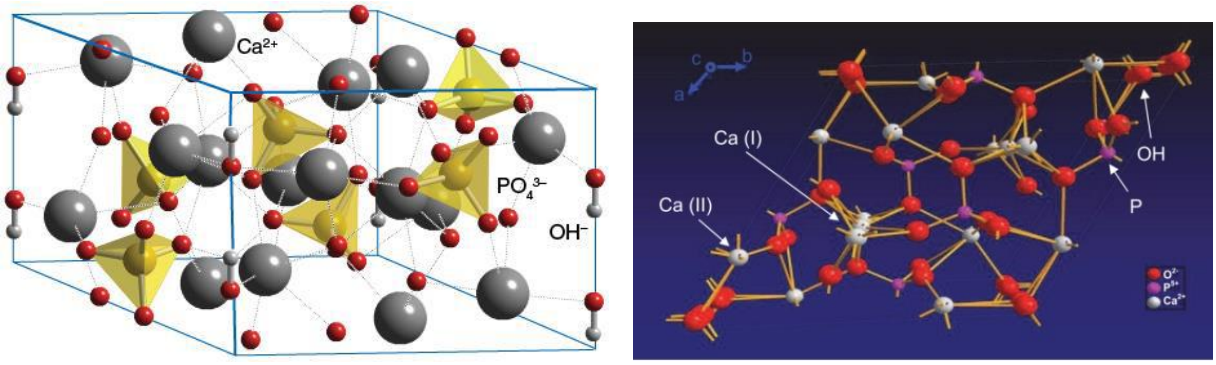

Figure 6. The Crystalline Structure of Hydroxyapatite [24].

The monoclinic form of HA is more thermodynamically stable and ordered and it forms at high temperatures, but there is never been any evidence of it in calcified tissue.
In each elementary cell we can detect:

14 Ca^{2+} ions : 6 of them inside the cell and 8 shared with adjacent cells.

➔ Total = 10 ions Ca^{2+}

10 PO_4^{3-} ions : 2 of them located inside the cell and 8 peripheral ions, shared with as many adjacent cells.

➔ Total = 6 ions PO_4^{3-}

8 OH^- ions : being along the edges, they all belong to the cell by ¼
→ Total = 2 OH^- ions [34].

The crystalline structure of HA can accommodate substitutions by various other ions for the Ca^{2+}, PO_4^{3-} and OH^- groups.
Ionic replacements can affect crystal morphology, crystallinity, solubility, latex parameters, and thermal stability of HA and biological response.
Cationic substitutions occur at sites that are normally occupied by calcium atoms, whereas anionic substitutions may occur either in phosphates or in place of hydroxyl.
Chlorapatite and fluorapatite are common examples of anion substituted HA, where OH^- ions are replaced by F^- and Cl^- ions (Figure 7).
HA is characterized by a Ca/P ratio of 1.667, similar to than in human bones and teeth, thus making it very suitable for orthopaedic, dental, [51] and maxillofacial repairs [52].
The closer the Ca/P value is to 1.67, the greater the stability of the material inside the human body [50].
HA with Ca/P < 1.5 is considered soluble.

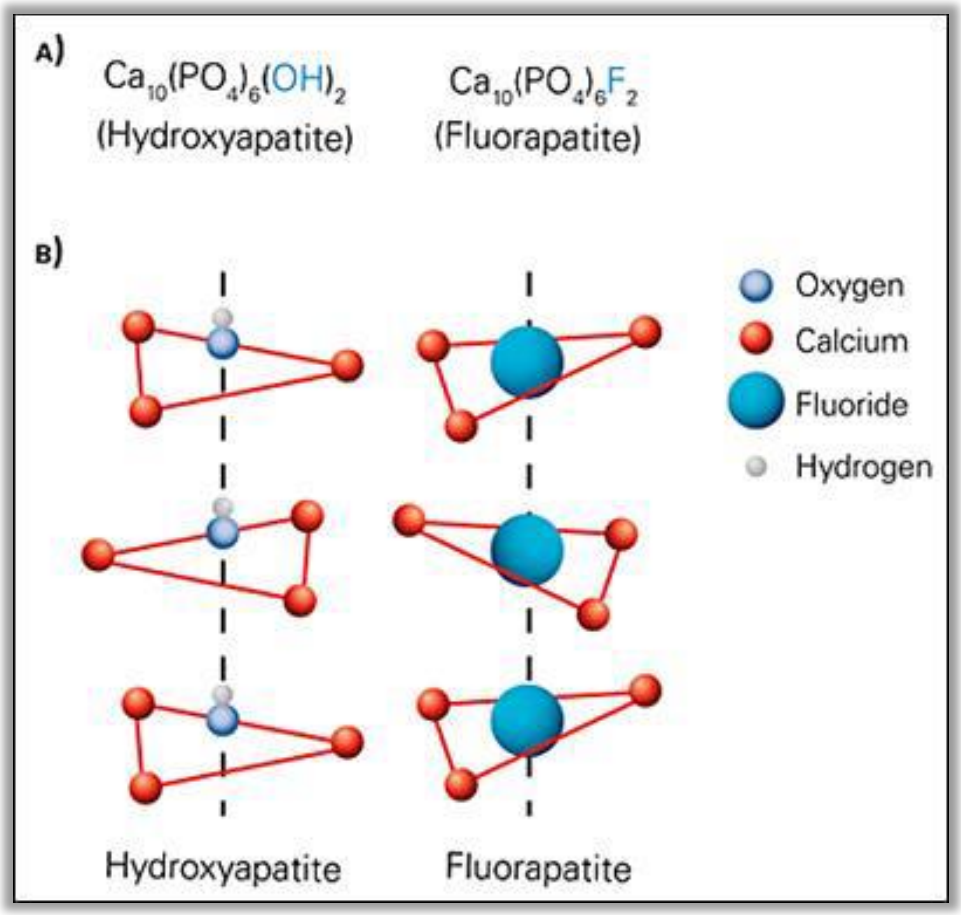

Figure 7. Comparison between the chemical structure of hydroxyapatite and fluorapatite [34].

It has also been shown that mechanical strength increases with increasing Ca/P ratio and reaches its maximum value if the Ca/P ratio is ~1.67 (stoichiometric HA) and decreases suddenly if the Ca/P ratio > 1.67 [33]. Instead, strength increases with decreasing of porosity [24].
Therefore, by altering the molar ratios Ca/P, it is possible to manipulate the degradation rate [8].
Shape, size and distribution of HA powder crystals significantly affect the mechanical properties, biocompatibility and bioactivity of the material [53],[54].
For this reason, it is important to focus on the different techniques for making HA powder.

Table 6 summarizes principal properties of HA [24].

Table 6. Principal properties of HA [24].

Property	Value	Property	Value
Density	3. 16 g/cm^3	**Poisson's ratio**	0.27
Decomposition temperature	> 1000 °C	**Fracture Energy**	2.3 – 20 J/m^2
Dielectric costant	7.40 – 10.47	**Fracture toughness**	0.7 – 1.2 MPa·m ^{½} (decrease with porosity)
Thermal conductivity	0.013 W / (cm · K)	**Fracture hardness**	3 – 7 GPa (for dense HA)
Melting point	1614 °C	**Biocompatibility**	High
Tensile strength	38 – 300 MPa (for dense HA) ~ 3 MPa (for porous HA)	**Biodegradation**	Low
Bending strength	38 – 250 MPa (for dense HA) 2 – 11 MPa (for porous HA)	**Bioactivity**	High
Compressive strength	120 – 900 MPa (for dense HA) 2 -100 MPa (for porous HA)	**Osteoconduction**	High
Young's elastic modulus	35 – 120 GPa	**Osteoinduction**	Nil

1.4.2 HA Synthesis Techniques

According to Sadat-Shojai et al., synthetic HA synthesis techniques can be divided into 4 main groups: [54]

1.4.2.1 Dry methods

Dry method includes two different methods: solid – state synthesis and mechanochemical method. Powders made using dry methods are usually characterized by a large grain size and an irregular shape [54] and derived from low cost raw material [55].
The size of the particles is usually above the nano – level and their phase purity is lower than wet methods [55]
According to the literature, dry methods do not require particular processing conditions, and do not use a solvent [54].

Solid-state synthesis is a relatively simple procedure and can be used to make powders in mass. Usually, a previously prepared CaP salt is used as a precursor, which is then ground and calcined at a very high temperature (e.g. 1000°C).
The high calcination temperature leads to the formation of a good crystalline structure.
The final particles are heterogeneous and rather irregularly shaped.
The second method is **Mechanochemical method**, also known as mechanical alloying, allows us to obtain a powder with a much more defined structure than the solid-state method, thanks to perturbation of surface – bonded species as a consequence of pressure, which improves kinetic and thermodynamic reactions between solids [54].
This technique is simple and easily reproducible [53]; principal processing variables are the type of reagents, the type of milling medium and the type of its diameter, the rotational speed and the duration of working phases and interval steps [54].
During their experiments, Nasiri-Tabrizi et al. have proven that the average size of powder decrease with the increase of milling time; this also leads an increase of lattice strain
The high reproducibility combined with low processing costs make dry methods one of the most suitable for the production of HA in large quantities. [53].

1.4.2.2 Wet methods

Unlike dry methods, wet methods allow to obtain HA powders characterized by nanoparticles with a regular morphology. For this reason, they are the most widely used methods for the synthesis of powders [56].
One of the main disadvantages of wet methods is the low temperature used during preparation which leads to the formation of CaP phases other than HA and/or traces of impurities in the crystalline structure due to ions in an aqueous solution [54].
They can be divided into 6 subgroups, described below:

- **Conventional chemical precipitation**: chemical precipitation represents one of the easiest wet method used for HA powders preparation. It is based on the fact that, at pH 4.2 and room temperature HA is usually stable and not very soluble in an aqueous solution [54]; however, the precipitation reaction is usually conducted at pH > 4.2 [54].
  For this technique, Ca-P containing precursors such as calcium nitrate or calcium hydroxide and diammonium hydrogen phosphate or orthophosphoric acid [54], are used.
  Usually, the reagents should be added drop-by-drop, under mild and continuous stirring conditions, checking that the molar Ca/P ratio remains approximately 1.67.
  Then the suspension, after being carefully filtered and dried, is either aged for a period at atmospheric pressure or is immediately reduced to powder [54].
  Powders made by this method are, however, non- stoichiometric and poorly crystalline [54], [47].
  To obtain powders with higher phase purity, the precipitation reaction must be conducted at high temperature or high pH or both. This strategy leads to a decrease in the formation of phase impurities [54].

- **Hydrolysis method:** nanoparticles of HA can be prepared by hydrolysis of other phases of CaPs, such as dicalcium phosphate dihydrate (DCPD), tricalcium phosphate (TCP) under

certain conditions, and also octacalcium phosphate (OCP). To date, OCP has almost completely been abandoned since it tends to incorporate impurities during its transformation into HA [54].

For example, Brown et al., reported the production of HA from TCP, demonstrating that there is a linear relationship between the hydrolysis temperature and the resulting surface area of HA [57].

In addition, by increasing the reaction temperature, the regularity of the crystals increases.[54]

Park et al. have demonstrated that the aspect ratio, thermal stability and stoichiometry of HA all depend strongly o the pH of hydrolysis [58].

- **Sol- gel method** ensures fine and homogeneous powders to be obtained thanks to the mixing of the reagents at molecular level and the possibility of using a low processing temperature [54].

  These are reactions that lead to the formation of a solid gel from a colloidal solution ("liquid sol") [34].

  Starting materials for the preparation of "sol" are usually inorganic salts or salts of organic acids [34] or alkoxides [54].

  The precursors are subject to a series of hydrolysis and polymerization reactions to form the colloidal suspension (the "sol"). At this stage, they work at controlled temperatures around 90 - 120 °C [34].

  The gel is then formed and aged at room temperature. This phase is followed by gelation, drying on a hot plate, and calcination. Through calcination the final organic residues are eliminated [54].

  The main steps of the sol-gel method are shown in the Figure 9.

  A long aging period is necessary for the formation of the apathetic phase; in fact, in the solution phase, the reaction between the calcium and phosphorus precursors is very slow [54].

  The nature of the solvent, the rate of gelation, temperature and pH chosen for the process depend strongly on the type of reagent chosen.

  In vitro studies have shown that HA made by the sol-gel method has a bio - absorbability rate similar to that biological apatite [54].

  HA powders prepared by the sol-gel method shows nano-structured primary particles that can agglomerate into micrometric grains (Figure 9) [34].

  Two major disadvantages for this method are high cost of the starting materials but in particularly the generation of calcium oxide, (CaO). Secondary CaO phase has been shown to be harmful to the biocompatibility, so it is necessary to remove it either by changing the main procedure or by washing the powder with a dilute acid solution (e.g. HCl).

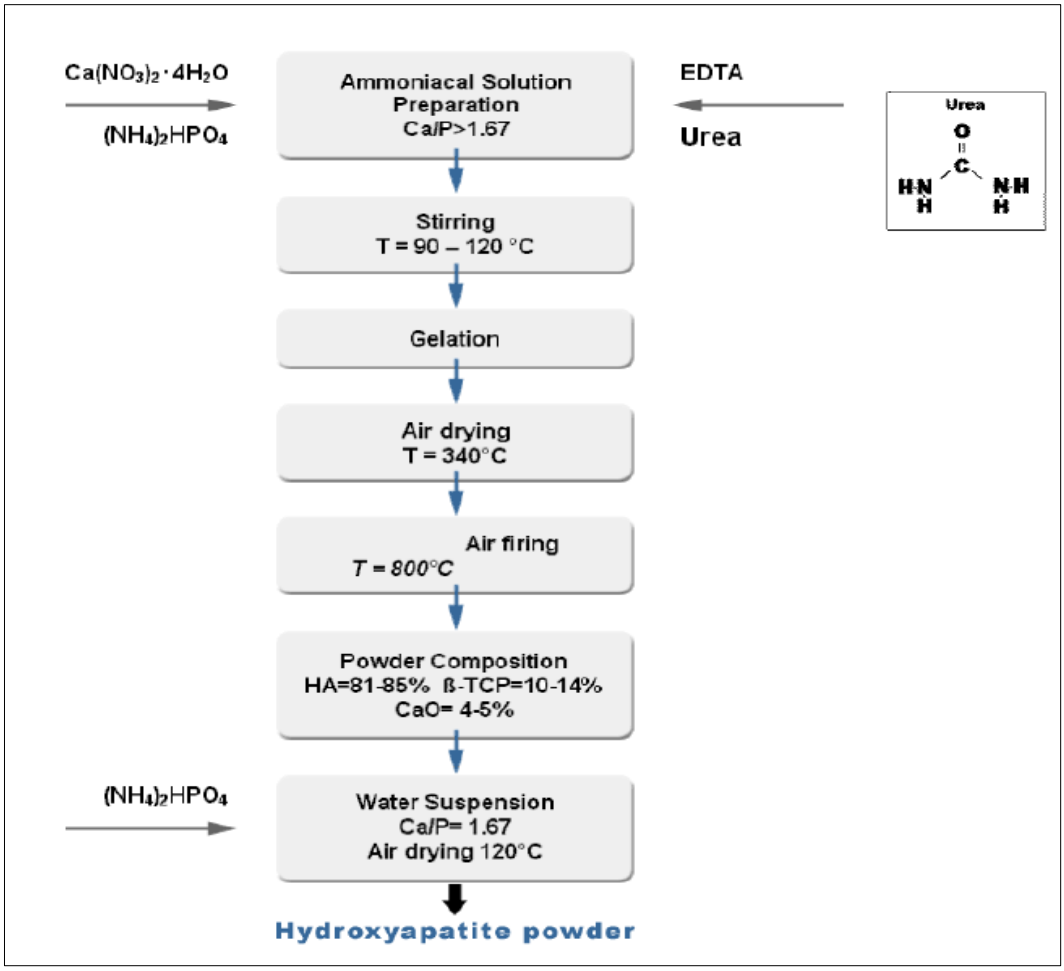

Figure 8. HA preparation scheme using sol-gel method [34].

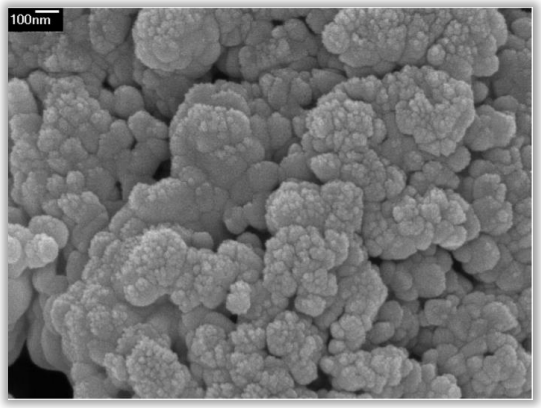

Figure 9. HA powder prepared via sol – gel [59].

- **Hydrothermal method** is characterized by high working temperature and pressure.
  It can be considered a chemical precipitation in which the aging phase is conducted at high temperature [54].
  Work is carried out in an autoclave, where the high temperature in a closed environment favours the formation of solvent vapour and a subsequent increase in pressure [34].

Using a high temperature results in a higher phase purity than that achievable with traditional wet methods and a good Ca/P ratio. However, high temperatures and pressures require expensive equipment, making this process more expensive than other wet methods [54].
The Hydrothermal method allows us to obtain HA crystals as hexagonal prisms of 0.1 mm length [54].

- **Emulsion method** is one of the most effective for reducing particle size and achieving a controlled morphology and microstructure by limiting particle agglomeration [54]. This technique is originally used to made porous materials [60].
  The main starting materials are calcium phosphoric acid and calcium nitrate, because they quite economic and easy to found on the market [60]. The most used surfactants are polyoxyethylene, cetyltrimethyl ammonium bromide and dioctyl sodium sulfosuccinate salt
  It is a rather simple method and uses low processing temperatures and mild synthesis conditions [54].

- **Sonochemical method** is based on chemical reactions activated by powerful ultrasonic radiation.
  The physical mechanism behind the synthesis is acoustic cavitation in an aqueous phase. The reactivity of chemicals is stimulated to accelerate heterogeneous reactions between liquid and solid reagents.
  It has recently been demonstrated that HA particles synthesized with this process possess more uniform, smaller and purer crystals [54]. A.B. Hazar Yoruça, and Y. İpek have proved that by increasing the ultrasonic powder up to 300 W, the particle size decreases significantly [61]. Due to the high speed and high kinetic energy they have stored, it is more likely that these particles can collide with each other and create a more uniform crystal lattice [61]. This characteristic can improve mechanical properties of final product [54].

1.4.2.3 High-temperature processes

These processes are characterized by the need to use a high temperature to partially or completely burn the precursors [54].
There are two different methods:

- **Combustion method** (Figure 10) allows to quickly produce highly pure powder with a single operation. This approach has advantages in terms of relatively simple process preparation, economical raw materials and good chemical homogeneity of the synthesized powder as a result of intimate mixing of the components [54].
  The combustion of the HA solution causes an exothermic and self-sufficient redox reaction between an organic fuel (e.g. citric acid, succinic acid, glycine, urea, sucrose) and oxidants (e.g. calcium nitrate Ca $(NO_3)_2$ and nitric acid (HNO_3)).
  As shown in Figure 10, the aqueous solutions of Ca $(NO_3)_2$ e ammonium sulphate ($(NH_4)_2HPO_4$) are initially mixed together; then high - concentration HNO_3 is added to dissolve the obtained precipitate. A mixture of two fuels is then incorporated (sometimes even a single fuel is used) [54].

To start the reaction, the mixture is heated in an oven at a relatively low temperature (about 300°C). Then, due to combustion, there is a sudden increase in temperature to a maximum [54].
Finally, the mixture is cooled rapidly, so that maximum nucleation is induced, and unwanted further growth of the particles is avoided [54].
Exothermic combustion reaction provides sufficient heat to maintain the system temperature and avoid the need for external heating.
There are many parameters that influence the maximum reaction temperature and consequently the characteristics of the final powder, such as the fuel/oxidant ratio, initial furnace temperature and the nature of the fuel [54].
The resulting product is usually an agglomeration of very fine particles [54].

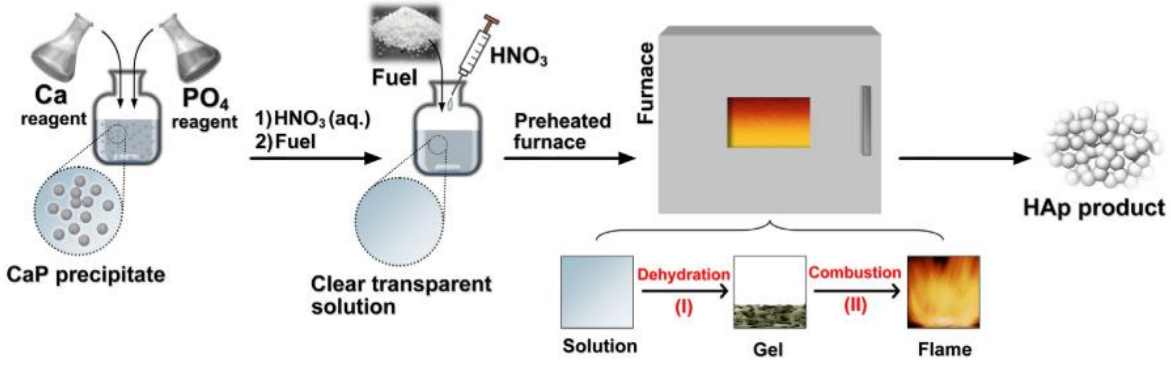

Figure 10. Preparation of HAp nanoparticles via solution combustion method [54].

- **Pyrolysis** is relatively simple and fast because it does not involve post treatments and/or long- term aging at high temperatures, but still guarantees the obtaining of stoichiometric, homogeneous and highly crystalline particles [54].
  The pyrolysis method is also known as "pyrolysis spray" because the precursor solutions are sprayed inside a hot oven using an ultrasonic generator. This is followed by the reaction of the vapours and gases generated at high temperatures and the production of the final powder.
  The high temperature causes the complete evaporation of the precursors, followed by nucleation and growth of the nanoparticles in the gaseous phase.
  A disadvantage of this technique is the possible formation of secondary aggregations, and a consequent decrease in the specific surface area [54].

1.4.2.4 Synthesis method based on biogenic sources

HA obtained partially or entirely from biogenic sources integrate better within the human body due to a greater physical-chemical similarity with bone apatite [54].
HA can be extracted from fish scales or fish bones, bovine bones, from eggshells, or from the exoskeleton of marine organisms.

A period of annealing which lasts several hours is generally required to obtain HA. In this way, the organic part of the bone is removed, and the pure HA particles remain.

Simple thermal annealing is not the only extraction process that can be used; the following are also possible: plasma processing, subcritical water processing, enzymatic hydrolysis, and alkaline hydrothermal hydrolysis [54].
All these methods make it possible to remove organic substances from bone and produce pure HA with an average yield of 65%.
Several experiments have been conducted to try to decrease the particle size at the nanoscale by means of the vibro - milling method, used, for example, by Ruksudjarit et al., who synthesized HA from bovine. The bovine bone was deproteinized in hot water and calcined at 800°C, crushed into small pieces and finally milled in a ball mill pot for a minimum of 24 hours [54].
To improve the properties of the final product, one or more of the methods described above can be combined. Among the various possibilities, a combination of hydrothermal - hydrolysis and hydrothermal - microemulsion are most widely used [54].
Almost all of the techniques listed above allow us to obtain a synthetic form of HA with a stoichiometric ratio similar to biological HA. The most important difference with biological HA is the absence of ionic replacements that occur spontaneously within the human body. [25]
Infact natural HA contains a certain amount of ionic substitution impurities such as Mg^{2+}, F^{-}, K^{+}, Na^{+}, Cl^{-} and Zn^{2+} [3].
Table 7 shows some of the different synthesis routes just described and the main properties of the powder obtained.

Table 7. Different processing technique of HA powder and its properties, adapted from [39].

Processing Technique	**Precursor**	**Powder property**
Solid-state synthesis	Calcium and phosphate containing compounds. Sintering ~ 1250 °C	
Mechanochemical method	Slow mixing of $Ca(OH) + H_3PO_4/(CH_3COO)_2Ca + KH_2PO_4/Ca(NO_3) + (NH_4)_2HPO_4$ solutions using vigorous stirring, followed by aging	HA nanoparticles of 50 - 100 nm length. HA nanorods of 50 nm diameter. HA nanospheres of 200 nm size
Hydrothermal method	Hydrothermal treatment of an aqueous mixture of pH 4.5 comprising $Ca(NO_3)_2$, NaH_2PO_4, HNO_3, and urea at 160 °C for about 3 h	HA whiskers of 10 μm width and 150 μm length
Sol-gel method	Aging an ethanol solution of pH 10 comprising $Ca(NO_3)_2$, $(NaH)_2PO_4$, NH_4OH, and PEG at 85 °C for 4 h, followed by drying	Sintered HA nanocrystals of 50 – 70 nm size
Sonochemical method	Ultrasonic irradiation (28-34 kHz, 100 W) of a pseudo- body solution containing NaCl, KCl, NaH_2PO_4, KH_2PO_4, $CaCl_2$, and $MgCl_2$	Spherical HA nanoparticles of 18 nm size with a specific surface area up to
Synthesis method based on biogenic sources	Thermal method of a deproteinized bovine bone, then crushing and ball milling, followed by vibro-milling using ethanol	Needle-like HA nanopowder of ~ 100 nm size

1.4.3 Dense and Porous Hydroxyapatite

Once HA powder is produced, dense or porous HA based products can be obtained depending on the sintering method chosen. Sintering treatment is carried out in special electric furnaces that reach high temperatures in a controlled manner, where the maximum temperature has to be properly set in order to be below the melting temperature of the material [33].
The heating rate, sintering temperature and holding time depend on the source material.
For HA these values are in the ranges of 0.5–3 °C/min, 1000–1250 °C and 2– 5 h, respectively.[33]
Thanks to the sintering process, the powders bind firmly together; water, carbonates and other volatile chemicals are removed in the form of gaseous products. In most cases, this causes a considerable degree of shrinkage which has to be considered at the process stage [33]
To obtain dense HA (Figure 11), sintering can be performed in several ways, including:

Figure 11. Disks of dense HA [34].

1. **Sintering in the absence of pressure:**
   A pressure of 60-80 MPa is used to compact the powders. These are sintered in air at 950-1300°C for a few hours, with a temperature gradient of 100°C/h.
   Depending on the set temperature, a different degree of HA density can be obtained [34].

2. **Uniaxial hot pressing (HP):**
   Dense HA is obtained without having to reach too high temperatures.
   This prevents the formation of other phosphates, such as tricalcium phosphate, resulting in a purer product [34].

3. **Hot isostatic pressing (HIP):**
   Cold-pressed powders are then hot-pressed by means of the isostatic action of a gas.
   Very dense materials with excellent mechanical properties are obtained.
   With this technique it is possible to obtain products in the desired shape or blocks to be processed later on [34].

These three techniques allow to decrease the grain size and obtain HA with higher densities. In this way, it is possible to obtain finer microstructures, high thermal stability and in the end finally mechanical qualities of HA [62].
The general method to produce porous HA (Figure 12) is sintering the powder with specific pore creating additives, such as naphthalene, paraffin or hydrogen peroxide, which evaporate at high temperatures [62].
Porosity percentage and the dimension of pore depend on particle size distribution of raw ceramic powder, type of fabrication techniques used, types of binder chosen and its concentration, sintering condition [63].
Usually, the particle size of starting ceramic powder should be geometrically in the range between 2 to 5 times larger than that of pores in order to achieve the required pore dimension. The percentage of porosity reductions with increasing conditions such as pressure, sintering time and temperature. In addition, manufacturing influences such as the type and quality of additives, sintering conditions (pressure atmosphere, temperature,) have a significant affect for the porous ceramics microstructures [63].
Porous ceramic based on HA presents a strong junction with natural bone, the pores furnish a strong mechanical interlock that produces a stronger fixation of the structure [63].
In general, porous HA is more resorbable and osteoconductive than dense HA. In fact, thanks to the increasing of surface area more bone cells are able to join it [63].
Also worth mentioning, porous HA structure can also be obtained by natural materials such as coral skeletons, converting $CaCO_3$ into HA under hydrothermal conditions [62].

Figure 12. examples of porous HA [34].

1.4.4 Mechanical properties

The mechanical properties of HA – based products depend on the microporosity, on the method of powder preparation, and on the sintering temperature adopted [9].
In general, the following properties increase when the sintering temperature is increased:

- Density
- Grain size
- Compressive, torsional and flexural strength
- Elastic modulus

Sintered HA has superior properties compared to cortical bone, enamel, and dentin, but fatigue strength is quite low [34].

HA has mechanical properties that decrease significantly with increase of microporosity, amorphous phase, grain size.
Low porosity, high crystallinity and small grain size, on the contrary, increase tensile strengths, compressive strengths, fracture toughness, and stiffness.
Studies have shown that fracture toughness and flexural strength of dense HA are much higher under wet conditions than in dry conditions [9].
Toughness fractures can decrease due to the presence of TCP, that can form during sintering at high temperatures. [34]
If the properties of HA are compared with those of the human bone (Table 8), it is possible to see that the bone has high compressive strength, even if lower than HA [9].
On the other hand, HA has a much lower fracture resistance (fracture toughness) than bone.
The mechanical qualities are lower for porous HA.
The fracture toughness high tensile strength of bone are due to the presence of collagen fibres.
Therefore, HA alone, and in general CaPs cannot be utilised for load-bearing scaffolds [9].

Table 8. Mechanical properties of porous and dense HA and human compact bone, adapted by [9].

Material	Compressive strength (MPa)	Tensile strength (MPa)	Elastic modulus (GPa)	Fracture toughness (MPa)
Dense HA	120-900	40-300	~ 100	~ 1.0
Porous HA (82-86%)	2-100	~ 5	35	0.5 – 1
Cortical bone	130 -180	50 – 151	12 -18	6 -8
Cancellous bone	4 – 12	-	0.1 – 0.5	-

1.4.5 HA Applications in BTE

In 1969, Levit et al. wrote one of the first scientific papers on possible applications of HA in the field of TE [64].
HA powders are mainly used as coating on metal substrates, as starting material for scaffolds, or as fillers for polymeric scaffolds [45].
HA powders as coatings began to be used mainly in the late 1980s; more specially, in 1985 Furlong and Osborn were the first to begin studying HA coatings for clinical applications and since then these coating have shown good results with a 2% failure rate for a 10-year follow-up study [39].
Usually, a metal substrate that is coated with HA by plasma treatment is used: in this way, the use of CaPs has somewhat expanded, even for applications requiring greater mechanical stress, as metal substrates help to increase the poor mechanical strength of ceramics [40], [45].
Clinical results reveal that HA-coated implants have a longer lifetime after implantation rather than uncoated implants, which can be very beneficial, especially for younger patients.
This HA application is highly valued in BTE because combines the great bioactivity and biocompatibility of HA with the good mechanical qualities of metals [62].
Thanks to the HA presence, bone tissue can integrate itself with the implant and, in addition HA reduces the release of metal ions avoiding undesirable inflammatory reactions [62]
In order to achieve positive results, it is crucial to choose the right thickness for the veneer; it has been shown that good results are obtained with a thickness of approx. 40 - 200 μm. If the thickness of coating is higher, less metal ions will be present in the body [62].
An important use of porous HA is for the controlled drug release in bone disorder (such as bone tumours or osteoporosis). Porous HA loaded with drugs ensures the accurate release of substance in the desired area. This local and prolonged release of drug speeds bone healing [62].
Custom – made porous HA scaffolds as gap filler are also widely used to treat bone defects because lead an excellent bone ingrowth, especially in cases where conventional techniques have failed. For example Quarto et al., have implanted a scaffold seeded with in vitro expanded autologous bone marrow cells to cure large bone disease (4-7 cm) of the ulna, humerus and tibia in patients of different ages [64]. At the same years Vacanti et al., have created an natural coral (porous HA; 500-pore ProOsteon) implant functionalized in vitro with autologous periosteal cells, to treat a traumatic avulsion of the distal phalanx of a man thumb [64].
Morishita et al., instead, have treated a disease due to tumors in a tibia and in a femur, using HA scaffolds seeded with in vitro expanded autologous bone marrow stromal cells [64].
For the preparation of 3D scaffolds the HA can be used alone or in combination with different polymers such as polylactic-co-glycolic acid (PLGA), polylactic acid (PLA), poly - l - lactic acid (PLLA) and polycaprolactone (PCL) to improve their bioactivity [65].
Ignjatovi´c et al. and Wanget al. fabricated a HA/PLLA composite and HA/polyethylene composite respectively, and in the both case it was shown these composites have a sufficient mechanical strength to be utilised in BTE [65].
The application of bone synthetic grafts has further evolved in BTE thanks to improvement of different Additive Manufacturing techniques. Some examples of techniques are select laser sintering, laser cladding, fused deposition modelling, 3D printing, solid freeform fabrication, and stereolithography. Various combinations of different techniques are also possible [43].

In addition to the repair of bone defects, HA has also been used for orbital implants (Bio-Eye®) and optalmical application [64].
As well as some of the work mentioned above, the Table 9 shows other studies with HA in the form of powder, coating or as a starting material for scaffolds for bone regeneration.
In the Table 10 Instead, is listed various examples of the commercial HA available for BTE.

Table 9. HA studies in BTE from 1997 to 2017.

Authors	Material	Aim	References
Hurzeler M.B. et al, 1997	Autogenus bone + porous HA (3:1)	Improve bone formation and mineralization reducing time	[66]
Kihe A.R. et al, 1997	HA + collagen	Improve bone formation than HA alone	[66]
Quinones C.R. et al, 1997	Porous HA	-	[66]
David A. Cottrell et al, 1998	Porous block HA (coralline HA)	-	[66]
Chang Y.L. et al, 1998	HA coated implant	-	[66]
Carlo Mangano et al, 2003	Porous HA	-	[66]
Rumi Fujiti et al, 2003	HA / β-TCP	-	[66]
Ahmed El-Ghannam,2004	HA	Accelleration of bone formation	[66]
M. Heliotis et al, 2006	HA + bone morphogenic protein (BMP)	Good results for the treatment of large bone defects	[66]
F.Schwarz et al, 2007	Scaffold HA / β-TCP	Shows osteoconductive scaffold property	[66]
O.S. Schindler et al, 2008	Composite ceramic bone graft substitute	-	[66]
Yadollah Soleymani Shayesteh et al, 2008	Mesenchymal stem cell with HA / β-TCP	Improve bone formation	[66]
Roohani-Esfahani et al. 2010	PCL/ HA/ Biphasic calcium phosphate (BCP) Scaffold	-	[67]
Izawa et al., 2014	Compound of Hap hydrogel based on xanthan gum	Hydrogel for an organic template for calcium mineralization in bone tissue	[68]

Wang et al., 2014	Chitosano +nHA Scaffold	-	[67]
Gopi et al., 2014	HA co-substituted with strontium and cerium reinforced	Improve bone formation and study bone bonding ability and the antibacterial activity	[68]
Hadavi et al., 2017	Scaffold HA / gum Arabic	Study effect of polysaccharide/n-HA scaffold on the ossification	[68]

Table 10. Various examples of commercially available HA for BTE, adapted from [64].

Trade name	Producer	Country
Actifuse	ApaTech	UK
ApaPore	ApaTech	UK
Apaceram	Pentax	Japan
Bonefil	Pentax	Japan
Bonetite	Pentax	Japan
Bonoceram	Sumitomo Osaka Cement	Japan
Bioroc	Depuy – Bioland	France
Cerapatite	Ceraver	France
BoneSource	Stryker Orthopaedics	NJ, USA
Calcitite	Zimmer	IN, USA
Osteograf	Ceramed	CO, USA

1.5 Tricalcium Phosphate (TCP)

The chemical formula of tricalcium phosphate (TCP) is: [7]

$$Ca_3(PO_4)_2$$

TCP belongs to the CaPs family and has a Ca/P ratio equal to 1.5 [7] and acts as a rich source of phosphorus and calcium that can be easily assimilated and absorbed inside the human body [69].
Thanks to its capability to interact positively with the hard tissue of the human body [19], TCP is currently used in different clinical applications in maxillofacial surgery, orthopaedics, dentistry [70].
TCP can have three different allotropic forms: β-TCP, α-TCP, α'-TCP. Concerning BTE applications, α' - TCP missing of practical interest due to it existence only at temperatures above 1430°C and when cooled below the transition temperature, it instantly returns to the allotropic form α-TCP [70].

β-TCP, the IUPAC name is tricalcium diorthophosphate β; other names are tricalcium bis(orthophosphate) β, calcium orthophosphate tribasic β [71].
α-TCP is also named tricalcium diorthophosphate α in the IUPAC momenclature; other names are tricalcium bis(orthophosphate) α, calcium orthophosphate tribasic α [71].
α-TCP can be regarded a high temperature phase of β-TCP; in fact, it is obtained from the latter at processing temperatures higher than 1125 °C.
Although they have the same chemical composition, β-TCP and α-TCP have differences in structure, solubility and density [70].
α-TCP has the crystalline structure of a monoclinic spatial group $P2_1/a$ and β-TCP has the crystalline structure of a rhombohedral spatial group [7].
In Figure 13 and in Table 11 are reported some properties for the three different allotropic forms of TCP, like number of formula units per cell (Z), parameters of cell (a, b, c, α β, and γ), theoretical density (D_{th}), cell volume (V), volume per formula unit (V_0), projections of the unit cells across the [0 0 1] direction [70].

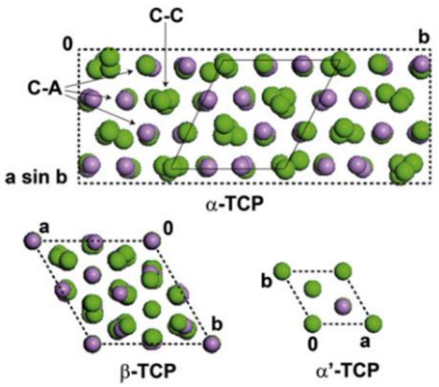

Figure 13. Schematic representation of the projections of the α-TCP, β-TCP, α'–TCP unit cells along the [0 0 1] direction P $^{5+}$ magenta, Ca^{2+} green, O^{2+} has not been represented for the sake of clarity, C-C cation-cation columns; C-A cation-anion column [70].

Table 11. Structural informations of α – TCP, β – TCP and α' – TCP [70].

Property	**$Ca_3(PO_4)_2$ polymorph**		
	β - $Ca_3(PO_4)_2$	**α - $Ca_3(PO_4)_2$**	**α' - $Ca_3(PO_4)_2$**
Symmetry	Rhombohedral	Monoclinic	Hexagonal
Space group	R3C	$P2_1/A$	$P6_3/mmc$
a (nm)	1.04352	1.2859	0.53507
b (nm)	1.04352	2.7354	0.53507
c (nm)	3.74029	1.5222	0.7684
α (°)	90	90	90
β (°)	90	126.35	90
γ (°)	120	90	120
V (nm^3)	3.5272	4.31	0.19052
V_0 (nm^3)	0.1680	0.180	0.19052
D_{th} (g cm^{-3})	3.066	2.866	2.702
Z	21	24	1

As evidenced by the V_0 and D_{th}, the structure of α - TCP is less dense than β - TCP but denser than α' - TCP [70].
α-TCP is formed by setting a temperature of 1125 °C or higher, β-TCP is created at a temperature of 900-1100 °C.
Differences in packing densities of α - TCP and β - TCP is coherent with their stability ranges of temperature [70].
β-TCP is stable at room temperature, and in general has a structure more stable than α-TCP but is still less stable than HA and, compared to this, has a faster degradation rate and higher solubility [7].
The α-TCP structure speeds up the degradation in a physiological environment than β-TCP [70].
This gives α-TCP an perfect material that can be substituted by new bone faster than other types of CaPs currently on the market.
α-TCP can also be used as a biodegradable carrier for the regulated release of cells, drugs, and macromolecules.
Comparing TCP and HA, we see that the dissolution rate decreases in the following order:[9]
HA > α-TCP > β-TCP.
This result confirms what was said above about HA, defined as one of the most stable calcium phosphates [70].
There are different approaches to modify the dissolution rate of α-TCP powders: modification of the contact area between the powders and the mixing liquid, modification of the saturation of the mixing liquid towards α-TCP, modification of the solubility of the powder in the mixing liquid.
β-TCP increases the proliferation of certain cells including bone marrow stromal and osteoblastic cells [7].
The characteristics of β-TCP make it an excellent component necessary for the production of several commercial biodegradable monophasic or biphasic biocereamics.
Also, α-TCP is stable at room temperature; its stability range is highly dependent on ion replacements [70].
α-TCP is biocompatible and is more soluble than β-TCP and hydrolyses rapidly in calcium - deficient hydroxyapatite. This makes α-TCP a useful material for preparing self-setting osteotransductive bone cements, composites for bone repair, and biodegradable bioceramics [70].

Conclusion

To date, bone tissue transplantation is one of the most performed in surgery, to try to cure and restore problems related to bone diseases (osteoporosis, osteogenesis imperfecta, osteoarthritis), fractures, musculoskeletal disorders or tumours.
Even if the bone has self-healing abilities, sometimes it is necessary to act externally to restore normal functionality. Among the different treatment options such as autografts, allografts and xenografts, autografts is considered the "gold standard" for repairing bone defects; but in some cases not even this is able to ensure complete and correct bone regeneration. These grafts in fact can provoke local infections, rejection by the transplanted organism and often there are not enough donors.
For these reasons, BTE is focusing on research and improvement of biomimetic synthetic materials to promote tissue regeneration.
The family of biomaterials used in BTE is very large, and includes metals, polymers and ceramic. Inside the bioceramic group, the family of CaPs is one of the most used, and in particulary HA and TCP.
CaPs have compositions and structural characteristics similar to natural bone and teeth and are characterized by high qualities of biocompatibility and bioactivity.
The great multidisciplinary field of TE has as main objective not so much the repair of the damaged tissue, but a complete regeneration of it, and for this reason CaPs are among the favourites for the realization of synthetic grafts.
Thanks to excellent osteoconductive and biodegradable properties, HA has been highly favoured in BTE and represents a great quantity of possible graft commercially available.
In several studies it has been demonstrated that HA is able to create a compatible environment for bone growth and regeneration, managing to integrate into the host tissue without causing an immune response and forming a bond with the surrounding tissue.
It can be used either as a metal prosthesis coating, as a powder or to make 3D scaffolds.
Like all ceramic materials, however, it has low tensile strength and an intrinsic brittleness that limits its application as a carrier material.
A number of methods have used for HAp powder synthesis such as hydrothermal method, emulsion method, sonochemical method, sol-gel synthesis and pyrolysis.
To date, the main biomedical applications of HA concern artificial substitutes for knees, teeth ligaments and tendons like repair for periodontal pathologies, augmentation and stabilization of the jawbone maxillofacial reconstruction, spinal fusion and bone fillers after tumour operation.
Great results were also reach in the application of drug delivery systems and carriers of bioactive peptides and/or various cell types.

References

[1] F. A. Grassi, U. E. Pazzaglia, G. Pilato, and G. Zatti, Manuale di ortopedia e traumatologia. 2012.

[2] C. Schmidleithner, "Master Thesis Additive Manufacturing of Tricalcium Phosphate Scaffolds for Bone Tissue Engineering," Vienna University of Technology.

[3] H. Qu, H. Fu, Z. Han, and Y. Sun, "Biomaterials for bone tissue engineering scaffolds: A review," RSC Adv., vol. 9, no. 45, pp. 26252–26262, 2019.

[4] C. J. Hernandez, "Cancellous bone," Handb. Biomater. Prop. Second Ed., pp. 15–21, 2016.

[5] E. Verné, "Slide corso Materiali per la Biongegneria: 'Biomateriali in ortopedia', Politecnico di Torino." Torino, Italy, 2018.

[6] A. Szcześ, L. Hołysz, and E. Chibowski, "Synthesis of hydroxyapatite for biomedical applications," Adv. Colloid Interface Sci., vol. 249, no. April, pp. 321–330, 2017.

[7] J. Jeong, J. H. Kim, J. H. Shim, N. S. Hwang, and C. Y. Heo, "Bioactive calcium phosphate materials and applications in bone regeneration," Biomater. Res., vol. 23, no. 1, pp. 1–11, 2019.

[8] H. E. Jazayeri et al., "The cross-disciplinary emergence of 3D printed bioceramic scaffolds in orthopedic bioengineering," Ceram. Int., vol. 44, no. 1, pp. 1–9, 2018.

[9] K. Rezwan, Q. Z. Chen, J. J. Blaker, and A. R. Boccaccini, "Biodegradable and bioactive porous polymer/inorganic composite scaffolds for bone tissue engineering," Biomaterials, vol. 27, no. 18, pp. 3413–3431, 2006.

[10] J. M. D. A. Rollo, R. S. Boffa, R. Cesar, D. C. Schwab, and T. P. Leivas, "Assessment of trabecular bones microarchitectures and crystal structure of hydroxyapatite in bone osteoporosis with application of the Rietveld method.," Procedia Eng., vol. 110, pp. 8–14, 2015.

[11] Q. Grimal and P. Laugier, "Quantitative Ultrasound Assessment of Cortical Bone Properties Beyond Bone Mineral Density," Irbm, vol. 40, no. 1, pp. 16–24, 2019.

[12] L. C. Gerhardt and A. R. Boccaccini, "Bioactive glass and glass-ceramic scaffolds for bone tissue engineering," Materials (Basel)., vol. 3, no. 7, pp. 3867–3910, 2010.

[13] N. A. Nawawi, A. S.F. Alqap, and I. Sopyan, "Recent Progress on Hydroxyapatite-Based Dense Biomaterials for Load Bearing Bone Substitutes," Recent Patents Mater. Sci., vol. 4, no. 1, pp. 63–80, 2011.

[14] P. Zioupos, R. B. Cook, and J. R. Hutchinson, "Some basic relationships between density values in cancellous and cortical bone," J. Biomech., vol. 41, no. 9, pp. 1961–1968, 2008.

[15] R. Bedini et al., "Rapporti ISTISAN 10/15 ISTITUTO SUPERIORE DI SANITÀ Analisi microtomografica del tessuto osseo trabecolare: influenza della soglia di binarizzazione sul calcolo dei parametri istomorfometrici," vol. 4915, no. 10, 2010.

[16] D. Ke and S. Bose, "Effects of pore distribution and chemistry on physical, mechanical, and biological properties of tricalcium phosphate scaffolds by binder-jet 3D printing," Addit. Manuf., vol. 22, no. July 2017, pp. 111–117, 2018.

[17] "Bone remodelling." [Online]. Available: https://www.york.ac.uk/res/bonefromblood/background/boneremodelling.html. [Accessed: 11-May-2020].

[18] K. Lin, R. Sheikh, S. Romanazzo, and I. Roohani, “3D printing of bioceramic scaffolds-barriers to the clinical translation: From promise to reality, and future perspectives,” Materials (Basel)., vol. 12, no. 7, pp. 1–20, 2019.
[19] P. Miranda, E. Saiz, K. Gryn, and A. P. Tomsia, “Sintering and robocasting of β-tricalcium phosphate scaffolds for orthopaedic applications,” Acta Biomater., vol. 2, no. 4, pp. 457–466, 2006.
[20] V. Campana et al., “Bone substitutes in orthopaedic surgery: from basic science to clinical practice,” J. Mater. Sci. Mater. Med., vol. 25, no. 10, pp. 2445–2461, 2014.
[21] W. Wang and K. W. K. Yeung, “Bone grafts and biomaterials substitutes for bone defect repair: A review,” Bioact. Mater., vol. 2, no. 4, pp. 224–247, 2017.
[22] F. Baino et al., “Processing methods for making porous bioactive glass-based scaffolds—A state-of-the-art review,” Int. J. Appl. Ceram. Technol., vol. 16, no. 5, pp. 1762–1796, 2019.
[23] T. Albrektsson and C. Johansson, “Osteoinduction, osteoconduction and osseointegration,” Eur. Spine J., vol. 10, pp. S96–S101, 2001.
[24] N. Eliaz and N. Metoki, “Calcium phosphate bioceramics: A review of their history, structure, properties, coating technologies and biomedical applications,” Materials (Basel)., vol. 10, no. 4, pp. 1–104, 2017.
[25] G. Rh. Owen, M. Dard, and H. Larjava, “Hydoxyapatite/beta-tricalcium phosphate biphasic ceramics as regenerative material for the repair of complex bone defects,” J. Biomed. Mater. Res. - Part B Appl. Biomater., vol. 106, no. 6, pp. 2493–2512, 2018.
[26] L. Zhang, G. Yang, B. N. Johnson, and X. Jia, “Three-dimensional (3D) printed scaffold and material selection for bone repair,” Acta Biomater., vol. 84, pp. 16–33, 2019.
[27] R. A. Horowitz, Z. I. V Mazor, C. Foitzik, H. Prasad, M. Rohrer, and A. D. Y. Palti, “β - Tricalcium Phosphate As Bone Substitute Material,” J. Osseointegration, vol. 1, no. 1, pp. 60–68, 2010.
[28] Galvan, F. R., V. Barranco, J. C. Galvan, S. Batlle, Sebastian FeliuFajardo, and García, “Bone Graft Types,” Intech, vol. 1, pp. 1–13, 2016.
[29] A. Tampieri, S. Sprio, A. Ruffini, G. Celotti, I. G. Lesci, and N. Roveri, “From wood to bone: Multi-step process to convert wood hierarchical structures into biomimetic hydroxyapatite scaffolds for bone tissue engineering,” J. Mater. Chem., vol. 19, no. 28, pp. 4973–4980, 2009.
[30] C. Koski, B. Onuike, A. Bandyopadhyay, and S. Bose, “Starch-hydroxyapatite composite bone scaffold fabrication utilizing a slurry extrusion-based solid freeform fabricator,” Addit. Manuf., vol. 24, no. August, pp. 47–59, 2018.
[31] C. Schmidleithner, S. Malferarri, R. Palgrave, D. Bomze, M. Schwentenwein, and D. M. Kalaskar, “Application of high resolution DLP stereolithography for fabrication of tricalcium phosphate scaffolds for bone regeneration,” Biomed. Mater., vol. 14, no. 4, pp. 1–11, 2019.
[32] R. M. Concetta, “Biomateriali ceramici e compositi,” Università degli studi di Lecce.
[33] S. V. Dorozhkin, “Calcium orthophosphate bioceramics,” Ceram. Int., vol. 41, no. 10, pp. 13913–13966, 2015.
[34] E. Verné, “Slide Corso Materiali per la Bioingegneria: ‘Bioceramici’, Politecnico di Torino.” Torino, Italy, 2018.
[35] W. Cao and L. L. Hench, “Bioactive materials,” Ceram. Int., vol. 22, no. 6, pp. 493–507, 1996.

[36] R. Albulescu et al., “Comprehensive In Vitro Testing of Calcium Phosphate-Based Bioceramics with Orthopedic and Dentistry Applications,” Materials (Basel)., vol. 10, pp. 1–41, 2019.
[37] A. R. Amini, C. T. Laurencin, and S. P. Nukavarapu, “Bone tissue engineering: Recent advances and challenges,” Crit. Rev. Biomed. Eng., vol. 40, no. 5, pp. 363–408, 2012.
[38] D. Mohamad Yunos, O. Bretcanu, and A. R. Boccaccini, “Polymer-bioceramic composites for tissue engineering scaffolds,” J. Mater. Sci., vol. 43, no. 13, pp. 4433–4442, 2008.
[39] M. Roy, A. Bandyopadhyay, and S. Bose, Ceramics in Bone Grafts and Coated Implants. Elsevier Inc., 2017.
[40] S. M. Best, A. E. Porter, E. S. Thian, and J. Huang, “Bioceramics: Past, present and for the future,” J. Eur. Ceram. Soc., vol. 28, no. 7, pp. 1319–1327, 2008.
[41] S. V. Dorozhkin, “Multiphasic calcium orthophosphate (CaPO4) bioceramics and their biomedical applications,” Ceram. Int., vol. 42, no. 6, pp. 6529–6554, 2016.
[42] M. Ebrahimi, M. G. Botelho, and S. V. Dorozhkin, “Biphasic calcium phosphates bioceramics (HA/TCP): Concept, physicochemical properties and the impact of standardization of study protocols in biomaterials research,” Mater. Sci. Eng. C, vol. 71, no. November, pp. 1293–1312, 2017.
[43] I. Denry and L. T. Kuhn, “Design and characterization of calcium phosphate ceramic scaffolds for bone tissue engineering,” Dent. Mater., vol. 32, no. 1, pp. 43–53, 2016.
[44] B. De Carvalho, E. Rompen, G. Lecloux, P. Schupbach, and E. Dory, “Effect of sintering on in vivo biological performance of bovine hydroxyapatite.,” Materials (Basel)., pp. 1–14, 2019.
[45] K. Søballe, “Hydroxyapatite ceramic coating for bone implant fixation: Mechanical and histological studies in dogs,” Acta Orthop., vol. 64, no. S255, pp. 1–58, 1993.
[46] M. T. Islam, R. M. Felfel, E. A. Abou Neel, D. M. Grant, I. Ahmed, and K. M. Z. Hossain, “Bioactive calcium phosphate–based glasses and ceramics and their biomedical applications: A review,” J. Tissue Eng., vol. 8, pp. 1–16, 2017.
[47] P. N. Kumta, C. Sfeir, D. H. Lee, D. Olton, and D. Choi, “Nanostructured calcium phosphates for biomedical applications: Novel synthesis and characterization,” Acta Biomater., vol. 1, no. 1, pp. 65–83, 2005.
[48] B. Wopenka and J. D. Pasteris, “A mineralogical perspective on the apatite in bone,” Mater. Sci. Eng. C, vol. 25, no. 2, pp. 131–143, 2005.
[49] R. Astala and M. J. Stott, “First principles investigation of mineral component of bone: CO3 substitutions in hydroxyapatite,” Chem. Mater., vol. 17, no. 16, pp. 4125–4133, 2005.
[50] Y. Javadzadeh and S. Hamedeyaz, “Hydroxyapatite-Based Materials: Synthesis and Characterization,” Technol. InsightsBiomedical Eng. - Front. Challenges, vol. i, no. Biomedical Engineering, p. 13, 2014.
[51] A. N. Wang et al., “Study on the Blend Film Prepared by Chitosan and Gelatin,” Adv. Mater. Res., vol. 201–203, pp. 2866–2869, 2011.
[52] A. Bhattacharjee et al., “Crystal chemistry and antibacterial properties of cupriferous hydroxyapatite,” Materials (Basel)., vol. 12, no. 11, pp. 1–17, 2019.
[53] C. C. Silva et al., “Properties and in vivo investigation of nanocrystalline hydroxyapatite obtained by mechanical alloying,” Mater. Sci. Eng. C, vol. 24, no. 4, pp. 549–554, 2004.

[54] M. Sadat-Shojai, M. T. Khorasani, E. Dinpanah-Khoshdargi, and A. Jamshidi, “Synthesis methods for nanosized hydroxyapatite with diverse structures,” Acta Biomater., vol. 9, no. 8, pp. 7591–7621, 2013.
[55] B. Li and T. Webster, Orthopedic biomaterials: Advances and applications. USA, 2018.
[56] J. Zhan, Y. H. Tseng, J. C. C. Chan, and C. Y. Mou, “Biomimetic formation of hydroxyapatite nanorods by a single - crystal - to - single -crystal transformation,” Adv. Funct. Mater., vol. 15, no. 12, pp. 2005–2010, 2005.
[57] K. S. Tenhuisen and P. W. Brown, “Formation of calcium-deficient hydroxyapatite from α-tricalcium phosphate,” Biomaterials, vol. 19, pp. 2209–2217, 1998.
[58] H. C. Park, D. J. Baek, Y. M. Park, S. Y. Yoon, and R. Stevens, “Thermal stability of hydroxyapatite whiskers derived from the hydrolysis of α-TCP,” J. Mater. Sci., vol. 39, no. 7, pp. 2531–2534, 2004.
[59] I. Sopyan, R. Singh, and M. Hamdi, “Synthesis of nano sized hydroxyapatite powder using sol-gel technique and its conversion to dense and porous bodies,” Indian J. Chem. - Sect. A Inorganic, Phys. Theor. Anal. Chem., vol. 47, no. 11, pp. 1626–1631, 2008.
[60] “Novel Biomaterials for Regenerative Medicine - Google Libri.” [Online]. Available: https://books.google.it/books?id=_s10DwAAQBAJ&pg=PA345&lpg=PA345&dq=emulsion+method+for+HA&source=bl&ots=VSdF2fqyZa&sig=ACfU3U1Sx_msmu_F7wCeIQeLYLZlcMGOSA&hl=it&sa=X&ved=2ahUKEwiVmM24-LLpAhXpkosKHVaWATsQ6AEwBHoECAkQAQ#v=onepage&q=emulsion method for HA&f=. [Accessed: 14-May-2020].
[61] A. B. Hazar Yoruç and Y. Ipek, “Sonochemical synthesis of hydroxyapatite nanoparticles with different precursor reagents,” Acta Phys. Pol. A, vol. 121, no. 1, pp. 230–232, 2012.
[62] W. Suchanek and M. Yoshimura, “Processing and properties of hydroxyapatite - based biomaterials for use as hard tissue replacement implants,” J. Mater. Res., vol. 13, no. 1, pp. 94–117, 1998.
[63] Galvan, F. R., V. Barranco, J. C. Galvan, S. Batlle, Sebastian FeliuFajardo, and García, “A Brief Introduction to Porous Ceramic,” Intech, vol. i, p. 13, 2016.
[64] S. Dorozhkin, “Medical Application of Calcium Orthophosphate Bioceramics,” Bio, vol. 1, no. 1, pp. 1–51, 2011.
[65] A. Haider, S. Haider, S. S. Han, and I. K. Kang, “Recent advances in the synthesis, functionalization and biomedical applications of hydroxyapatite: a review,” RSC Adv., vol. 7, no. 13, pp. 7442–7458, 2017.
[66] V. S. Kattimani, S. Kondaka, and K. P. Lingamaneni, “Hydroxyapatite -- Past, Present, and Future in Bone Regeneration,” Bone Tissue Regen. Insights, vol. 7, pp. 9–19, 2016.
[67] S. R. Motamedian, “Smart scaffolds in bone tissue engineering: A systematic review of literature,” World J. Stem Cells, vol. 7, no. 3, p. 657, 2015.
[68] Galvan, F. R., V. Barranco, J. C. Galvan, S. Batlle, Sebastian FeliuFajardo, and García, “Tuned Hydroxyapatite Materials for Biomedical Applications,” Biomater. - Phys. Chem. - New Ed., vol. i, pp. 88–104, 2016.
[69] A. M. H. Ng et al., “Differential osteogenic activity of osteoprogenitor cells on HA and TCP/HA scaffold of tissue engineered bone,” J. Biomed. Mater. Res. - Part A, vol. 85, no. 2, pp. 301–312, 2008.

[70] R. G. Carrodeguas and S. De Aza, “α-Tricalcium phosphate: Synthesis, properties and biomedical applications,” Acta Biomater., vol. 7, no. 10, pp. 3536–3546, 2011.
[71] S. V. Dorozhkin, “Calcium orthophosphates: occurrence, properties, biomineralization, pathological calcification and biomimetic applications.,” Biomatter, vol. 1, no. 2, pp. 121–164, 2011.

Chapter 2
Rapid Prototyping Techniques for Scaffolds Manufacturing

As introduced in the previous chapter, advanced BTE approaches rely on synthetic grafts for the treatment and regeneration of major bone defects in order to overcome common limits associated to the implantation of grafts of natural origin; here, the attention is focused on porous ceramic scaffolds.
In the present chapter, an overview on ceramic scaffolds for bone tissue engineering will be provided, paying special attention to additive manufacturing technologies. The functional and structural complexity of natural bone, indeed, makes the design ofscaffolds a complex challenge as both chemical and structural properties have to meet very specific requirements, i.e..adequate support properties and a macro- and micro- porous structure to promote angiogenesis and cell colonization.
Many fabrication techniques are currently available for the production of porous artificial matrixes. Among these, rapid prototyping turned out to be one of the most promising for the development of mechanically competent and structurally highly-defined scaffolds with tailored properties for bone tissue engineering applications.

2.1 Scaffolds for bone Repair: basic definition

The scaffold, also known as template and/or artificial extracellular matrix, is a biocompatible 3D structure that acts as resorbable extracellular support matrix, [1] on which cells could attach, proliferate and differentiate in order to synthetize new bone tissue until the complete filling of the original bone defect [1],[2].
Andrés Segovia, a Spanish classical guitarist, is managed to explain the role of scaffold with these worlds [3]:

"When one puts up a building, he makes an elaborate scaffold to get everything into its proper place. But when one takes the scaffold down, the building must stand by itself with no trace of the means by which it was erected. That is how a musician should work."

In Table 1 the main functions that should be performed by a scaffold intended for tissue engineering applications are summarized.

Table 1. Functions of the scaffold, adapted from [4].

Primary Functions of Scaffold
Substrate for cell adhesion
Delivery vehicle for exogenous cell, growth factors and genes
Temporary mechanical support for new tissue gowth
Barrier to the infiltration of surrounding tissue that may hinder the process of regeneration
Maintenance of the shape of the defect by avoiding distortion

Given the sensitive and complex nature of a biological system, scaffolds have to satisfy multiple requirements at the same time, as depicted in Figure 1 [5].

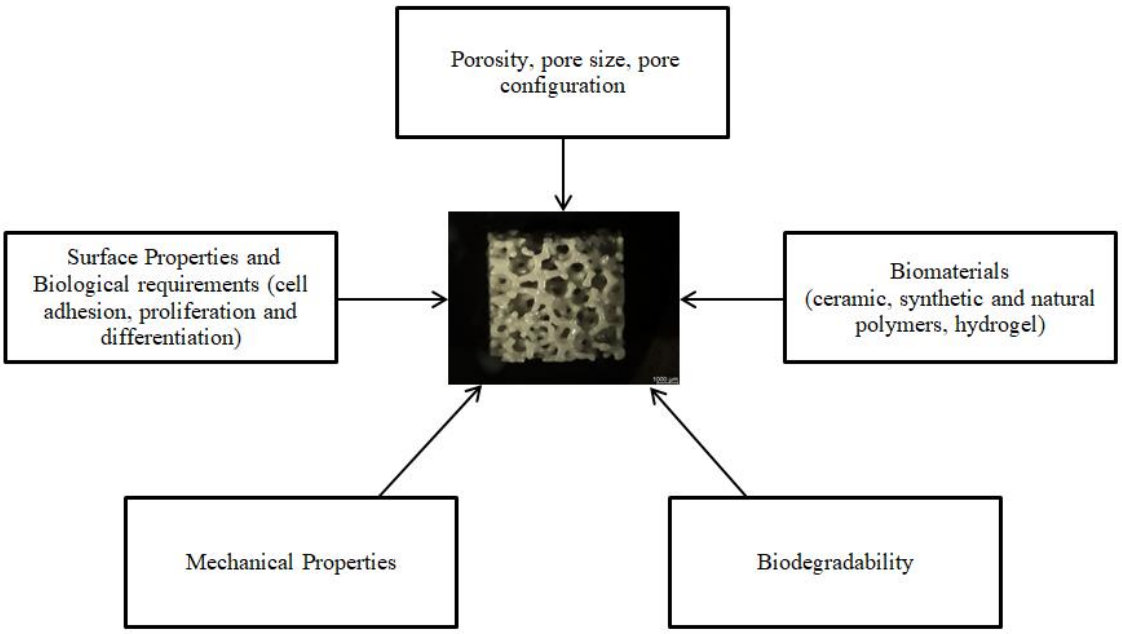

Figure 1. Key factors involved in the design of scaffolds for BTE.

Osteoconductivity, controlled biodegradability, biocompatibility [6] are important characteristics of tissue - engineered scaffolds for bone defect repair, where new tissue growth and scaffold resorption are concurrent events leading to the replacement of the scaffold by newly formed bone. Highly biocompatible materials have to be used in order to obviate an inflammatory response or cytotoxicity within the body [3].

In addition, the scaffold must have structural properties to provide proper mechanical support over the whole healing process [6].

Scaffold must have sufficient biological affinities to promote the integration and growth of cells [2] and damaged tissues [7]; with suitable porosity features, necessary to allow cell migration, diffusion of nutrients and vascularization [3].

All parameters must be chosen according to the implant site; in fact, in the skeletal system, depending on the anatomical position, bone tissue exybited different structural properties. Therefore, if surgery on the spongy bone is required, highly porous and durable scaffolds will be preferable; on the other hand, if the problem concerns the cortical bone, scaffolds with low porosity and oriented strut will be required [7].
In the following section, scaffolds requirements will be discussed in detail.

2.1.1 Scaffold Requirements

2.1.1.1 Biocompatibility

This is the first criterion that every tissue - engineered scaffold must meet [6].
William defines the term biocompatibility as:

"*the capability of a material to facilitate natural cellular and molecular activity within a scaffold in the absence of systemic toxicity*" [8].

Biocompatible scaffolds allow cells to adhere, migrate and proliferate on their surface without the risk of triggering dangerous inflammatory responses [6], and/or potentially toxic effects, both locally and systemically [9].
Good biocompatibility also promotes osteoconductivity, osteoblast proliferation and osteoinductivity [8].
In order for the scaffold to be biocompatible it is necessary to carefully choose the material with which it is manufactured. Suitable materials for BTE scaffolds must bind firmly to the natural bone in situ and promote new bone growth [9].
It has been shown that scaffolds in HA are highly biocompatible and improve the tissue repair process: thanks to the release of calcium and phosphate ions, osteogenesis is greatly accelerated [8].
Methods for controlling the scaffold biocompatibility can be found in ISO 10993 – 1 [10].

2.1.1.2 Porosity and Pore Size

Pore size and porosity percentage of the scaffolds is an essential parameter to get a physiological tissue development [11]. The ideal scaffold for cancellous bone tissue should have an interconnected porous structure with porosity > 80% [2], where more than 60% of the pores should have a size between 100 - 400 μm and at least 20 % is expected to be smaller than 20 μm [3].
Porosity percentage and pore size directly affect the osteoinductive and osteoconductive capabilities of the scaffold [12].
A suitable porosity range confers to the confers to the scaffold adequate mass transport properties for cell migration, attachment and interaction with the biological environment [6], as well as the passage of nutrients and bioactive molecules. Moreover, it has been demonstrated that suitable porosity features could improve vascularization and spatial organization between cell growth and ECM production, thus leading to a considerable enhancement of the biomineralization process [8].

Large pores (around 200-300 μm), in fact, lead to direct osteogenic pathways [2],[9]. The prevailing opinion in the literature is that in order to allow greater cell migration and proliferation, and the consequent formation of new tissue, the pore size must be between 200-400 μm [13].
Smaller pores, instead, (closer 100 μm) were found to be beneficial to chondrogenesis [14].
However, too small pores, lead to poor vascularisation [11] and limited cell migration, causing the formation of cell capsules around the edges of the scaffold [9].
It is, however, necessary for the pores not to be too large, as this would excessively decrease the mechanical resistance of the final product [9], [6].
The ideal degree of porosity must be found so as to allow sufficiently high permeability and interconnecivity for nutrient supply and waste removal and adequate stiffness and resistance to loads transmitted from the healthy bone adjacent to the scaffold [2].
Interconnectivity (Figure 2) is a key requirement to ensure the transport of nutrients and the elimination of waste products [15].
An in vivo study with HA scaffolds has shown that low pore interconnection only enables pore penetration and chondroidal tissue formation but does not guarantee proper bone tissue growth [15].
The shape of the pores can also influence the mechanical and osteogenic properties of the scaffold [6].
Gong et al. performed fatigue tests (cyclic stress - strain) on scaffolds with triangular and circular pores, with a total porosity of about 60%. The study found that scaffolds with circular pores are more resistant than those with triangular pores [6].

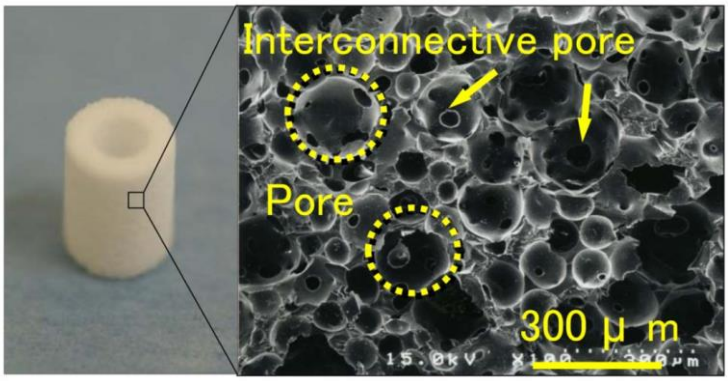

Figure 2. Pores and interconnection of pores showed in HA scaffold [16].

Optical microscopy (light or electron microscopy technique) or microcomputer tomography can be applied in the middle parts of the scaffold to investigate the macro and micropores [10].

2.1.1.3 Mechanical Properties

For the scaffold to be functional, it must have biomechanical properties comparable to those of the adjacent healthy bone [12],[8].
The scaffold must maintain a certain stiffness until the newly formed tissue has achieved sufficient structural integrity to physically support itself [8].
It must have a Young's module similar to that of natural bone in order to avoid stress shielding and promote early tissue regeneration [17].

Good mechanical properties could be obtained by building anisotropic scaffolds with oriented pores [9]. Pore size and interconnection and architecture affect the mechanical properties of the scaffolds [15].
For example, studies on HA scaffolds have shown that decreasing the pore size results in higher compressive strength [15].
The compressive strength is the most common test done for ceramic scaffolds and it is used to calculate the stress – strain curve [18].
In accordance with ASTM F2883-11, for implantable ceramic scaffolds, compressive strength would be tested according to ASTM C1424 for advanced ceramics [18].
For example, to replace cortical bone a good scaffold should have a compressive strength ~ 130 - 180 MPa and Young's module ~ 12 -18 GPa, as it is described in Chapter 1).
In addition, it has been proven that the mechanical strength of the scaffold affects the mechanotransduction properties of the bone cells attached to the surface. There seems to be a correlation between mechanotransduction and the potential osteoinductive properties of the scaffold [12].
Not all anchorage - dependent cells respond similarly to scaffold stiffness[11]:
endothelial cells, for example, migrate and proliferate more easily on more rigid substrates [11].

2.1.1.4 Biodegradability

As the tissue regenerates, the scaffold must degrade in a controlled manner over time [8].
The biodegradability of the scaffold depends on the type of material and its application: TCP-based scaffolds show a rate of bioresorption similar to bone neoformation, whereas HA scaffolds are generally characterized by better chemical durability [8].
Usually the degradation of the biomaterial is influenced by the presence of organic ions in physiological fluids [7].
The rate of scaffold degradation may change depending on the different printing mode used. It will therefore be necessary to test different production methods to find the optimal one [8]. It can be calculated in accordance with ISO 10993-14 [18].

2.1.1.5 Surface properties and interaction with cells

The scaffold needs to be made in complex and even irregular shapes. L'osso umano ha una struttura molto complessa dal livello della nanoscale fino alla macroscale. The scaffold should serve as a model for natural bone growth and should therefore imitate the hierarchical structure of natural bone. With regard to cortical bone, for example, its internal architecture should be similar to the small vascular channels, Volkmann's channels and the gaps in the osteocytes and Hanversian channels [9].
As already mentioned, the scaffold needs careful design in order to achieve a high level of interconnected porosity [9].
Several studies have shown that the characteristics of the scaffold surface affect the amount, type and conformation of proteins and cells that will adhere to it [9].
A rough surface may improve cell adhesion, but excessive roughness must be avoided, or the cells may fail to develop focal adhesion plaques [4].

The performance of a scaffold depends on the interaction between its surface and biological fluids and is often mediated by certain proteins that are absorbed by the biological fluid [19].
Chemistry, roughness and surface topography strongly influence the protein layer on which the formation of surface bonds directly aimed at binding only certain types of cells depends.
Proteins create a specific interface to which cells can respond to the macrostructure of the scaffold as well as the chemical properties of the surface determine how cells attach to the structure [19].
Surfaces with nanometric topography increase the availability of proteins and amino acids by promoting cell adhesion to a large extent [19].
Some examples in the literature suggest incorporating growth factors into scaffolds because they can improve and speed up the growth of new bone. in fact, morphogenic bone proteins (BMPs) help the development of both bone and cartilage and can trigger the differentiation and proliferation of osteoprogenitor cells. vascular endothelial growth factor (VEGF) has often been used because it can improve blood vessel formation [14].
Finally, the synthesis of the material and the production of the scaffold should allow the sterilisation process to be easily marketable [2].

Table 2. summarises the main features of the scaffold and their effects.

Table 2. Characteristics of the scaffold and their desirable effects [14].

Scaffold Requirements	**Desirable Features**
Biocompatibility	• Non-toxic breakdown products • Non-inflammatory scaffold components, avoiding immune rejection
Biodegradability	• Biodegradability • Controlled scaffold degradation which can complement tissue ingrowth whilst maintaining sufficient support • Degradable by host enzymatic or biological processes • Allows invading host cells to produce their own extracellular matrix
Bioactivity	• Scaffold materials that can interact with and bind to host tissue • Osteoconductive and osteoinductive properties • Inclusion of biological cues and growth factors to stimulate cell ingrowth, attachment and differentiation
Scaffold Architecture	• Interconnected pores allowing diffusion and cell migration • Microporosity to present a large surface area for cell-scaffold interactions • Macroporosity to allow cell migration and invasion of vasculature • Sufficient porosity to facilitate cell ingrowth without weakening mechanical properties • Pore size tailored to target tissue and cells • Inbuilt vascular channels to enhance angiogenesis *in vivo*
Mechanical Properties	• Compressive, elastic and fatigue strength comparable to host tissue allowing cell mechanoregulation to occur and structural integrity to remain *in vivo* • Scaffold material that can be readily manipulated in the clinical environment to treat individual patient bone defects

2.2 Conventional Methods Vs Non - Conventional Methods

Scaffold manufacturing techniques could be divided into two main groups: conventional methods and non-conventional methods (or Additive Manufacturing techniques / Rapid Prototyping techniques) [9] (Table 3).
Scaffolds can be made using conventional techniques such as freeze - drying, gas foaming, solvent casting and particulate leaching, sol-gel method, phase separation (TIPS, DIPS, RIPS) [13], melt, dry, wet-spinning and electro-spinning [1].
In general, conventional techniques include all those techniques that are not based on a CAD/CAM design [9].
However, these methods have several limitations, the first of which is poor reproducibility [1][13], and the inability to obtain scaffolds with a precise internal porosity, geometry and interconnectivity [6].
From the biological point of view, this could be a severe drawback as a random and uncontrolled 3D-structures could determine an heterogeneous distribution of cells, causing uneven tissue growth [20].
The most common conventional manufacturing technique are described below.

Foaming methods
They are based on the use of a foaming agent to create air bubbles that will then generate porosity. After preparing a colloidal suspension (or slurry), pores are created, thanks to the porogen, by injecting the gas directly, or by generating gas through a chemical reaction or through thermal decomposition and the addiction of surfactants [9].
Foaming methods include techniques such as: Gel cast foaming, H_2O_2 foaming or Sol–gel foaming. However, all these techniques do not guarantee a scaffold with good mechanical properties and, above all, do not assure the high porous interconnectivity required for successful bone implants [9].
Q.Chen et al., have focused their studies on the creation of highly porous foams with ceramic material and surfactant. They used foaming sol-gel derived BG created with the inclusion of a surfactant combined with mechanical agitation [21].

Phase separation methods
They usually are divided in three groups depending on the principal parameters that cause demixing of the solution [22]; for example, temperature induced phase separation methods (TIPS) are based on the change of the temperature at the interface of the solution [22]. For diffusion induced phase separation methods (DIPS) are necessary to add a vapour or a liquid (a non solvent); reaction induced phase separation (RIPS) are based on a chymical reaction is induced to lead to the phase separation the original polymer solution; in this class precipitation induced by a change in pH are also included. [22].
TIPS is mainly used to obtain polymeric scaffolds but also polymer composite scaffolds with porous glass nanoparticles to increase bioactivity [9].
TIPS is based on the change in solubility between two different polymers as a function of temperature: two polymers may be soluble in each other at a given temperature but completely insoluble at a lower temperature. Therefore, if a solution of these polymers is made and then the

solution is cooled below the critical temperature of the solution, they will separate and form two distinguishable phases: one less rich in polymer and one richer in polymer. The less polymer-rich phase will be removed to obtain the porous structure [9].
TIPS is used to obtain porous scaffold with pore diameter from 1 to 100 μm and porosity over 95%. For example, K. Szustakiewicz et al., obtained porous scaffold based on synthetic HA and poly(L-lactide) (PLLA) using TIPS supported by salt leaching process (SL) [23].
Maquet et al., have built a scaffold of bioreabsorbable polymers (poly(D,L-lactide) (PDLLA) and poly(latex-coglycolide) (PLGA)) and 45S5 Bioglass®. They constructed two different sets of samples by varying the amount of glass powder; in both cases they obtained a porosity greater than 90% vol [24].
Italian researchers have created bioresorbable and bioactive porous scaffold based on poly(3-hydroxybutyrate) (PHB) and HA particles. These scaffolds are able to sustain MC3T3-E1 and cytocompatible; they have a good porosity and high bioactivity thanks to the HA presence [25].

Spinning methods
They allow obtaining nano- or micrometric fibres, useful especially for the regeneration of nerves, and are divided into dry, wet, melt spinning methods and electrospinning [22].
Melt-spinning technique uses a melted polymer that is extruded through a die with a desired geometry section, while dry spinning and wet spinning use concentrated solutions that are extruded through a die with a section of the desired geometry. For both methods it is necessary to remove the solvent to obtain the fibres.
Electrospinning can use both polymer solutions in volatile solvent (electrospinning solution) and polymer melt (melt electrospinning). It is a versatile technique that allow to make continuous fibres from submicron to nanometric diameters [22].
An interesting study has seen the realization of scaffolds in Bioglass with biodegradable nanofibrous coatings obtained with electro-spinning. The composite scaffold obtained by combining bioactive glass-ceramic and electrospun polymer (PCL-PEO, P(3HB), PHBV) nanofibers allowed the formation of a layer of nanostructured HA in contact with physiological fluids and the possibility of controlled drug release [26].
Y. Hong et al., have made a hierarchal nanoporous Bioactive Glass (BG) fiber membranes with electro-spinning technique and P123-PEO co-template. Thanks to this technique micro, meso and macro pores are obtained and BG fibers are well arranged into 3D macroporous membranes at the macroscopic scale. These membranes have potential application for BTE or drug delivery [27].

Thermal consolidation of particle
Methods that are part of this group are characterized by the use of sacrificial particles that will be added to the green body that will be sintered. These particles will form pores upon thermal degradation and they are typically polymers or of synthetic (e.g.PE particles) or natural origin (e.g. rice husk or starch) [9]. These techniques are generally not expensive but usually they do not allow obtaining highly porous scaffolds and good interconnection among pores [9].

Sponge replication method

This method is based on the use of porous template of natural material (e.g. marine sponge) or synthetic material (e.g. polyurethane sponge) with a slurry [28] to create glass and glass ceramic shelves with a high level of porosity and obtain a structure more similar to bone. The idea is to recreate the structure of the foam by covering the walls and the struts using a glass (ceramic) slurry [9].

The sponge is the organic phase of the scaffolds and only serves as a model for the inorganic phase, in fact it will be completely removed during the process [9].

The scaffolds obtained in this way will have to undergo a double heat treatment: one to eliminate the organic phase and one to compact the ceramic/glass phase [9]. In this way a porous ceramic structure is obtained showing the same architecture like the sacrificial template (positive replica) [28].

This method allows to obtain scaffolds with structures very similar to natural bone trabecular structures and high levels of porosity (about 90 vol.%) but often these scaffolds have poor mechanical properties [9]. Usually foam replication method is used to build porous scaffolds of glass-ceramic, biphasic CaPs and HA [29].

A problem of this technique is the capability to create a solid network with high density and good mechanical properties [29].

In 2006 Chen et al., used a PU foam as a sacrificial model a slurry of commercial 45S5 Bioglass® and PVA powders as a binder. This was one of the first scaffolds successfully obtained with this method: it has a very high porosity and interconnected and open macropores between 510-720 μm which make it very similar to spongy bone but at the same time too easy to be used in BTE application (compressive strength between 0.1-0.4 MPa) [30].

G. Tripathi et al., have used this method to build a HA scaffold with interconnected oval pores (diameter: 100-300 μm and wall thickness ~50 μm). The homogeneous distribution of pores and the pore wall thickness provided larger surface area to help protein attachment and cell proliferation [31].

Q. Fun et al., prepared porous scaffold of 13-93 bioactive glass with porosity of 85 ± 2% and pore size of 100–500. In this case, they have obtained a more resistant scaffold than other examples in literature for HA and bioactive glass-ceramic prepared by the same method and with the same percentage of porosity. In addition, these scaffolds showed great property to support the proliferation of MC3T3-E1 preosteoblastic cells [29].

Wu et al., tried to improve the mechanical properties of the scaffolds obtained with sponge replica method by depositing a silk coating on the struts of the template; but the results obtained from the compressive strength test remained low .

Table 3. Conventional methods vs Non – Conventional methods [15],[9],[22], [32], [33].

Conventional methods	Non – Conventional methods
- Inability to obtain a scaffold with a precise architecture and controlled porosity - Inadequate to create patient-specific scaffolds - Techniques strongly dependent operators - Usually fast and not too expensive techniques	- Fabrication of scaffolds with a complex internal structure and patient – specific geometry - Possibility to use heterogeneous materials - Industrial scalability - Sometimes limited choice of materials - High cost of the process
METHODS: Solvent casting and particulate leaching Gas foaming Freeze – drying Sol - gel Melt, dry, wet – spinning and electro – spinning Phase separation (TIPS, DIPS, RIPS) Plasma spraying Sponge replication method	METHODS: Select laser sintering (SLS) Stereolithography (SLA) Fused deposition modelling (FDM) Laminated object manufacturing (LOM) Solid ground curing 2 – photon polimerization Robocasting Ink – jet printing 3D printing (3DP) 3D fiber deposition

Despite the improvements that have been made over the years, conventional techniques are still very much dependent on the process rather than the design; and they have inherent limitations that make it impossible to control the architecture of the scaffolds [4].
As a consequence, researchers, since the second half of the 1980s [34], have been developing Rapid Prototyping (RP) as a valid alternative to obtain detailed and extensive control on the manufacturing process [4], [35].

2.3 Rapid Prototyping (RP) techniques

During the last two decades, with the development of Rapid Prototyping (RP) techniques, a great number of tissue - engineered scaffolds have been created for clinical applications using new materials and innovative technologies [6]. These methods make it now possible to create scaffolds for a targeted regeneration of hard tissue, quickly and also patient-specific or generally marketable [8].
In literature, Rapid Prototyping (RP) techniques Additive Manufacturing (AM) are frequently used as synonyms; and these terms refer to all those non-conventional techniques where 3D - structures

are produced by adding material "layer-by-layer" [4],[32]. Unlike conventional techniques, RP builds the object by selectively adding the material layer after layer. Each layer represents the shape of the cross-section of the model at a specific layer [36].
RP techniques offer the possibility of controlling the architecture of the scaffold (shape, size, interconnectivity, branches, geometry, and pore orientation). Biomimetic structures that vary in material composition and design can be realised, thus improving the control of mechanical properties, biological effects, and degradation rate of the scaffold [36].
RP techniques use different technologies, similar to each other in terms of main procedures which are usually divided into 5 phases [37]:

1. Creation of the CAD model
2. Converting the CAD model into STL files
3. Slicing of the STL file
4. The RP apparatus creates the scaffold one layer at a time
5. Post-Processing (if necessary)

The creation of file CAD is one of the fundamental steps for the build of bone scaffolds with RP technique.
The CAD file can be created from magnetic resonance imaging (MRI) but especially computed tomography (CT) images are used, as they allow to obtain accurate 3D reconstructions at a very high resolution [17].
If the CT images directly represent the patient's defect, you can create a 3D image of the bone defect to be treated in order to print out a patient-specific scaffold (Figure 3) [36].

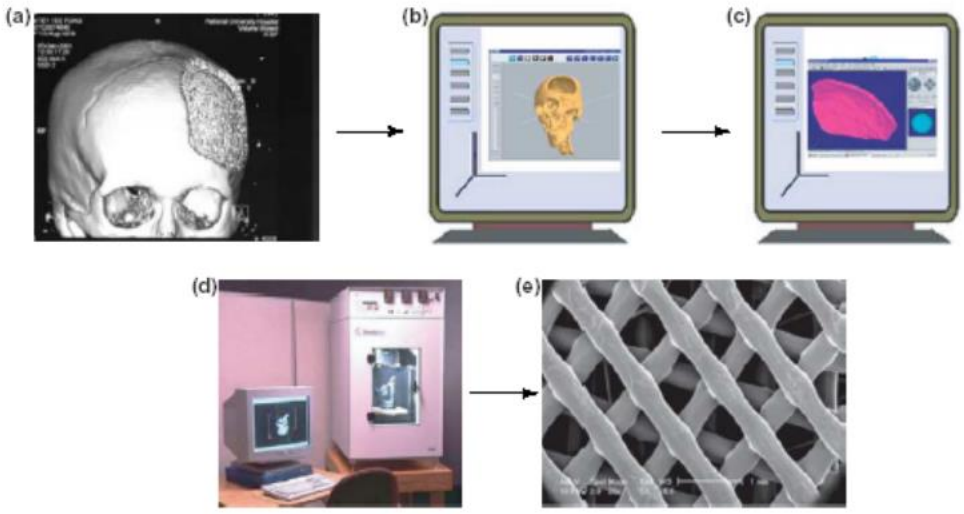

Figure 3. Steps required for scaffold manufacturing with RP technique that use CAD file. **a)** μ-CT scan data of the patient's defect is used to generated a CAD model. **b)** This is imported into RP system software to be "sliced" into thin layers. **c)** The "sliced" data are used to instruct the RP machine **d)** to build a scaffold **e)** layer-by-layer deposition. [36].

Another approach to scaffold creation is based on the use of hierarchal structures created by repeating a cell unit of known properties and geometry. However, this approach creates simple architectures with orthogonal and/or parallel channels, which do not really replicate the morphology of natural bone [38].
To overcome this limitation and at the same time create marketable shelves, CAD files from μ-CT of commercial polymer sponge or other porous devices (e.g. wood) can be used that can better imitate the trabecular structure of bone. Synthetic Scaffolds inspired by natural structures are having a lot of success because they allow to obtain a much more biomimetic result. For example, the microstructure of cuttlefish bone has inspired the manufacture of BTE shelves because its natural architecture is characterized by high porosity and at the same time high compressive strength [39].
In general, once the image is obtained, it is converted into DICOM (Digital Imaging and Communication Medicine) files and subjected to a segmentation process (a key step because the accuracy of the final model will depend on this) [17].
Then moving on to the reconstruction of the 3D volume that will be used to create the 3D CAD model for the scaffold construction, after which the CAD model is converted into an STL file, the surface of the object is discretized using a polygonal mesh and cut into individual layers [40].
After checking and correcting possible errors in the STL file due to file conversion, all the individual parameters for 3D printing are selected and set. These will vary depending on the type of technology adopted and the material chosen [17].
The setting of the layer thickness is a parameter common to all RP systems; it will determine the resolution of the object [17].
Some techniques, such as Robocasting, does not use the CAD file as a starting point, but text script.
Robocasting is another AM techniques in which a grid-like scaffold is built using micron-sized ceramic powder and fine nozzle. This technique allows the continuous extrusion of a thin filament (until 30μm) from a nozzle onto a building platform [41].
Over the last two decades more than 20 different RP techniques have been used and marketed for TE [33],[36].
With regard to BTE, today 3D scaffolds with controlled cell distribution and biocompatible materials, optimal for the repair of bone defects, are produced [6].
RP can be divided into three large families (Figure 4):

1) **Laser-based methods:** use a beam of light, such as digital light processing (DLP), and laser-based systems [9], to fabricate cross-linked TE scaffolds [33] .
   A typical set-up is usually composed of beam delivery optics, light source and the specific material [42].
   The presence of a photoinitiator is required and must be added in small amounts to avoid toxicity [6].
   The principal disadvantage of these methods is a lower cellular viability compared to other methods [43].

2) **Nozzle - based methods:** the material in the form of a filament is extruded by a robot-controlled nozzle [9] by applying controlled pressure [6].
   These methods create continuous and thin streams of material that are directed by CAD software connected to the machine.

Depending on the material chosen, these methods can allow us to incorporate a large number of cells into the bioink. They are subject to low shear stress, which in turn has a positive effect on their capacity for diffusion and proliferation [6];

3) **Printer methods:** are based on a head that prints a liquid binder onto slim layer of powder, following the design that is generated by software [33].

In fact, unlike nozzle-based methods, the biomaterial can be extruded as droplets and not continuously [6].

These methods use a non-contact technique that may use piezoelectric, thermal or electromagnetic forces to expel drops of material onto a building platform, replicating a CAD design [43].

Printer-based methods are generally inexpensive and easily applicable to low-viscosity materials [6]. Based on several experiments, it can be stated that such procedures have good potential for BTE [6].

However, due to frequent nozzle clogging, regular printing is difficult to achieve [6].

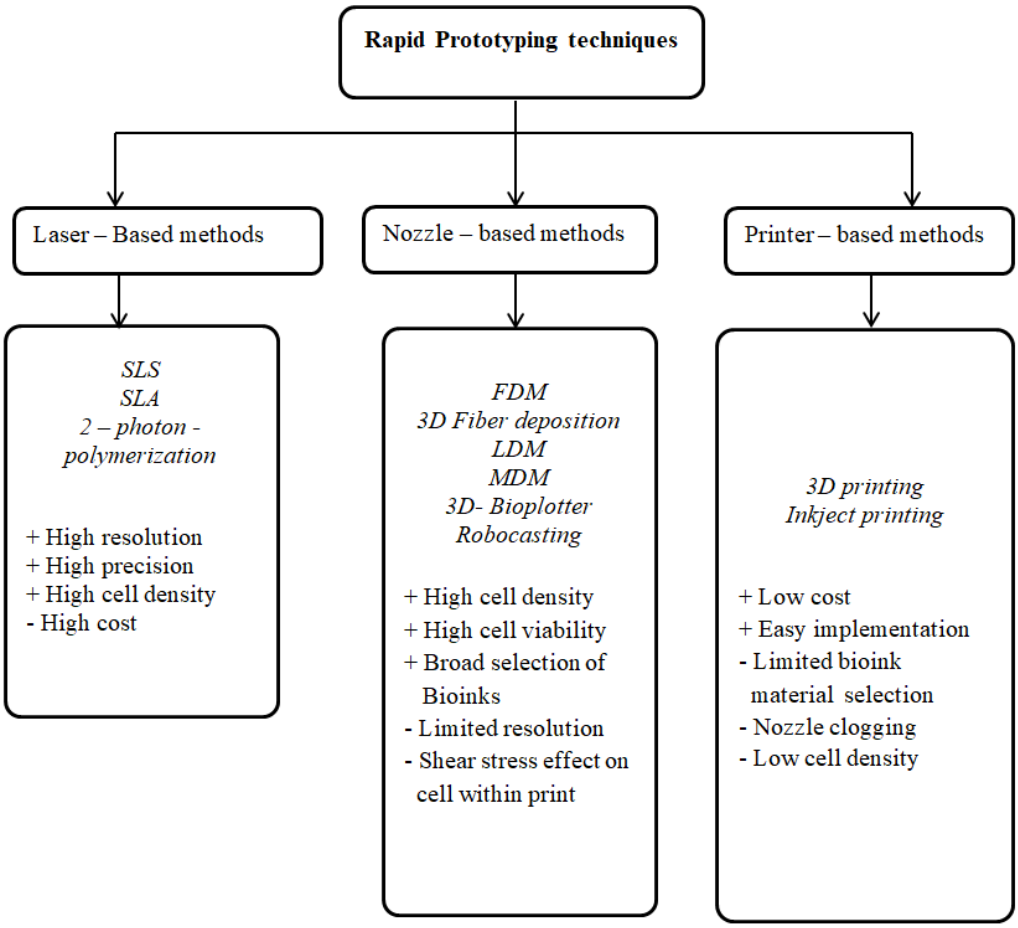

Select Laser Sintering, (SLS),Stereolithography (SLA), Fused Deposition Modeling (FDM), Low Temperature Deposition Manufacturing (LDM), Multi – nozzle deposition manufacturing (MDM)

Figure 4. Rapid Prototyping techniques and their advantages (+) and disadvantages (-), adapted from [33].

Resolution is often the discriminating factor determining the choice of a specific technology rather than another one. Each method has a precise lower limit on the amount of detail it is capable of reproducing [33].
Table 3 provides a comprehensive picture of the RP techniques commonly used in the realization of BTE scaffold.

Table 3. Comparison of different RP technologies in BTE, adapted from [1], [4], [34], [9].

Technique	Process details	Resolution (µm)	Material for BTE	Advantages	Disadvantages
SLS	Preparing the powder bed Layer – by – Layer addition of powder Sintering each layer	500	Ceramics (HA β-TCP) Polymers (PLLA PCL) Metals	No need for support No – post processing	Feature resolution depends on laser beam diameter Low surface quality Low mechanical strength
SLA	Immersion of platform in photopolymer liquid Exposure to focused light according to the desired design Layer – by –layer fabrication	30	Ceramics (HA β-TCP, Bioactive glass) Polymers (PDLLA PPF)	Complex internal features can be obtained Grow factors, proteins and cell patterning is possible	Only applicable for photopolymers High production cost Slow process
FDM	Strands of heated polymer/ceramics extrusion through a nozzle	250	Ceramics (HA TCP, Al_2O_3) Thermoplastic polymers	No need for platform/ support Low production costs	Low surface quality Low resolution Low mech. Properties
3D printing	Strands of viscous material (in solution form) extrusion based on the predesigned structure Layer – by – layer deposition strands according to the tear of speed	100- 200	Ceramics (HA Bioactive glass) Polymers (PLA PEG PLGA)	Mild condition of the process allows drug and biomolecules plotting No support material is required	Low mechanical strength Low accuracy compared to SLA Low surface quality (rough surface)
Robocasting	Direct writing of liquid using a small nozzle while a nozzle is moved across a platform.Consolidation through liquid – to gel transition Layer – by – layer fabrication.	100-1000	HA/PLA HA/PCL 6P53B glass/PCL	Independent 3D nozzle movement Precise control on thickness No need for platform /support	Material restriction Low accuracy compared to SLA

3D Fiber Deposition	The material is in a granule or pellet form. Material flow is regulated by applying pressure to the syringe	250	Polymers (PEGT)	Quick process	High temperature is required
LDM	The scaffold – building cycle is performed in a low – temperature environment under 0°C	300 - 500	Polymers (PLLA)	Can incorporate biomolecule	Solvent is used Requires freeze drying
MDM	It is similar to LDM But in this case a greater range of materials can be used	400	Polymers (PLLA)	Enhanced range of materials can be used Can incorporate biomolecule	Solvent is used Requires freeze drying
3D Bioplotter	The nozzle system works pneumatically or via volume – driven injection. Key difference with other nozzle – based systems is the ability to plot into a liquid medium with matching density	45- 1600	Hydrogel Polymers (PCL PLLA)	Enhanced range of materials can be used Can incorporate biomolecule	Low mechanical strength Low accuracy Slow processing

2.3.1 Rapid Prototyping techniques for the production of bio-ceramic scaffolds

With RP techniques, several types of biomaterial are used to fabricate bone-like scaffolds, like natural and synthetic polymers, ceramics [13], glass and even glass and even cells (bioinks) [9]. Among the techniques included in Table 3., the most suitable for the production of ceramic scaffolds are FDM, SLS, 3DP, Robocasting and SLA, as descripted in Figure 5.

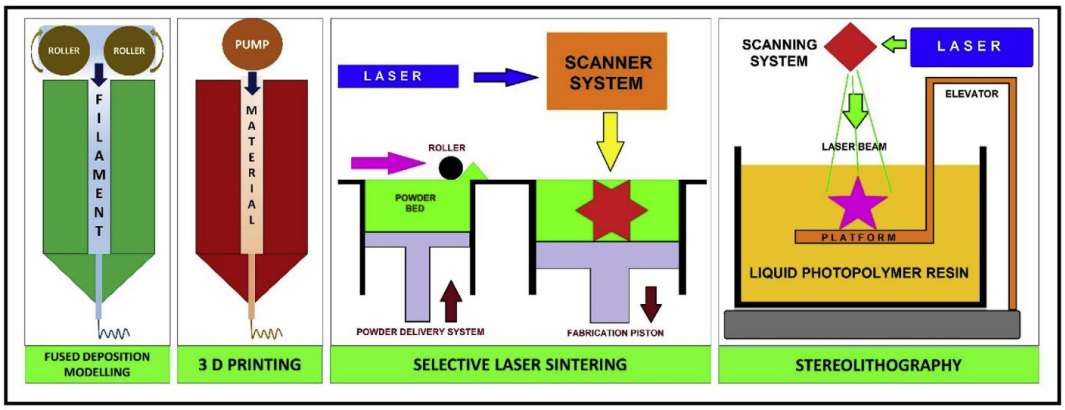

Figure 5. Schematic presentation of principal techniques used to produce ceramic scaffolds in BTE [7].

Moreover, it is possible to divide RP for the processing of bio-ceramic materials into two categories:

1) **Direct fabrication techniques:**

   These techniques allow the production of sintered ceramic parts without the need for a subsequent thermal post-processing. These techniques melt the ceramic powder using a high-energy laser [32].
   However, rough surfaces are often obtained and local thermal stress issues may arise. SLS technique or EBM (electron beam melting) are examples of direct techniques [32].

2) **Indirect fabrication techniques:**

   These techniques are based on three fundamental steps: 3D printing, thermal de-binding, and sintering [32].
   With these techniques, the printing process does not lead to a finished product but rather to the so-called "green body", which contains, in addition to the ceramic powder, a volatile organic matrix [40], [44].
   Post-processing is then necessary to obtain the finished object with satisfactory mechanical properties and a higher relative density [44]. As a result, de-binding and sintering are crucial steps for defining the final properties of the scaffold. Debinding process leads to the thermal decomposition of the binder and then, with the sintering process, a final compact part, free of organic material is obtained [44].
   Techniques such as FDM, SLA or 3D printing are part of this family [32].

The accurate internal architecture of the scaffold guaranteed by RP techniques and the choice to use ceramic materials, in particular CaPs, if properly designed can ensures to obtain structures that can be used to BTE applications. These kind of scaffolds will able to trigger the osteogenic process [6], facilitate the interactions of growth factors and osteogenic cells and the differentiation of mesenchymal cells (MSCs) into the osteogenic lineage [6].

CaPs scaffolds have also shown a great potential as drug carriers, as they have high-performance drug release and promote osteoblast proliferation activity [6].
Animal studies have shown that CaPs scaffolds loaded with vascular endothelial growth factor (VGEF) and BMP - 2 are useful in speeding up bone regeneration [6].
However, one of the most critical aspects concerning CaPs scaffolds is related to the intrinsic fragility of ceramic materials [9]; therefore, it is always necessary to adjust the design of the 3D scaffold in order to balance porosity requirements and mechanical properties [15].
Especially for brittle materials such as ceramics, once the printing process is finished, it is essential to control the mechanical response, stress-strain and compression test and breakage resistance of the scaffold as a function of time [15].
Another issue of major concern is the adequate control on the degradation kinetics of the scaffolds [6], in particular, dealing with HA, this could be troubling due to the very slow degradation rate of the material in contact with body fluids [7].
According to literature studies, among the available AM technology, SLA is one of the most promising for the processing of BTE scaffolds thanks to the high resolution achievable, the possibility to use different kind of ceramic materials [9]. Thanks to the emergence of microstereolithography (MSTL) and Digital Light Process (DLP), the accuracy of the samples is even better; so it is possible to create more complex structures. Besides having a high resolution [13], it can process clinically used methacrylate - base light curing composites without modifications [32].

2.4 Stereolithography (SLA)

Among the various RP techniques that can be used with ceramic materials, Stereolithography (SLA) ensures maximum control in creating structures with a detailed and precise internal geometry and a high surface finish [1].
Developed by Chuck Hull, the "father of 3D printing", in 1986, SLA w one of the first techniques to appear on the market [1].
Since that moment, SLA has been widely used in BTE for the creation of HA, β-TCP, Zirconia, Alumina, and bioactive glass scaffolds [1].

2.4.1 Processing

SLA is an additive manufacturing process using a bath of liquid UV - curable photosensitive liquid system, an ultraviolet (UV) laser to build 3D structures layer - by – layer, a movable platform and a dynamic mirror system [1], [33].
When the printing process begins, the laser beam solidifies the ceramics material at the surface of the bath, thus creating the first layer; the irradiated zones are defined in accordance with the previously determined scaffold CAD model [45],[36]. When the irradiation of a layer ends, depending on the configuration of the machine (top-down or bottom-up system, see Figure 6), the slurry bed is respectively raised or lowered by an elevator platform.

Most SLAs use the bottom-up system; in this case the platform moves down so that the new material can cover the newly formed layer. The laser cures a new layer over the previous one [1].
In the second system the platform moves upwards and the vat must be completely transparent [9].
This second approach has a few more advantages compared to the bottom-up system, first of all the demand for a smaller amount of raw material [9].

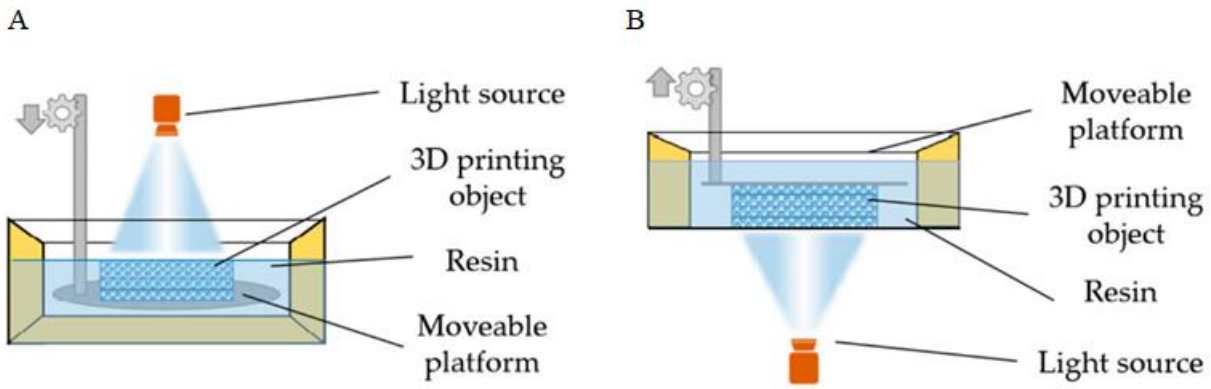

Figure 6. Stereolithography with A) bottom-up system; B) top-down system [46].

The displacement along the z axis and the irradiation depth actually determine the thickness of each single layer, and thus the surface resolution of the final object [1].
Exposure to the UV laser light solidifies the pattern traced on the slurry and allows it to adhere to the layer below [33].
The subsequent deposition of adjacent layers leads to the building of the 3D object characterized by highly-resolved solid structure [47].

2.4.2 The slurry: composition and characteristics

The ceramic slurry should maintain long-term stability and have a proper rheological behaviour to achieve a smooth printing flow [1].
Most of the slurries used are non-aqueous, because aqueous suspensions usually give rise to weak structures; it is therefore preferable to use acrylamide resin-based slurries [1].
From a rheological point of view, slurries should exhibit Newtonian flow behaviour [48] and viscosity values should be low enough to facilitate the printing process and to avoid the formation of air bubbles [49].
Slurry viscosity is strictly dependent on the number of ceramic particles.
In order to obtain high quality products, the percentage of ceramic powder in green bodies must be at least 50% [49]; as the particle content increases, a shrinkage decrease upon sintering has been reported, thus significantly improving the quality of the final product [40].
However, if the dust content is too high, viscosity could increase over the optimal value established for the processing of ceramic materials (3 Pa·s) [49]. Moreover, particles must be homogeneously dispersed within the organic liquid matrix and their size should be smaller than the layer height [1].

It is possible to reduce the slurry viscosity by incorporating non-reactive thinners (e.g. N-methylpyrolidone) or by increasing the manufacturing temperature [40].
Moreover, the addition of some dispersant agents could be beneficial to the slurry quality, ensuring low viscosity values and good homogeneity while keeping the solid loading high [50]. In particular, long-chained fatty acids, phosphine oxides or oligomeric surfactants can reduce particle agglomeration, decreasing viscosity and improving slurry stability and density [40].
Transparency to UV light is another fundamental requirement in order to achieve the desired light penetration depth. In fact, if the slurry is not transparent enough, light penetration will be attenuated, resulting in a considerable cure depth decrease.
If required, absorbant agents for visible light or UV rays could be added in order to limit the cure depth, thus avoiding an excessive polymerisation along the z axis [40].

2.4.2.1 The photopolymerization process: chemical basis

When the ceramic powder, monomer, and photoinitiator are illuminated by the UV light, the photoinitiator generates cation species or free radicals , attacking the double bonds of the monomer, and triggering polymerisation [49].
The subsequent reactions between the monomer and the active end of the chain allow the polymeric chains to increase their length until a termination reaction occurs [49].
Two different types of photopolymerisation can occur: cationic polymerisation or radical polymerization. The latter is generally preferred in SLA processes because it is easier to control [49].
During radical polymerization, the PI divides and generates radical species. These radicals are highly reactive and immediately attack the double bonds of the monomer [49].
The main steps of radical polymerisation are given below [49]:

Initiation $PI \xrightarrow{h\nu} R\cdot$ *(1)*

Propagation $R\cdot + M \longrightarrow R(M)_n\cdot$ *(2)*

Termination $R(M)_n\cdot + R(M)_m\cdot \longrightarrow R(M)_{m+n}\cdot R$ *(3)*
$R(M)_n\cdot \longrightarrow R(M)_n$

M= Monomer, R= Radical, PI= photoiniziator

For radical photopolymerisation, acrylate functionalised monomers (i.e. cured acrylated epoxy, acrylated polyester and acrylated urethane) and telechelic oligomers are usually used due to the rapid rate of their polymerisation [49].
Acrylates are often combined with methacrylates to decrease shrinkage during curing.
Another method to reduce shrinkage and speed up curing may be a combination of acrylate and epoxy-based resins [40].
The photopolymer acts as binder between the ceramic powder, making it possible to accurately manufacture the part [44].

The kinetic of reaction and the mechanical properties of the final structure are significantly affected by the quantity of PI and their choice has to be based on the nature of the monomers used. It has been reported that, as the PI concentration increases, the polymerisation speed and the stiffness of the sample increase [40].
However, the quantity of PI must be limited as their intrinsic cytotoxicity could be harmful for tissue ingrowth and regeneration; for example, PIs for cationic polymerisation form strong proton acids and it is therefore preferable not to use them for biomedical applications. For this reason, radical PIs are usually preferred, even though serious DNA damages could occur if not properly dosed [40]. A commonly used low toxicity PI is Irgacure 2959 [40].

2.4.2.2 Key Parameters for Photopolymerization Process

Some important parameters need to be set and controlled in order to obtain a good light-curing slurry for printing:

Energy of the Laser UV:
The energy E (J/cm^2) [49] of the UV source can be calculated as the product between the intensity of the UV light beam and the exposition time [51].
The incident energy dose must be adjusted in order to achieve the correct depth of cure, coinciding with the desired layer thickness [51].
For a single mode laser beam, the intensity follows a gaussian distribution [51]. A Gaussian beam of peak intensity I_{max} and width w^2_{Gauss} has an actual distribution of intensity at the surface (z = 0) which varies in the width direction (y) as equation *(4)*:

$$I_0(y, z = 0) = Imax\ exp(\frac{-2y^2}{w^2 Gauss}) \quad (4)$$

where z is the depth from the surface of the suspension, y is the distance from the center of the bean.

The incident energy dose (E_0) is the illumination time multiplied by intensity (E=I·t) *(5)*:

$$E_0(y,z=0) = I_{max}\ exp\left(\frac{-2y^2}{w^2 Gauss}\right) \quad (5)$$

At any point, the incident energy dose (E_0) can be estimated by Beer - Lambert's law , which states that the energy dose attenuates logarithmically with depth (z), according to equation *(6)* [51]:

$$E(z) = E_0\ exp\left(\frac{-z}{Sd}\right) \quad (6)$$

where E_0 is the dose of incident energy on the surface and S_d is the resin sensitivity in the depth direction.

The energy dose could be estimated by equation *(7)*:

$$E(z) = E_{max}\, exp\left(\frac{-2y^2}{w^2 Gauss}\right) exp\left(\frac{-z}{Sd}\right) \quad (7)$$

where E_{max} is the maximum dose of energy

The polymerisation of the slurry will take place at every point in which the energy dose is greater than or equal to the critical energy dose necessary for polymerisation to take place (E_d) [51]: polymerisation in the cross-section must then take place at points (y*, z*) where E(y*, z*) = E_d.
We will thus obtain a parabolic curve shape given by *(9)* [51]:

$$ln\left(\frac{Emax}{Ed}\right) = \frac{2y^{*2}}{w^2 Gauss} + \frac{z^*}{Sd} \quad (9)$$

Penetration Depth (D_p):
The penetration depth of the laser beam (D_p) is defined as the depth where intensity is reduced by 1/e of the beam intensity measured at the bath surface [45], [47].
D_p depends on the size and quantity of the ceramic particles [49] and the difference in refractive index between the UV curable solution and the ceramic powder [52].
Once E_d and D_p are determined, it is possible to properly choose the laser beam power and the scanning speed [53].
A good slurry for SLA is usually characterized by high D_p values, to minimise the layer thickness and low E_d, so that the polymerization reaction can be initiated with a low energy dose [54].

Cure width (C_w)
Cure width (C_w) is defined as the width of E_d, E_{max} and laser beam width [51].
The curing width is always greater than the diameter of the laser beam, due to dispersion phenomena caused by the presence of ceramic particles [55].

Cure depth (C_d):
Cure depth (C_d) is defined as the maximum depth at which the material receives sufficient light to reach the gel point [49], forming a three-dimensional gel network during light-curing [47].
The gel point indicates the transition of the slurry from visco-plastic (pre-gel) to rigid-elastic (post-gel) behaviour [56].
C_d must be at least equal to the layer thickness [56] and the polymerization depth is too great, , a loss in spatial resolution could be observed.
C_d could be related to the parameters of Beer - Lambert's law, according to equation *(10)*:

$$C_d = S_d\, ln\left(\frac{E0}{Ed}\right) \quad (10)$$

It is essential to understand how the composition of the slurry influences the relationship between C_d and energy dose in order to obtain photopolymerizable slurries [56].
A compromise between these two parameters must be established so that products with both satisfactory spatial resolution and low manufacturing times could be obtained [51].

High C_d values require high energy density but guarantee an optimization of the working time ; on the contrary, a good resolution would, require low energy density [55].
It has been confirmed that, by varying the concentration of the ceramic powder, the particle size, and the refractive index, both C_d and C_w could be properly modified, according to the needs [51].
The curing rate increases as the ratio of the refractive index between ceramic particles and organic content decreases. The ceramic powder scatters light, thus decreasing the resolution, cure depth and increasing printing time [1].
Smaller particles generally have better light scattering properties [1].
Gentry and Halloron have shown that when the refractive index of the precursor monomer corresponds to the refractive index of the ceramic powder, there is an improvement in curing depth [49].
Light scattering effects lead to the polymerisation of an area larger than the predetermined area: this effect is called overgrowth [57].
C_d also depends on how much photoinitiator (PI) is used for slurry preparation: if the PI concentration is high, C_d decreases [47].

2.4.3 Post - Processing

Unlike SLS and other direct techniques, where the ceramic material is shaped and sintered in a single step, for SLA, once printing is concluded, a further step called post-processing is necessary. In fact, the so-called "green body" resulting from the printing process still requires additional thermal treatments to be transformed into a ceramic part [44], [57].
Besides the ceramic powder (~ 60%), the "green body" still contains a volatile organic matrix which must be eliminated [40], [44].
The –post-processing involves three fundamental steps: cleaning and drying of pieces from uncured slurry, de-binding and sintering. During de-binding, the binder is thermally decomposed: organic residuals slowly degrade, leaving behind only the loosely compacted ceramic powder [44].
During de-binding, the temperature increase must be slow and constant to avoid the formation of internal stresses which can result in the formations of cracks within the structure[44].
The debinding temperature and the time required depend on several factors, such as [58]:

- quantity of organic components,
- composition of organic components,
- size and distribution of ceramic particles,
- percentage of solid part contained in the slurry, compared to the organic matrix.

The removal of the binder is important in order to avoid contaminations that could change the properties of the final product [9].
The greens are then densified upon sinteringto form the final ceramic scaffold [44].
The –high-temperature sintering process is usually carried out between 50-75% of the melting temperature of the material [9]. Usually, the higher is the sintering temperature, the more resistant will be the scaffold

[7]. However, if the porosity of the sintered scaffold remains too high, the mechanical properties may be affected significantly anyway [9].
During sintering, the scaffold inevitably undergoes volumetric shrinkage, [9], that must be carefully considered and preferably estimated before printing, during the design phase [32].
The main steps of the post - processing are shown in Figure 7.

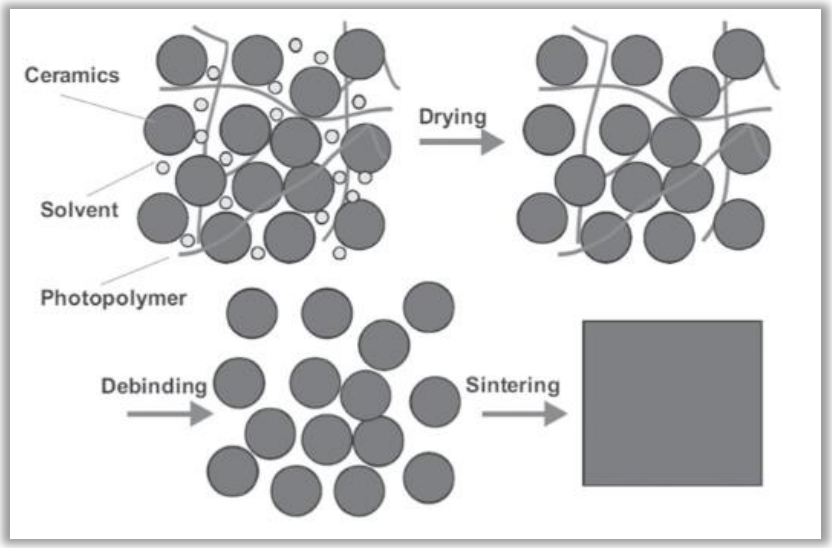

Figure 7. Principal steps of post-processing from the ceramic green body to the sintered dense ceramic [44].

To minimize shrinkage and increase shape accuracy, the slurry should have a high ceramic particle content; however, this can cause the formation of cracks due to gases which are unable to reach the surface of the scaffold, creating a strong internal pressure [1].
To facilitate the sintering process, external pressure can be applied; in this case the sintering is called "sintering under pressure". On the contrary, if no external pressure is applied, the sintering is called "sintering without pressure" (or conventional sintering) [9].

2.4.4 SLA: Advantages and Disadvantages

Some more advanced variants, such as μ-Stereolithography (μ-SLA) and two-photon polymerization (TPP), allow an even better quality resolution compared to conventional SLA [9].
With μ-SLA, the thickness of a layer can be decreased up to 10 μm [9], whereas TPP is even capable of achieving a resolution of less than 0.1 μm [40].
Resolution of a standard SLA layer depends on the elevator layer resolution (up to 1.3 mm) and laser spot size (80-250 mm) [36].
Products made with SLA are usually robust and can be used as master patterns for thermoforming, selection moulding, as well as in various metal casting processes [33].
However, this process often has high processing costs: the photo-curable resin can cost from $300 to $800 and a stereolithography machine can cost from $100.000 to more than $500.000 [33].
If the product is very large, point-by-point polymerization of the cross-section of each layer can be very time consuming, making the process computationally long and demanding [40].

The main parameters that influence the success of SLA printing are: [1]

- type and concentration of monomer,
- volume ratio between ceramic powder and organic components,
- chemical interaction between ceramic powder and organic components,
- viscosity of the slurry,
- laser beam power,
- optimisation of debinding and sintering steps
- time of exposure to light.

2.5 Digital Light Processing (DLP)-Based Stereolithography

Recently, a new method based on the stereolithographic technique has been proposed, which allows a considerable reduction in production time.
Digital light processing (DLP) based stereolithography (SLA) is an innovative and very efficient RP technology particularly appreciated for the production of CaPs scaffold for BTE. Besides its speed, DLP guarantees an excellent resolution of the final product [59] and reduces the stress to which samples are subjected during processing [60].
In the present thesis project DLP was used for the realization of scaffolds with trabecular-like porous structure. .
The term DLP refers to digital mirror devices that, when properly controlled, selectively expose the photosensitive resin to visible or ultraviolet (UV) light [61].
The manufacturing process is similar to the classical SLA: the DLP builds complex 3D layer-by-layer structures. The geometry of the various layers is previously determined by cutting the design CAD model on a series of horizontal planes at close range [45]; the operator is also able to set all printing parameters according to the slurry curing characteristics [57].
The big difference compared to classical SLA is the use of a series of computer-programmable arrays of digital micro-mirror devices (DMD) [45], which allow the simultaneous irradiation of the entire desired cross-section [40], [59].

2.5.1 System setup

The main components of the DLP system are Digital Micro Mirror Devices (DMD), a projection lens, a vat containing UV curable resin, a UV light source, and a motorised translation stage.
The setup can be implemented in two different ways: a free-surface approach or top-down projection (Figure 8.A)) and a constrained surface approach or bottom-up projection (Figure 7.B)) [40],[62].
In a free-surface approach the light exposure is from above and the building platform is immersed in a slurry bath. After the polymerisation of a layer, the z-phase is lowered into the resin tank and the new material successively coats the growing part [45].

Utilising a constrained surface approach, the slurry is illuminated from below through a transparent vat. After the polymerisation of each layer, the building platform is raised by a distance equal to the thickness of the individual layer. In this way, the liquid slurry can flow into the cavity and the next layer is created [62].

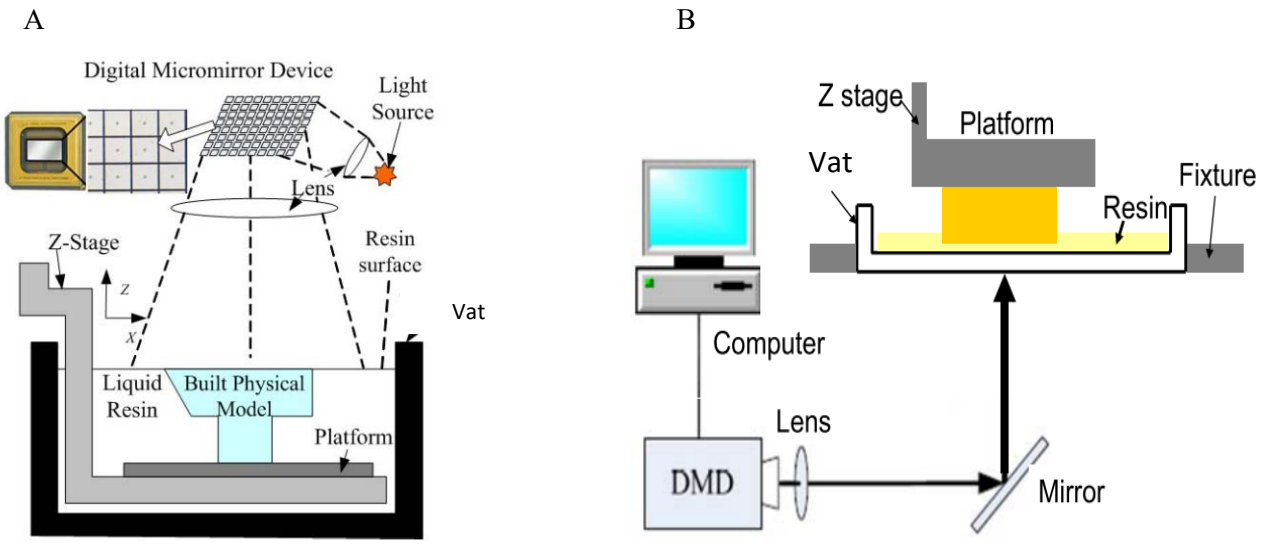

Figure 8. A) DLP setup free surface approach (TOP DOWN) and B) constrained surface approach (BOTTOM UP) [62].

A constrained surface approach is often preferred as it guarantees certain advantages over the other method. These advantages include [62]:

- Increased motion accuracy of the z - stage down to precisions of 0.1 - 1µm which ensures a smooth surface and precise layer thickness [40];
- New liquid slurry can be added as needed through a pump [62], so fresh material supply is always guaranteed, even for large jobs;
- The layer created is not directly exposed to air, allowing faster light-curing [62],
- The structure under construction is not completely submerged in the vat; this considerably reduces the amount of material required and, consequently, the cost of production [40].

It is important for the newly created layer not to remain attached to the surface of the vat, but to properly adhere to the previous layer, and for the whole structure to remain firmly attached to the building platform throughout the process. To promote the attraction forces between scaffold and building platform and reduce the attraction forces between scaffold and vat surface, the vat is coated with hydrophobic films, such as polytetrafluoroethylene (PTFE), silicon or polydimethylsiloxane (PDMS) [62].
Furthermore, it is necessary to pay attention to any curved surfaces during printing: the DLP process is particularly suitable for illuminating geometries with 90° angles and runs the risk of creating saw - tooth roughness when illuminating curved structures [40].

2.5.2 Digital Micromirror Device (DMD)

Digital micro-mirror devices (DMD) are the key component of the DLP process.
A microelectromechanical system (MEMS) acts as a dynamic mask when connected to the computer [40].
The chip was developed at Texas Instruments in 1987 and consists of an array of reflective aluminium micro - mirrors [45].
Each mirror is fixed on top of a yoke and hinge system on a silicon memory cell, creating a single pixel [40].
If a sufficiently high polarization voltage is applied, the electrostatic attractions bring the mirrors into an unbalanced position of < 10° or > 10° with respect to the position of equilibrium [63].
The address voltage determines in which direction the mirror is tilted [40].
If the micro - mirror is in the condition of < 10° ("tilt on" or ON), the light from the light source is reflected in the projection lens [63] and the image [40]. is created. When it is in the condition of > 10° ("tilt off" or OFF), the light is not reflected but is collected by a light absorber [63].
Generally, a DMD chip contains more than 442.000 switchable mirrors [63].

The use of the DMD provides many advantages:

- The large number of micro-mirrors allow a better and more uniform intensity of the light [45]; moreover the pixels, being reduced in size, allow a higher resolution of the display [45].
- Ultra - flat aluminium micro-mirrors permit successful modulation of the UV illumination [45].
- There is greater control over exposure time: this is particularly important so that the modulation of the grayscale intensity can occur at pixel level [45].

2.5.3 Advantages and Disadvantages of DLP Process

In summary, the main advantages of the DLP process compared to other RP techniques are:

- The use of dynamic masks, which allow the polymerisation of an entire cross-section at once, drastically reducing production time regardless of the shape, size and complexity of the structure to be recreated [61]. The speed of the process is not only an economic advantage but is a fundamental requirement when working with partially stable resins that necessarily require fast processing times [40],
- High spatial resolution thanks to the small size of the pixels and the large number of pixels [50],
- No special environmental conditions required during processing [61],
- By using the constrained surface approach, the amount of material required is much smaller and this contributes to lower production costs [61],

There are also some negative aspects about this technique:

- Undesirable diffusion of light through the previously formed layers could cause uncontrolled polymerization and occlusion of the pore [64],
- If the curing depth of the UV light is not properly controlled, there may be a loss of resolution [64].

2.5.4 Current applications of SLA-based and DLP-based ceramic scaffolds

In recent years the SLA and DLP process have established themselves as successful techniques for the manufacture of ceramic scaffolds, thanks to the possibility of producing dense, precise and high-strength ceramics [65].
These techniques allow greater flexibility in the realization and modification of designs; samples can be quickly tested and readjusted and parts with precise characteristics can be created [65]. These peculiarities have allowed to obtain good results in BTE but also in dentistry and cranio-maxillofacial procedures [65].
Additive printing based on SLA and ofhigh resolution DLP allows to obtain ceramic pieces with theoretical densities higher than 99.8%, good mechanical properties, a homogeneous, precise and highly reproducible microstructure [65].
A wide range of ceramic materials can be used, such as zirconia (ZrO2), aluminia (Al2O3), TCP and HA [65].
In 2012 Ronca et al. developed a composite shelf using SLA and using nano-HA and poly-DL-lactide. Due to the presence of HA the scaffold has a higher structural strength and better biocompatibility [37].
In 2013, Brie et al, created scaffolds of HA only and implanted them in the skull of 8 patients. After a 12-month check-up these scaffolds did not cause any complications and a perfect continuity between host tissue and implant was recorded [37].
In 2019 Mangano et al.,. showed that biphasic calcium phosphate scaffolds made with SLA had better characteristics than scaffolds made with traditional sintering. Porous cylindrical scaffolds were composed of 30% of HA and 70% β-TCP in order to find the right balance for bone regeneration favored by the rapid resorption of β-TCP and low resorption of HA [66]. The scaffolds obtained with SLA were better able to mimic the porous trabecular organization of the maxillary bone characterized by a high interconnectivity of the spinal cord spaces.
SLA-molded specimens had a higher final strength with a smaller plastic region. An average compression of about 6.4 MPa and a compression deformation ε of about 3.6% was recorded to achieve material fracture [66].
HA's cylindrical shells were constructed with DLP-based AM machine by P.Tesavibul et al. Again, the samples have a geometry comparable to that of the original CAD model (11.3 mm diameter and 3 mm thickness cylinders). The samples have a density at 91% of the theoretical HA density and a compressive strength of cellular structure equal to 0.36 MPa. The average pore size is between 500-700 μm. Good results were obtained for the in vitro biocompatibility tests: after 14 days, preosteoblastic MC3T3-E1 cells sown on the scaffold began to proliferate and differentiate [67].

Several studies for the realization of scaffolds with bioreabsorbable materials were made by Lithoz using their CeraFab DLP process system.
In 2019, β-TCP-based BTE shelves were printed in different geometries (hexagonal Kagome, rectilinear Grid, Schwarz primitive, and hollow Schwarz architecture) to evaluate the best compromise between porosity and mechanical properties [59]. The recilinerar Grid structure showed a compressive strength of 44.7 MPa (Weibull modulus is 5.28) at 50 vol% porosity. In addition, a short-term study showed the growth of preosteoblastic MC3T3-E1 cells [59].
Despite the good results that are being obtained, in order to create scaffolds with characteristics suitable for use in BTE, pore microstructure defects, rheological properties of the slurry, correct sintering temperature and satisfactory mechanical properties are still rather problematic aspects that need to be improved [68]. In any case, the various studies show that it is almost always possible to obtain high relative density percentages of the scaffold and excellent cell biocompatibility results. The main property that should be improved is the compressive strength of the sample, often too low for the requirements of BTE. For example, 45S5 Bioglass® scaffolds made by the DLP process have a lower compressive strength than porous scaffolds made by the foam replica method [69].
In Table 4 you can find some studies found in the literature and the main characteristics of scaffolds printed with classic SLA or DLP technique.

Table 4. Applications of bioceramic scaffolds in BTE with SLA/DLP process

Reference	Material	Scaffold geometry	Technique	Scaffold property
C.Mangano et al., 2019 [66]	Biphasic CaPs (70% β-TCP/ 30% HA)	Porous cylinders	SLA	- Pore size: 100 µm - Compressive strength: 6.4 MPa - Biocompatible (cell-culturing with MC3T3-E1 pre-osteoblasts)
P.Tesavibul et al., 2014 [67]	HA	Porous cylinder	DLP	- Relative Density: 91% - Pore size: 500-700 µm - Biocompatible (cell-culturing with MC3T3-E1 pre-osteoblasts)
C. Schimidleithner et al., 2019 [59]	TCP	Grid structure	DLP	- Relative Density: 99.5% - Pore size: 400 µm - Porosity: 50 vol% - Compressive strength:44.7 MPa and Weibull modulus: .28 - Biocompatible (cell-culturing with MC3T3-E1 pre-osteoblasts)
Y.Yao et al., 2019 [68]	HA	Cubic structure (10x10 mm)	DLP	- Relative Density: 95.85% - Shear viscosity < 3.7 Pa·s
C.Ghayor et al., 2018 [70]	TCP	15 scaffolds with different defined pore/bottleneck dimensions and distributions	DLP	- Pore size for osteoconductive property: 700-1200 µm
Y. Zeng et al., 2018 [60]	HA	Square pore structure (21x21x3 mm)	DLP	- Compressive strength (z direction): 11.8 MPa - Compressive strength (x direction): 5.1 MPa - Biocompatible (cell-culturing with MC3T3-E1 pre-osteoblasts)
P.Tesavibul et al., 2012 [69]	45S5 Bioglass®	Cylindrical cellular structure (d=9.8 mm; h=11.6 mm)	DLP	- Pore size: 500 µm - Compressive strength of the cellular structure: 0.33 MPa
Z.Liu et al., 2019 [71]	HA	Porous rectangular scaffold (l= 10 mm; h=20 mm)	DLP	- Pore size: 300-600 µm - Relative Density: 94.9% - Porosity: 49.8% - Bending strength: 41.3 MPa - Compressive strength: 15.25 MPa - Biocompatible (cell-culturing with MC3T3-E1 pre-osteoblasts)
C. Feng et al., [72]	HA (45% vol)	Porous cylindrical scaffold (d=11.8; h=14.2)	DLP	- Relative density: 66.6% - Flexural strength: 10.0 MPa - Compression strength: 12.0 MPa
Y. Cao et al., 2020 [73]	ZrO_2 / HA	Porous rectangular scaffold (l=7.5 mm; h=15 mm)	DLP	- Compressive strength (HA 10 wt%): 52.25 MPa - Biocompatible (cell-culturing with MC3T3-E1 pre-osteoblasts)

Conclusion

In order to overcome the intrinsic limits of natural grafts, during the last decades, BTE focused on synthetic grafts in CaPs with a preference for those in HA or TCP. Synthetic grafts, more commonly known as 3D scaffolds, must provide the same function as ECM, thus ensuring cellular activity, adequate mechanical support and the production of precise cells and proteins through mechanical and biochemical interactions.

To perform these tasks the scaffold must be carefully designed, in fact it will not be sufficient to choose a biocompatible material able to promote osteogenesis, to ensure a good result; but it must have a certain degree of porosity, a precise pore size and adequate surface characteristics.

Over the years many techniques have been improved and developed, but only with "non-conventional techniques" (or RP techniques) it has been possible to obtain scaffolds with a highly reproducible and precise structure.

These methods, by CAD files, are able to made 3D porous scaffolds with precise structural properties.

Among the various RP techniques presented, SLA is very suitable to be used with ceramic materials, ensuring a very high resolution and ease of processing.

Today this technique has been further improved, by replacing UV laser with a new lighting method that is able to reduce processing time without affecting the spatial resolution. This method is called DLP process and is based on a DMD consisting of millions of mirrors, which is able to scan an entire layer at a time.

By combining the properties CaPs, listed in Chapter 1 with this promising new AM technique, it will be possible to create accurate scaffolds that can be used to manage large and small bone defects even in load-bearing anatomical sites.

References

[1] K. Lin, R. Sheikh, S. Romanazzo, and I. Roohani, “3D printing of bioceramic scaffolds-barriers to the clinical translation: From promise to reality, and future perspectives,” Materials (Basel)., vol. 12, no. 7, pp. 1–20, 2019.

[2] L. C. Gerhardt and A. R. Boccaccini, “Bioactive glass and glass-ceramic scaffolds for bone tissue engineering,” Materials (Basel)., vol. 3, no. 7, pp. 3867–3910, 2010.

[3] S. Dorozhkin, “Medical Application of Calcium Orthophosphate Bioceramics,” Bio, vol. 1, no. 1, pp. 1–51, 2011.

[4] W.-Y. Yeong et al., “Rapid prototyping in tissue engineering: challenges and potential,” Trends Biotechnol., vol. 22, no. 12, pp. 643–652, 2004.

[5] K. Rezwan, Q. Z. Chen, J. J. Blaker, and A. R. Boccaccini, “Biodegradable and bioactive porous polymer/inorganic composite scaffolds for bone tissue engineering,” Biomaterials, vol. 27, no. 18, pp. 3413–3431, 2006.

[6] L. Zhang, G. Yang, B. N. Johnson, and X. Jia, “Three-dimensional (3D) printed scaffold and material selection for bone repair,” Acta Biomater., vol. 84, pp. 16–33, 2019.

[7] S. Mondal and U. Pal, “3D hydroxyapatite scaffold for bone regeneration and local drug delivery applications,” J. Drug Deliv. Sci. Technol., vol. 53, pp. 1–11, 2019.

[8] H. E. Jazayeri et al., “The cross-disciplinary emergence of 3D printed bioceramic scaffolds in orthopedic bioengineering,” Ceram. Int., vol. 44, no. 1, pp. 1–9, 2018.

[9] F. Baino et al., “Processing methods for making porous bioactive glass-based scaffolds—A state-of-the-art review,” Int. J. Appl. Ceram. Technol., vol. 16, no. 5, pp. 1762–1796, 2019.

[10] ASTM InternationalStandard Guide for Characterization of Ceramic and Mineral Based Scaffolds used for Tissue-Engineered Medical Products (TEMPs) and as Device for Surgical Implant Applications and ASTM Standard F2883 - 11, “Standard Guide for Characterization of Ceramic and Mineral Based Scaffolds used for Tissue-Engineered Medical Products (TEMPs) and as Device for Surgical Implant Applications,” ASTM B. Stand., no. January 2012, pp. 1–7, 2011.

[11] C. M. Murphy, F. J. O’Brien, D. G. Little, and A. Schindeler, “Cell-scaffold interactions in the bone tissue engineering triad,” Eur. Cells Mater., vol. 26, pp. 120–132, 2013.

[12] A. R. Amini, C. T. Laurencin, and S. P. Nukavarapu, “Bone tissue engineering: Recent advances and challenges,” Crit. Rev. Biomed. Eng., vol. 40, no. 5, pp. 363–408, 2012.

[13] Y. J. Seol, D. Y. Park, J. Y. Park, S. W. Kim, S. J. Park, and D. W. Cho, “A new method of fabricating robust freeform 3D ceramic scaffolds for bone tissue regeneration,” Biotechnol. Bioeng., vol. 110, no. 5, pp. 1444–1455, 2013.

[14] G. Turnbull et al., “3D bioactive composite scaffolds for bone tissue engineering,” Bioact. Mater., vol. 3, no. 3, pp. 278–314, 2018.

[15] E. Babaie and S. B. Bhaduri, “Fabrication Aspects of Porous Biomaterials in Orthopedic Applications: A Review,” ACS Biomater. Sci. Eng., vol. 4, no. 1, pp. 1–39, 2018.

[16] K. Doi et al., “Development of Implant/Interconnected Porous Hydroxyapatite Complex as New Concept Graft Material,” PLoS One, vol. 7, no. 11, pp. 1–10, 2012.

[17] D. Martinez-Marquez, A. Mirnajafizadeh, C. P. Carty, and R. A. Stewart, Application of quality by design for 3D printed bone prostheses and scaffolds, vol. 13, no. 4. 2018.

[18] I. Denry and L. T. Kuhn, “Design and characterization of calcium phosphate ceramic scaffolds for bone tissue engineering,” Dent. Mater., vol. 32, no. 1, pp. 43–53, 2016.

[19] J. Henkel et al., “Bone Regeneration Based on Tissue Engineering Conceptions-A 21st Century Perspective,” Bone Res., vol. 1, pp. 216–248, 2013.
[20] X. Du, S. Fu, and Y. Zhu, “3D printing of ceramic-based scaffolds for bone tissue engineering: An overview,” J. Mater. Chem. B, vol. 6, no. 27, pp. 4397–4412, 2018.
[21] Q. Z. Chen and G. A. Thouas, “Fabrication and characterization of sol-gel derived 45S5 Bioglass®-ceramic scaffolds,” Acta Biomater., vol. 7, no. 10, pp. 3616–3626, 2011.
[22] C. Valeria, “Slides Corso di Medicina Rigenerativa ‘Fabrication methods of scaffolds’, Politecnico di Torino.” 2018.
[23] K. Szustakiewicz et al., “The influence of hydroxyapatite content on properties of poly(L-lactide)/hydroxyapatite porous scaffolds obtained using thermal induced phase separation technique,” Eur. Polym. J., vol. 113, no. January, pp. 313–320, 2019.
[24] V. Maquet, A. R. Boccaccini, L. Pravata, I. Notingher, and R. Jérôme, “Porous poly(α-hydroxyacid)-bioglass composite scaffolds for bone tissue engineering,” Biomaterials, vol. 25, no. 18, pp. 4185–4194, 2004.
[25] M. Degli Esposti, F. Chiellini, F. Bondioli, D. Morselli, and P. Fabbri, “Highly porous PHB-based bioactive scaffolds for bone tissue engineering by in situ synthesis of hydroxyapatite,” Mater. Sci. Eng. C, vol. 100, no. February, pp. 286–296, 2019.
[26] O. Bretcanu et al., “Electrospun nanofibrous biodegradable polyester coatings on Bioglass®-based glass-ceramics for tissue engineering,” Mater. Chem. Phys., vol. 118, no. 2–3, pp. 420–426, 2009.
[27] Y. Hong et al., “Preparation, bioactivity, and drug release of hierarchical nanoporous bioactive glass ultrathin fibers,” Adv. Mater., vol. 22, no. 6, pp. 754–758, 2010.
[28] F. Baino, G. Novajra, and C. Vitale-Brovarone, “Bioceramics and scaffolds: A winning combination for tissue engineering,” Front. Bioeng. Biotechnol., vol. 3, no. December, pp. 1–17, 2015.
[29] Q. Fu, M. N. Rahaman, B. Sonny Bal, R. F. Brown, and D. E. Day, “Mechanical and in vitro performance of 13-93 bioactive glass scaffolds prepared by a polymer foam replication technique,” Acta Biomater., vol. 4, no. 6, pp. 1854–1864, 2008.
[30] Q. Z. Chen, I. D. Thompson, and A. R. Boccaccini, “45S5 Bioglass®-derived glass-ceramic scaffolds for bone tissue engineering,” Biomaterials, vol. 27, no. 11, pp. 2414–2425, 2006.
[31] G. Tripathi and B. Basu, “A porous hydroxyapatite scaffold for bone tissue engineering: Physico-mechanical and biological evaluations,” Ceram. Int., vol. 38, no. 1, pp. 341–349, 2012.
[32] R. Gmeiner et al., “Additive manufacturing of bioactive glasses and silicate bioceramics,” J. Ceram. Sci. Technol., vol. 6, no. 2, pp. 75–86, 2015.
[33] V. Chiono, “Slides Corso di Medicina Rigenerativa ‘Scaffold Fabrication : Non conventional techniques : Rapid Prototyping’, Politecnico di Torino.” 2018.
[34] S. Bose, S. Vahabzadeh, and A. Bandyopadhyay, “Bone tissue engineering using 3D printing,” Mater. Today, vol. 16, no. 12, pp. 496–504, 2013.
[35] A. M. H. Ng et al., “Differential osteogenic activity of osteoprogenitor cells on HA and TCP/HA scaffold of tissue engineered bone,” J. Biomed. Mater. Res. - Part A, vol. 85, no. 2, pp. 301–312, 2008.
[36] D. W. Hutmacher, M. Sittinger, and M. V. Risbud, “Scaffold-based tissue engineering: Rationale for computer-aided design and solid free-form fabrication systems,” Trends Biotechnol., vol. 22, no. 7, pp. 354–362, 2004.

[37] J. O. Hollinger, T. A. Einhorn, B. A. Doll, and C. Sfeir, “Rapid prototyping technology and its application in bone tissue engineering,” J. Zhejiang Univ. B (Biomedicine Biotechnol., vol. 18, no. 4, pp. 303–315, 2017.
[38] M. Fantini, M. Curto, and F. De Crescenzio, “A method to design biomimetic scaffolds for bone tissue engineering based on Voronoi lattices,” Virtual Phys. Prototyp., vol. 11, no. 2, pp. 77–90, 2016.
[39] S. M. Giannitelli, D. Accoto, M. Trombetta, and A. Rainer, “Current trends in the design of scaffolds for computer-aided tissue engineering,” Acta Biomater., vol. 10, no. 2, pp. 580–594, 2014.
[40] C. Schmidleithner, “Master Thesis Additive Manufacturing of Tricalcium Phosphate Scaffolds for Bone Tissue Engineering,” Vienna University of Technology.
[41] F. Baino, J. Barberi, E. Fiume, G. Orlygsson, J. Massera, and E. Vern, “Robocasting of Bioactive SiO2-P2O5-CaO-MgO-Na2O-K2O Glass Scaffolds,” J. Healthc. Eng., vol. 2019, 2019.
[42] M. Moesen, T. Craeghs, J. P. Kruth, and J. Schrooten, “Robust beam compensation for laser-based additive manufacturing,” CAD Comput. Aided Des., vol. 43, no. 8, pp. 876–888, 2011.
[43] E. S. Bishop et al., “3-D bioprinting technologies in tissue engineering and regenerative medicine: Current and future trends,” Genes Dis., vol. 4, no. 4, pp. 185–195, 2017.
[44] A. D. Lantada, A. De Blas Romero, M. Schwentenwein, C. Jellinek, and J. Homa, “Lithography-based ceramic manufacture (LCM) of auxetic structures: Present capabilities and challenges,” Smart Mater. Struct., vol. 25, no. 5, 2016.
[45] C. Sun, N. Fang, D. M. Wu, and X. Zhang, “Projection micro-stereolithography using digital micro-mirror dynamic mask,” Sensors Actuators, A Phys., vol. 121, no. 1, pp. 113–120, 2005.
[46] Y. Mao, T. Miyazaki, K. Sakai, J. Gong, M. Zhu, and H. Ito, “A 3D printable thermal energy storage crystalline gel using mask-projection stereolithography,” Polymers (Basel)., vol. 10, no. 10, pp. 1–14, 2018.
[47] J. H. Lee, R. K. Prud’homme, and I. A. Aksay, “Cure depth in photopolymerization: Experiments and theory,” J. Mater. Res., vol. 16, no. 12, pp. 3536–3544, 2001.
[48] M. L. Griffith and J. W. Halloran, “Ultraviolet curable ceramic suspensions for stereolithography of ceramics,” Am. Soc. Mech. Eng. Prod. Eng. Div. PED, vol. 68–2, no. January 1994, pp. 529–534, 1994.
[49] C. J. Bae, A. Ramachandran, K. Chung, and S. Park, “Ceramic stereolithography: Additive manufacturing for 3D complex ceramic structures,” J. Korean Ceram. Soc., vol. 54, no. 6, pp. 470–477, 2017.
[50] A. de Blas Romero et al., “Lithography-based additive manufacture of ceramic biodevices with design-controlled surface topographies,” Int. J. Adv. Manuf. Technol., vol. 88, no. 5–8, pp. 1547–1555, 2017.
[51] S. P. Gentry and J. W. Halloran, “Depth and width of cured lines in photopolymerizable ceramic suspensions,” J. Eur. Ceram. Soc., vol. 33, no. 10, pp. 1981–1988, 2013.
[52] C. Hinczewski, S. Corbel, and T. Chartier, “Ceramic suspensions suitable for stereolithography,” J. Eur. Ceram. Soc., vol. 18, no. 6, pp. 583–590, 1998.
[53] J. Bennett, “Measuring UV curing parameters of commercial photopolymers used in additive manufacturing,” Addit. Manuf., vol. 18, pp. 203–212, 2017.
[54] F. Scalera, C. Esposito Corcione, F. Montagna, A. Sannino, and A. Maffezzoli, “Development and characterization of UV curable epoxy/hydroxyapatite suspensions for

stereolithography applied to bone tissue engineering," Ceram. Int., vol. 40, no. 10, pp. 15455–15462, 2014.
[55] T. Chartier, C. Chaput, F. Doreau, and M. Loiseau, "Stereolithography of structural complex ceramic parts," J. Mater. Sci., vol. 37, no. 15, pp. 3141–3147, 2002.
[56] J. W. Halloran et al., "Photopolymerization of powder suspensions for shaping ceramics," J. Eur. Ceram. Soc., vol. 31, no. 14, pp. 2613–2619, 2011.
[57] G. Mitteramskogler et al., "Light curing strategies for lithography-based additive manufacturing of customized ceramics," Addit. Manuf., vol. 1, pp. 110–118, 2014.
[58] E. Schwarzer, M. Götz, D. Markova, D. Stafford, U. Scheithauer, and T. Moritz, "Lithography-based ceramic manufacturing (LCM) – Viscosity and cleaning as two quality influencing steps in the process chain of printing green parts," J. Eur. Ceram. Soc., vol. 37, no. 16, pp. 5329–5338, 2017.
[59] C. Schmidleithner, S. Malferarri, R. Palgrave, D. Bomze, M. Schwentenwein, and D. M. Kalaskar, "Application of high resolution DLP stereolithography for fabrication of tricalcium phosphate scaffolds for bone regeneration," Biomed. Mater., vol. 14, no. 4, pp. 1–11, 2019.
[60] Y. Zeng et al., "3D printing of hydroxyapatite scaffolds with good mechanical and biocompatible properties by digital light processing," J. Mater. Sci., vol. 53, no. 9, pp. 6291–6301, 2018.
[61] R. Felzmann et al., "Lithography-based additive manufacturing of cellular ceramic structures," Adv. Eng. Mater., vol. 14, no. 12, pp. 1052–1058, 2012.
[62] Y. Pan, C. Zhou, and Y. Chen, "Rapid manufacturing in minutes: The development of a mask projection stereolithography process for high-speed fabrication," ASME 2012 Int. Manuf. Sci. Eng. Conf., pp. 405–414, 2012.
[63] Y. Lu, G. Mapili, G. Suhali, S. Chen, and K. Roy, "A digital micro-mirror device-based system for the microfabrication of complex, spatially patterned tissue engineering scaffolds," J. Biomed. Mater. Res. - Part A, vol. 77, no. 2, pp. 396–405, 2006.
[64] L. H. Han, G. Mapili, S. Chen, and K. Roy, "Projection microfabrication of three-dimensional scaffolds for tissue engineering," J. Manuf. Sci. Eng. Trans. ASME, vol. 130, no. 2, pp. 0210051–0210054, 2008.
[65] I. Potestio, "Lithoz: How lithography-based ceramic AM is expanding the opportunities for technical ceramics," Powder Inject. Mould. Int., vol. 13, no. 2, pp. 2–5, 2019.
[66] C. Mangano, F. Mangano, L. Gobbi, O. Admakin, S. Iketani, and A. Giuliani, "Comparative study between laser light stereo-lithography 3D-printed and traditionally sintered biphasic calcium phosphate scaffolds by an integrated morphological, morphometric and mechanical analysis," Int. J. Mol. Sci., vol. 20, no. 13, 2019.
[67] P. Tesavibul et al., "Biocompatibility of hydroxyapatite scaffolds processed by lithography-based additive manufacturing," Biomed. Mater. Eng., vol. 26, no. 1–2, pp. 31–38, 2015.
[68] Y. Yao, N. Sha, and Z. Zhao, "Highly Concentrated Hydroxyapatite Suspension for DLP Printing," IOP Conf. Ser. Mater. Sci. Eng., vol. 678, no. 1, pp. 1–8, 2019.
[69] P. Tesavibul et al., "Processing of 45S5 Bioglass® by lithography-based additive manufacturing," Mater. Lett., vol. 74, pp. 81–84, 2012.
[70] C. Ghayor and F. E. Weber, "Osteoconductive microarchitecture of bone substitutes for bone regeneration revisited," Front. Physiol, vol. 9, pp. 1–10, 2018.

[71] Z. Liu et al., “Additive manufacturing of hydroxyapatite bone scaffolds via digital light processing and in vitro compatibility,” Ceram. Int., vol. 45, no. 8, pp. 11079–11086, 2019.
[72] C. Feng et al., “Additive manufacturing of hydroxyapatite bioceramic scaffolds: Dispersion, digital light processing, sintering, mechanical properties, and biocompatibility,” J. Adv. Ceram., vol. 9, no. 3, pp. 360–373, 2020.
[73] Y. Cao et al., “Fabrication and properties of zirconia/hydroxyapatite composite scaffold based on digital light processing,” Ceram. Int., vol. 46, no. 2, pp. 2300–2308, 2020.

Chapter 3

Materials & Method

In the present study, HA-based scaffolds for the regeneration of bone defects were produced.
Digital Light Processing (DLP) - Based Stereolithography (SLA) with bound surface using an LED radiation source in the blue visible region.
As explained in chapter 2, DLP process is able to produce batches of complex structures that can be marketed in a short time without affecting resolution, which remains one of the strengths of this additive technique.
DLP also allows us to obtain highly porous and interconnected scaffolds so as to meet one of the main requirements of BTE, discussed in chapter 2.
Like most of AM techniques, the construction of scaffolds by means of the DLP process is based on a Computer-Aided Design (CAD) model, which may derive from the patient's medical μ-CT imaging or from computer-built models based on simpler porous geometries which, however, may not be able to properly replicate the trabecular architecture of cancellous bone.
In order to overcome this limit, the present study combined the enormous potential of DLP with the well-established use of PU trabecular-like foams, used in BTE since 2006 for the production of scaffolds by foam replication technique. In particular, it was decided to use a CAD model based on μ-CT reconstruction of an open-cell polymeric commercial sponge (45 ppi), thus obtaining a complex and standardized scaffold, adaptable to different types of patients and, therefore, more marketable.
Combining this strategy with the choice to use one of the most appreciated techniques for the processing of ceramic material, it was possible to obtain HA scaffolds (one of the most used CaPs in BTE, thanks to its biocompatibility and properties of osteoconductivity), with a trabecular architecture similar to that of spongy bone tissue (cancellous bone).
The first part of the thesis work was conducted at Lithoz GmbH (Austria), where the production of the slurry and its subsequent characterization was carried out, considering the viscosity, the density of the material produced, the optimization of the printing process parameters and finally the additive construction of the scaffolds using the CeraFab 7500 machine.
From the μ-CTs images of the commercial sponge, the STL file of an almost perfectly cubic (4.72x 5x5.15 mm) porous scaffold was obtained. Afterwards, the geometry of the scaffold was modified, doubling the starting structure and superimposing the new mirror image along the longitudinal axis in order to obtain a cylinder with an aspect ratio 2:1.
In order to evaluate the possibility of also using the LithaBone 480 E slurry for the printing of non-porous structures, 3 sets of hollow cylinders of the same size as the porous cylindrical scaffolds were manufactured, differing from one another in the thickness between the outer and inner surface.

During the period of time spent at Lithoz GmbH, a total of 90 porous cylindrical scaffolds, 30 porous cubic scaffolds, and 3 different sets of 45 non-porous cylinders were produced.
The second part of the work carried out at the DISAT laboratory of Politecnico di Torino (Italy) aimed to conduct a morphological and chemical analysis of the scaffolds produced. X-Ray Diffraction (XRD) analysis was carried out to assess the crystalline phase of the scaffold, while the Scanning Electron Microscopy (SEM) and Energy Dispersive Spectrometry (EDS) were respectively perform to analyse morphological and compositional features of the scaffolds.

The materials and methods used in the present work are here presented. Table 1 provides an overview of the activities, detailing the instrumentation used to finalize each task.

Table 1. Overview of materials and methods used for the job.

Task	**Instrument and Software or Material**	**Location**
LithaBone 480E Preparation	HA powder and Organic Binder	Lithoz GmbH, Vienna
Scaffold Design	- InVesalius Bitmap – InVesalius 3 - Autodesk Netfabb 2019	Lithoz GmbH, Vienna
Manufacturing	- Lithoz Cerafab 7500 System - CeraCleaning Station Ultra - Nabertherm P330 oven	Lithoz GmbH, Vienna
Slurry Analysis	- Sartorius kit Skyscan 1172 - Rotational Rheological Test with a RCM Rheometer series. - MTS Electromechanical Universal Testing Systems - Microscope: Opto S\N KL LCD	Lithoz GmbH, Vienna
Scaffold Analysis	- JCM – 6000Plus Versatile Benchtop SEM JEOL - PANalytical diffractometer and X'Pert HighScore	DISAT Laboratory, Politecnico of Turin

3.1 Slurry Preparation

A new type of photocurable slurry named LithaBone 480E was developed basing on LithaBone 400, already used and characterized in the past by Lithoz GmbH.
Initially, commercially available HA ($[Ca_{10}(PO_4)_6](OH)_2$) powders, supplied by Lithoz GmbH, were dried for about 24h at 120 °C and added in 3 steps to the previously prepared organic matrix containing solvent, reactive monomers and photoinitiator (usually less than 1 wt%).
At each step, a precise amount of powders was added to the matrix; it was necessary to blend in the material to ensure that the final result would be a homogeneous slurry. The SpeedMixerTM DAC 400.1 FVZ (Hauschild, Germany) was used for this purpose: it works with a Dual Asymmetric Centrifuge consisting of a mixing arm and a mixing cup, rotating in opposite directions. This combination of forces allows obtaining a fast and effective mixing. The slurry was mixed for 30 s at 1800 rpm and then for 30 s at 2750 rpm.
Once all the powders were added to the binder, the slurry underwent a dispersion process with milling beads for 3 h.
Finally, a rehological additive was added to the formula to improve the stability of the final uncured slurry which was then placed in storage at a constant temperature of 5°C, ready for use.
The development and study of LithaBone 480 E was aimed in particular at improving the binder formula, in order to make it more volatile compared to the previous one used in LithaBone 400. A more volatile binder, indeed, is necessary to avoid cracks or breaks on the scaffold surface after sintering.
The main steps performed to prepare the slurry are shown in Figure 1.

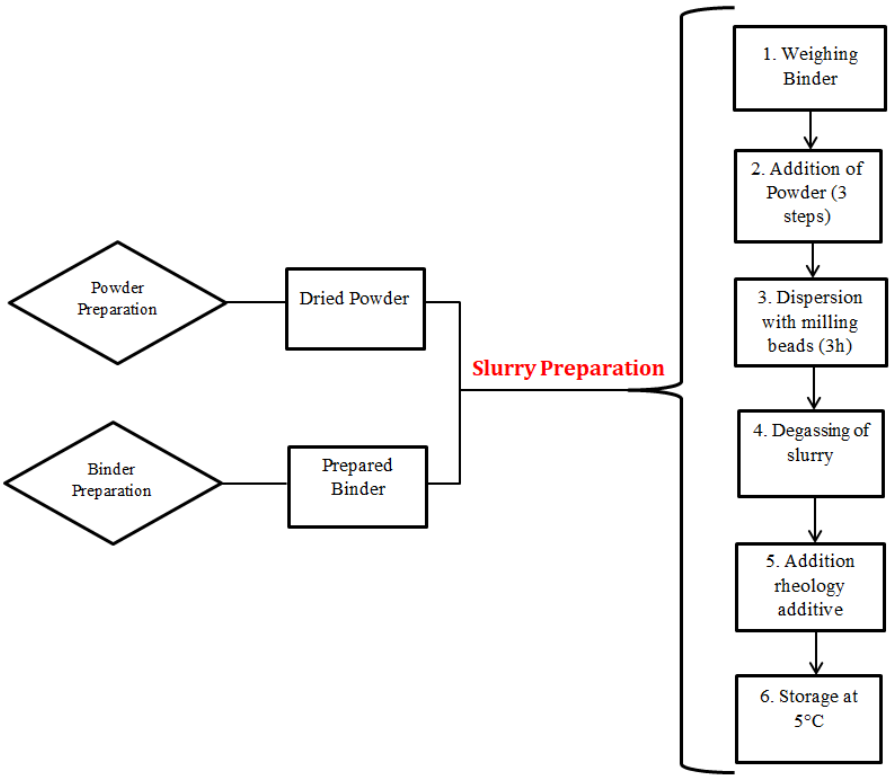

Figure 1. Flowchart for Slurry LithaBone 480E preparation.

The volumetric ratio between ceramic powder and binder was calculated in order to obtain a slurry with a viscosity that can be used for DLP printing.
The weight of the powder was calculated using the theoretical HA density of 3.156 g/cm^3 [23] .

3.2 Manufacturing

3.2.1 Pre-Processing: CeraFab Data Pre-processing (DP) Software

The CeraFab system is based on jobs previously created using the CeraFab DP (Data Pre-processing) system. The starting point is a 3D CAD file in .STL format which, through the software, is modified into fab-file format so that it can be recognized by the CeraFab 7500 machine. Thanks to this software, the project may be manipulated through a virtual platform known as "tray" (Figure 2) and all process parameters may be set, including the number of pieces to be printed for each single job, as well as their position and orientation within the building platform.
The software distinguishes between two types of layers: the "start layers", i.e. the first layers produced during the printing process, and all the subsequent layers ("general layers") which make up the greater part of the structure [1].
A summary of the 4 steps needed to completely and correctly define the characteristic of the work is given below:

1. **Machine & Material**: selection of the CeraFab machine and the type of material to be used.

2. **Tray**: setting of the number of equal parts to be printed simultaneously, their relative distance and orientation in space.

3. **Parameters**: selection of the main printing parameters. There are 3 different sets of parameters:

- General settings: layer thickness (µm), exposure time start (s), exposure time general (s), exposure intensity start (mW/cm²), exposure intensity general (mW/cm²), shrinkage compensation factor (XY) and shrinkage compensation factor (Z);

- Waiting times: time exposure start (s) and waiting time exposure general (s);

- Velocities and moving distance: rotation speed start (steps/s), rotation speed general (steps/s), tilting down start (steps/s) and rotation angle start (°).

4. **Finalization**: The last step involves error check and data saving. During this phase, a preview of the project divided into all its individual layers is also provided, according to the pre-defined settings. Moreover, the estimated slurry consumption is provided.
   Once the project has been checked, the fab - file can be sent directly to the chosen CeraFab machine.

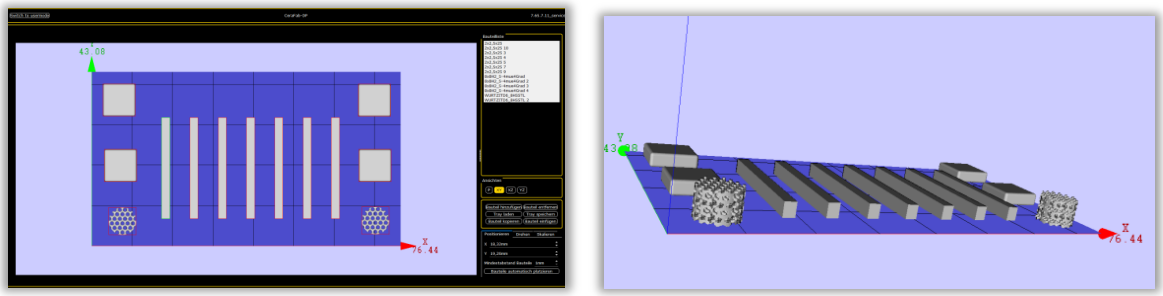

Figure 2. Step 2: Virtual Tray for “Stability Tray Test” in different orientations.

3.2.2 Processing

Following will illustrate the CeraFab 7500-system provided by Lithoz GmbH, with its main features, components and the operating software.

3.2.2.1 Lithoz GmbH CeraFab 7500 - system

The Lithoz CeraFab 7500 – 28 system (Figure 3) was the machine used for the production of HA scaffolds at Lithoz GmbH.

Building envelope (X,Y,Z)	~ 76 mm x 43 mm x 150 mm
Pixel	1920 x 1080
Resolution	40 µm (635 dpi)
Layer thickness	25 – 100 µm
Light Source	Light emitting diodes (LEDs)
Manufacturing speed	up to 10 mm per hour
Data type	.stl (binary)

Figure 3. CeraFab 7500 system [1].

The CeraFab 7500 system uses the Digital Light Processing (DLP) based stereolithography (SLA) method, previously described in Chapter 2.
This system is among the most popular for the manufacture of complex 3D ceramic structures. State-of-the-art industrial electronics, as well as the opportunity to control the manufacturing of the part in real time, guarantee absolute precision of the printed object (in the micrometer range) combined with short production times.
The Cerafab system allows different types of ceramic powder (e.g. Alumina, Silica, TCP, Magnesia, Porcelain and HA) to be homogeneously dispersed within the organic matrix containing reactive monomers, solvent and photoinitiator.
The setup is a constrained surface DLP (digital mirror device) system with an LED radiation source in the blue visible light.
The light engine utilizes powerful LEDs as a light source and a DMD (digital mirror device) chip as a dynamic mask with a resolution of 1920 × 1080 pixels and a pixel size of 40 × 40 µm [2].
The DMD - chip of CeraFab 7500 guarantees a selective photopolymerization of the layer; the resolution in the x/y plane is 40 µm and a single layer thickness that can vary between 25 - 100 µm, depending on the manufacturer's choice.
Layer-by-layer production involves the addition of fresh slurry every time a layer is produced. Figure 4 illustrates how the light source radiates from below the rotating vat uniformly filled with slurry.
When the photoinitiator is hit by external light, it forms free radicals which start the polymerization by reacting with the monomers contained in the mixture.. The chain reaction forms the desired matrix of monomers that will bind the ceramic particles together in the desired pattern.
Compared to other methods of vat photopolymerization, the parts produced are no longer immersed in the slurry and this not only reduces the amount of material required but also the risk of introducing defects during construction [3].

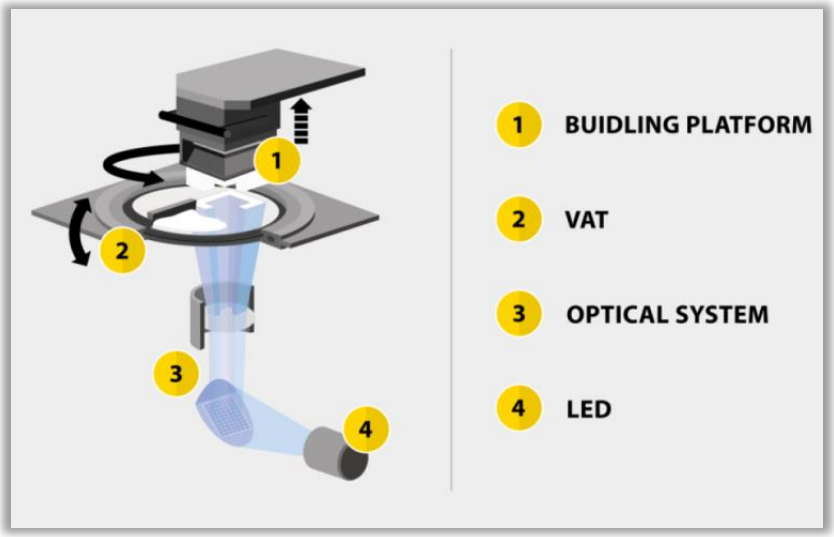

Figure 4. Functional principle of the ceramic DLP-system by Lithoz GmbH; the arrows indicate the directions along which the building platform and the vat move [1].

Figure 5 illustrates the machine's workspace and its main components:

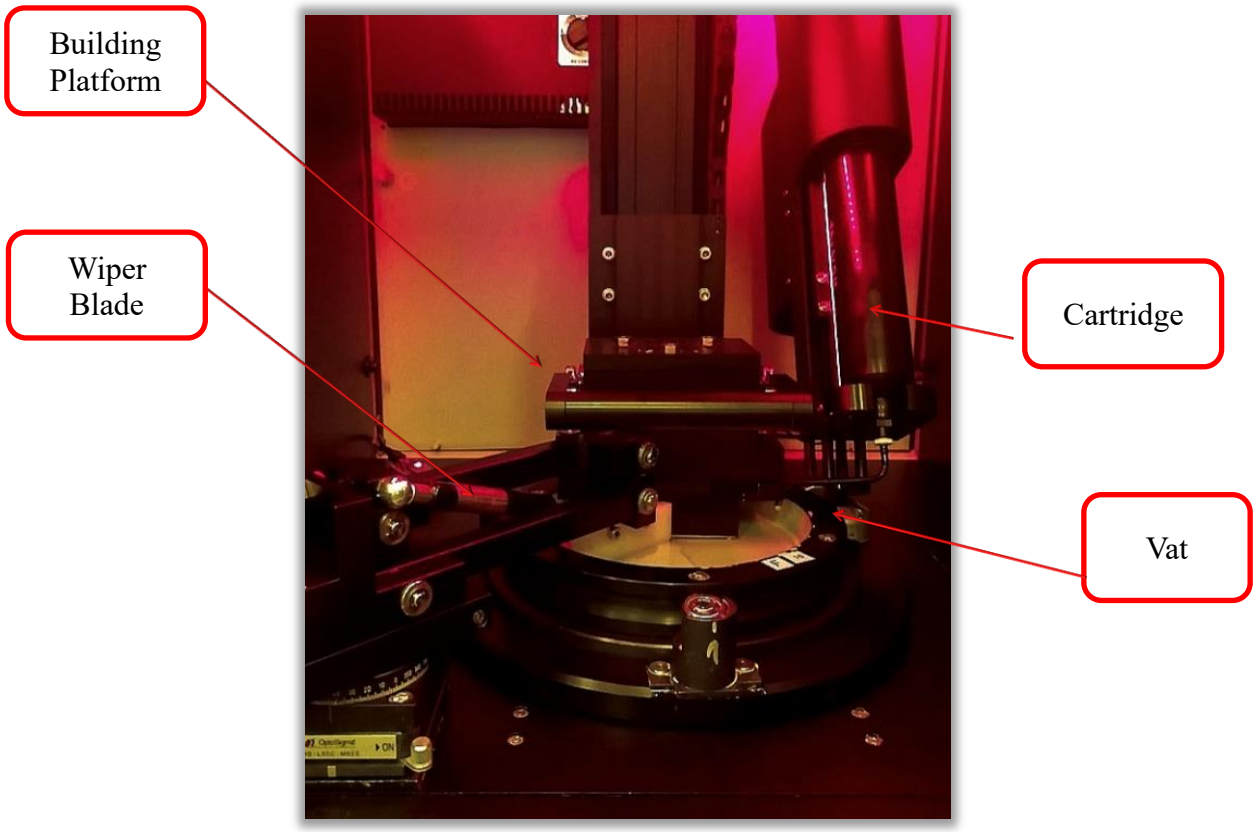

Figure 5. Workspace of the CeraFab 7500 – 28.

The workspace of CeraFab 7500-282 is composed of:

- **Rotation Vat:** contains the liquid slurry and is coated with new material after each new layer is formed. The vat consists of a layer of transparent glass interposed with a layer of silicon. The lower layer of the vat is irradiated by the light source.
  It is worth noting that the newly created layer does not remain attached to the surface of the vat, but that all layers are firmly fixed to each other and attached to the building platform. To reduce the forces of interaction between the scaffold under construction and the surface of the vat, the latter is coated with a hydrophobic silicone film. In addition, after polymerization of the layer, one side of the vat is slowly lowered before the other, in order to facilitate the detachment of the new layer from the surface.

- **Building Platform:** is placed above the vat and forms the basis for the construction of the structure. It consists of a metal body and a glass plate and can only move along the z axis. To improve the adhesion between the building platform and the scaffold under construction, the glass platform has been coated with an FDM Adhesion Foil.

- **Cartridge:** contains the slurry. Through a controlled dosing system, new liquid slurry is added to the vat each time the next layer is formed.

- **Wiper blade:** its task is to evenly distribute the new slurry added to the vat after the construction of a layer. When adjusting the position of the wiper blade, the height of the slurry on the vat may be modified; the initial slurry thickness is one of the two parameters which must be checked before initiating the printing process.

3.2.2.2 CeraFab Hardware Control (HC)

CeraFab Hardware Control (HC) is the user interface for direct interaction with the Cerafab 7500 machine. Through the machine's touch screen, the operator can start printing, check the process status, the number of layers being printed and the time required to complete the job, move the building platform and check the general machine status [1].
The HC control panel provides access to the software directory of the machine to which the fab - file previously created with CeraFab DP has been transferred.
After selecting and confirming the working file, this is loaded and the slicing starts. During slicing the parts are cut into individual layers, according to the predefined layer thickness.
Two mandatory checks, described below, must be performed from the control panel before starting to print, as the accurate assembly of the vat, the building platform and the wiper blade are not sufficient to guarantee a good final result of the product printing; it is thus necessary to:

1. Ensure that the slurry evenly covers the vat's surface by sing a rubber spatula to pour the slurry, taking care not to rub against the vat. Then, through the control panel, set the continuous rotation of the vat to about 1 minute so that the material is evenly distributed on the surface.
   Finally, measure the initial level of liquid slurry present in the vat and if the height does not reflect the desired level, change the position of the wiper blade.
   In the present work, the height of the slurry in the vat was 175 µm.

2. Make sure that vat and building platform are parallel to each other.
   This alignment is essential for the success of the manufacturing run and the quality of the fabricated parts.

Once the fab-file has been loaded and all aspects of the machine have been checked, printing may begin. The process starts with a complete rotation of the vat, then the building platform lowers towards the vat until there is space left which is equal to the height you wish to achieve for a single layer. The next step involves the selective exposure of the slurry to visible blue light with consequent polymerization of the desired part. To facilitate the separation between the newly formed layer and the surface of the vat, the latter is slowly tilted downwards and at the same time the building platform is raised as much as the height of a single layer. The sequence of the process is then repeated, as the next layer is formed, and so on until the entire job is completed.

The Table 3 shows all the various types of tests conducted during the Lithoz period to characterize the LithaBone 480E slurry and the printing work to obtain the final porous scaffolds. All tests will be explained in detail below.

Table 3. Tests/ Jobs conducted in Lithoz GmbH.

Tests/ Jobs	Chapter	Geometry of printed samples	Aim
Stability Tray Test	3.3.	7 compact bars (2.5x2x25 mm) 4 cuboids 2 porous open - cell cylinders	3 - point bending strength test, density test and evaluation of the feasibility of printing scaffolds with controlled porosity.
Viscosity test	3.3.1.	Uncurred LithaBone 480E slurry	Rehological behaviour of LithaBone 480E slurry.
Grindometer test	3.3.2.	Uncurred LithaBone 480E slurry	Check the degree of dispersion of ceramic particles into the LithaBone 480E.
Shrinkage factor	3.3.5.	18 compact bars (2.5x2x25 mm)	Evaluate the shrinkage factor in x-y direction and z direction.
Design specification for printing	3.4.	Different sample geometries use pre-existing fab-files	Check of: - Wall thickness - Aspect Ratio - Overhangs - Minimal Feature and overpolymerization
Non-porous scaffolds	3.5.1.	3 different sets of compact cylinders	Evaluate the possibility of printing non-porous scaffolds.
Cubic porous scaffolds	3.5.2.	Cubic scaffold (4.72x5.15x5.0 mm)	The aim of the thesis: obtaining bone-like bioceramic scaffolds using μ-CT with DLP process.
Cylindrical porous scaffolds	3.5.2.	Cylindrical scaffold (5x5x10 mm)	The aim of the thesis: obtaining bone-like bioceramic scaffolds with aspect ratio 2:1 using μ-CT with DLP process.

3.2.3 Post –Processing

In order to obtain a strong ceramic part and remove the organic binder, cleaning, drying and sintering of the green bodies were required after printing.

3.2.3.1 Cleaning

Green samples (Figure 6) were removed from the building platform using razor blades and cleaned meticulously to eliminate the uncured slurry.
The test specimens, cylinders and porous scaffolds were then cleaned using a cleaning agent provided by Lithoz; smooth and absorbent paper and pressurized air were then used to remove residuals within the micrometric cavities.
After cleaning, green samples were stored at 30°C for no longer than 5 days and then sintered

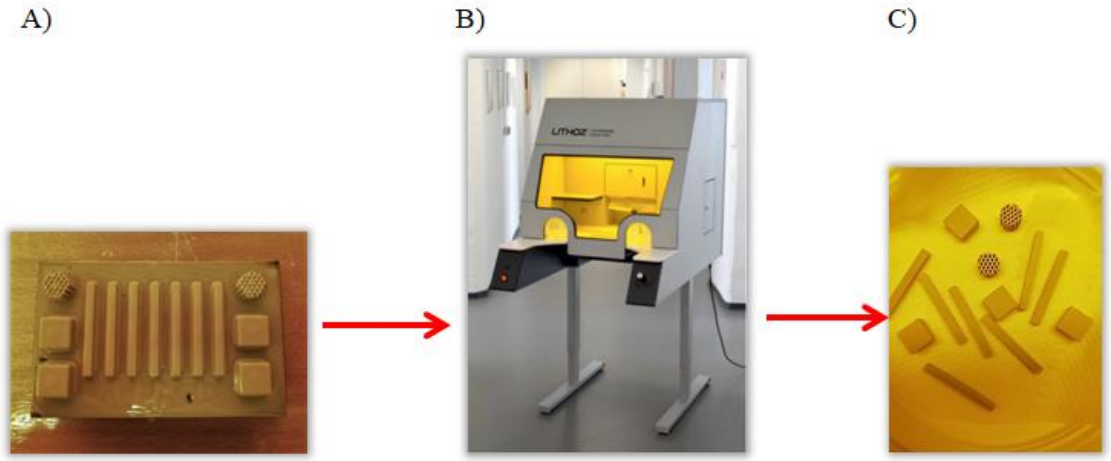

Figure 6. A) Just printed green samples on the building platform; B) CeraCleaning Station Ultra for sample cleaning; C) Clean green samples.

3.2.3.2 Sintering process

After eliminating the uncured slurry, the green samples were subjected to the final heat treatment to completely remove the organic part and obtain ceramic solid parts with superior mechanical properties and density; removing the binder from the green bodies, in fact, is necessary as it may contain harmful substances for the human body.
To remove the organic matrix, the samples were sintered using the high-temperature Nabertherm P330 chamber furnace (Figure 7).
Starting from 25 °C, the temperature was gradually raised to eliminate the solvent contained in the slurry and its organic component, thus avoiding the formation of internal stresses resulting from high temperature gases.
The total sintering time was 99 h (~ 4 days), and a maximum temperature of 1300°C, maintained for about 2 hours, was reached in order to obtain a compact final part.
Figure 8 shows the temperature program for sintering HA green bodies.
Just for the sintering of porous scaffolds, an IPS Object Fix Flow between the scaffold and the support platform was used in order to guarantee better adherence to the support.
IPS Object Fix is an auxiliary paste consisting of water oxides and thickeners used to stabilize and fix the sample to the holder. Thanks to their consistency, IPS Object Fix pastes are easy to apply and can be effortlessly removed once the sintering process is complete.

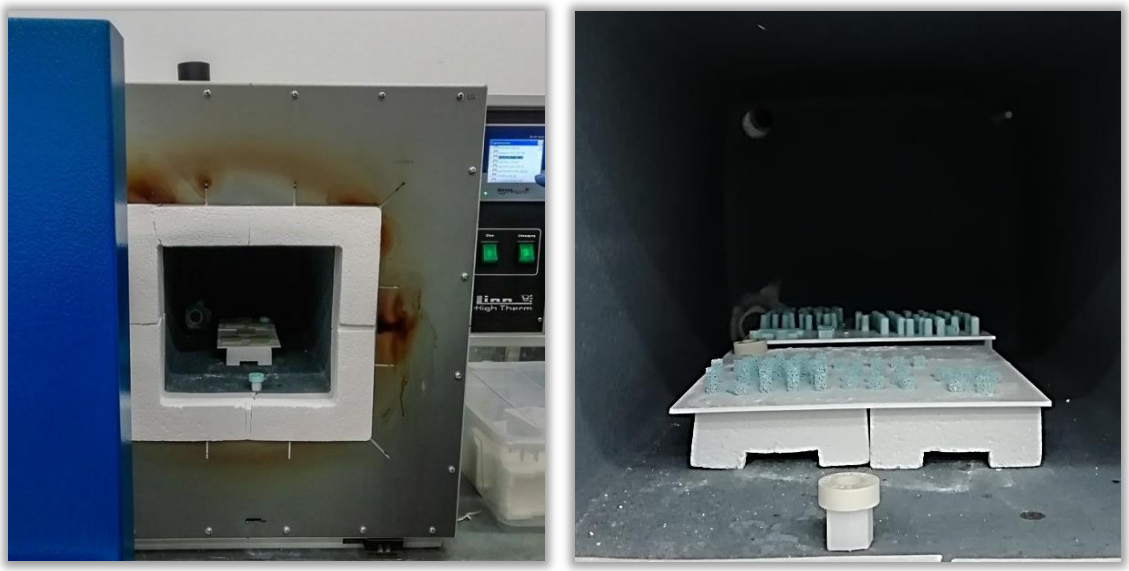

Figure 7. Nabertherm P330 oven used for sintering process.

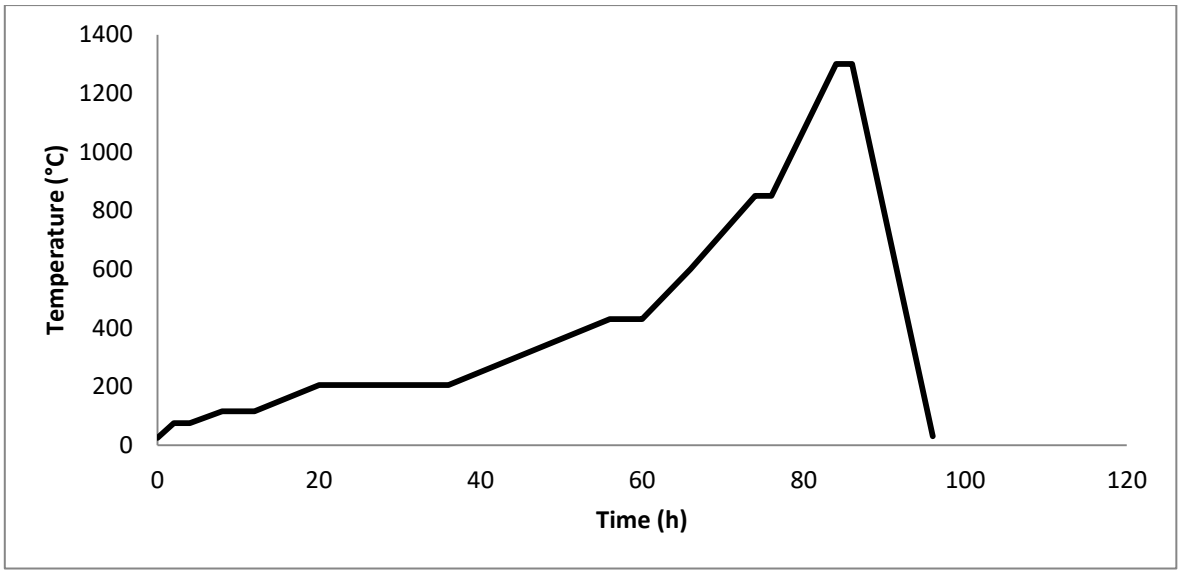

Figure 8. Temperature program for sintering of HA green parts.

3.3 Slurry characterization

Before proceeding with the printing of the scaffolds, it was necessary to conduct preliminary tests on the new LithaBone 480E material developed in order to evaluate its chemical-physical characteristics, strengths and printing limits.

A "Stability tray test" job was set up to monitor any changes in slurry over the weeks. The Tray included checking and calculating the viscosity of LithaBone 480E slurry, relative density,

grindometer test, 3 - point bending strength test of the material. This procedure was repeated once a week for 5 consecutive weeks.
The LithaBone 480 E slurry produced was then divided into 5 containers stored inside a refrigerator kept at a constant temperature of 5°C. Each container contained 60 g of slurry.
For the density test and 3 - point bending test, using a preset work file (see Figure 9. A)), 7 compact bars of size 2.5x2x25 mm, 4 cuboids and 2 porous open - cell cylinders were printed each time: 3 - point bending strength test, density test and evaluation of the feasibility of printing scaffolds with controlled porosity.
Since less than optimal results were obtained for the 4 cuboids after the sintering process, it was decided to use the bars for the density test as well.
Finally, the slurry shrinkage factor was also calculated, an indispensable parameter to obtain final sintered scaffolds of the desired size (see Figure 9. B)).

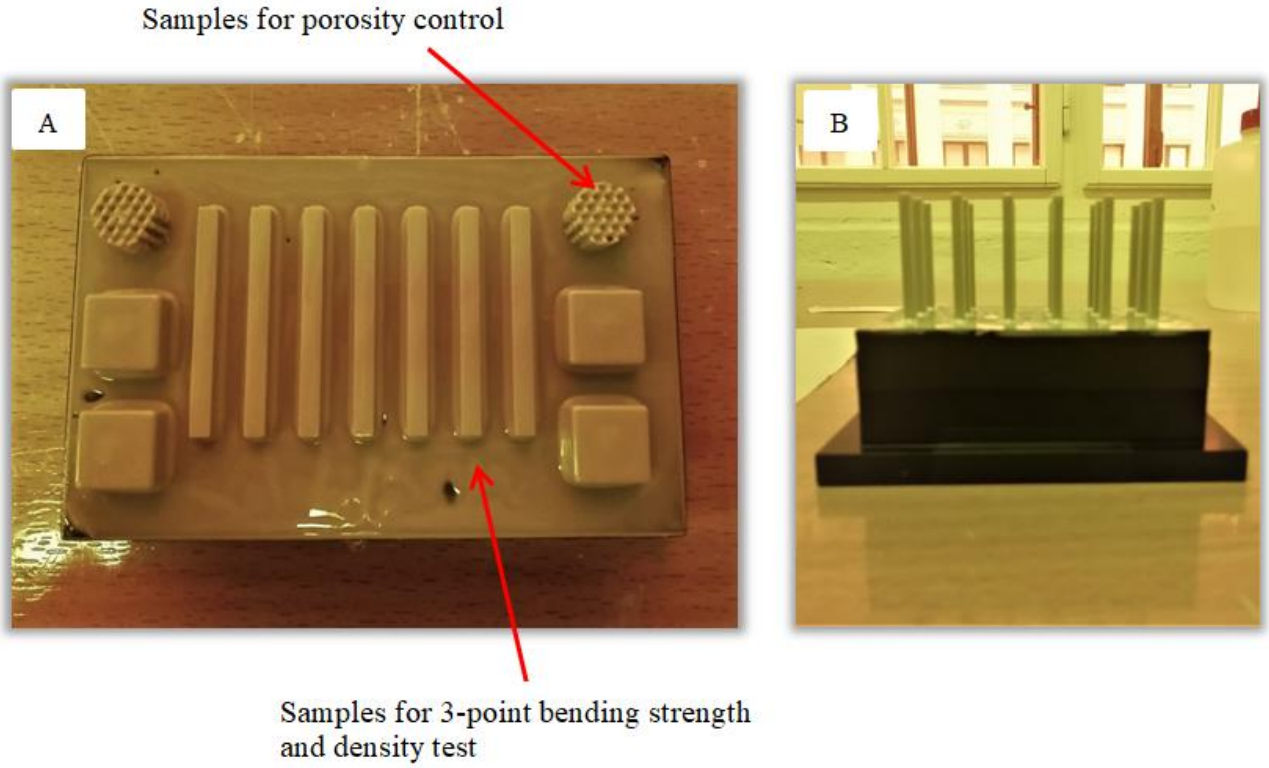

Figure. 9.A) Samples for “Stability Tray test”; 9.B) Samples for shrinkage parameter.

3.3.1 Viscosity test

Analyzing the rheological behavior of the slurry is foundamental for the optimization of printing parameters in the DLP process. In order to obtain sufficiently strong scaffolds, it is indeed necessary to find a compromise between ease of printing and good mechanical properties of the final product.
A high percentage of initial powders guarantees high density scaffolds with satisfactory mechanical properties; however, this causes an inevitable increase in slurry viscosity and a consequent increase in printing difficulties and times. If the slurry viscosity is too high, printing accuracy will not be

guaranteed [4].

Viscosity is a physical quantity that measures the resistance of a fluid to slurry when a tangential force is applied [5].
Newton's law states that if the shear rate is directly proportional to the applied stress (shear stress) and independent of time, then this fluid is called Newtonian and obeys Newton's equation (1):

$$\tau = \frac{F}{A} \qquad (1)$$

τ= shear stress (Pa)
A= surface (m^2)
F= applied force (N)

By determining the values of velocity gradient γ and shear stress τ we can define the viscosity as the resistance that opposes the motion of the fluid, as it is shows in equation (2):

$$\eta = \frac{\tau}{\dot{\Upsilon}} \qquad (2)$$

η= Viscosity (Pa·s)
τ= Shear stress (Pa)
$\dot{\Upsilon}$= Shear rate (s^{-1})

Fluids that do not exhibit Newtonian behavior are called non-Newtonian (Figure 10) and are usually divided into:

1. **Pseudo-plastic Fluids (shear thinning fluids)**: the shear rate increases with increasing shear stress. For high shear rate values, the fluid deforms more easily, and its viscosity tends to decrease [6].

2. **Dilatan fuid (shear thickening fluids)**: the shear rate decreases with increasing shear stress. For high shear stress values, the fluid tends to deform with difficulty because the viscosity increases [5].

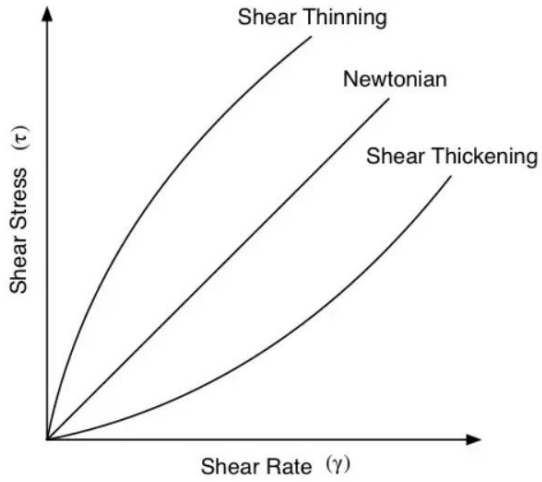

Figure 10. Shear Stress vs. Shear Rate diagram for different kinds of fluids [6].

Rheology is the science that studies the behavior and deformation of fluids in motion, and by means of rheometers it is possible to determine the deformation and flow behavior of all kinds of materials.
The two most common types of rheological tests are rotation and oscillation (Figure 11).

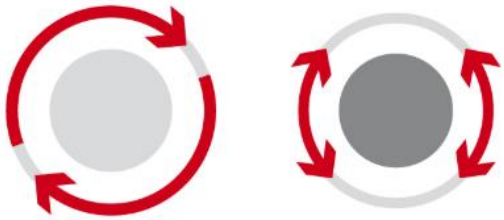

Figure 11. Rotational movement and oscillation movement.

An RCM Rheometer series was used for the test; this can operate in two different modes, depending on the preset parameters:

a) **CSR, via rotational speed**: checking the rotation speed (shear rate $\dot{\Upsilon}$) determines the shear stress τ;

b) **CSS, via torque**: by pre-setting a driving force, the rotation speed and thus the shear rate can be determined $\dot{\Upsilon}$.

Specific conversion factors permit the conversion of the driving force to τ and the rotational speed to $\dot{\Upsilon}$ [7].

In any case, whenever a rheological test is carried out, it is extremely important to check the exact temperature of the sample; in fact, most rheological parameters are influenced by the latter [7].
Rheological analysis was important to control the stability of the suspension over time and the possible tendency of the particles to sediment, as well as being useful to identify the minimum

concentration of organic component to be used to produce a slurry of adequate viscosity; in fact, by incorporating a higher quantity of diluents, an excessively high viscosity can be lowered [8].
For the viscosity analysis of the LithaBone 480E slurry, it was decided to use the Rotational mode because it allowed to accurately monitor the flow and viscosity curve of the sample and required a small amount of material compared to the oscillatory method.

3.3.2 Grindometer Test

Some kind of solid materials must be ground into fine particles to be dispersed be dispersed within a liquid matrix.
When dealing with dispersion properties of solid particulates , also called “grinds”, it is important to analyze not only the actual size of the individual particles but also the degree of dispersion achieved [9].
To determine the fineness of grinds and detect the presence of large dispersed particles or agglomerates, a special meter called a grindometer was used, with a beveled scraper to distribute the material on it (Figure 12). The grindometer is a stainless-steel fineness of grind gauge, on the surface of which there are one or two grooves of increasing depth. The depth can be measured using the laterally engraved scales; grindometers are usually available with a mil or micron scale (1 mil = 25.4 microns) [10].
The non-light cured slurry was applied at the deepest point of the measuring groove and with the help of the beveled scraper was spread transversely to the opposite end of the grindometer. The result visible on the scale corresponded to the most frequent size of the scattered particles [9], [11].
This method did not provide the exact particle size but gives information on the presence of large particles and their approximate size, allowing the production processes to be followed in real time and without needing to use large amounts of material as a sample [11].

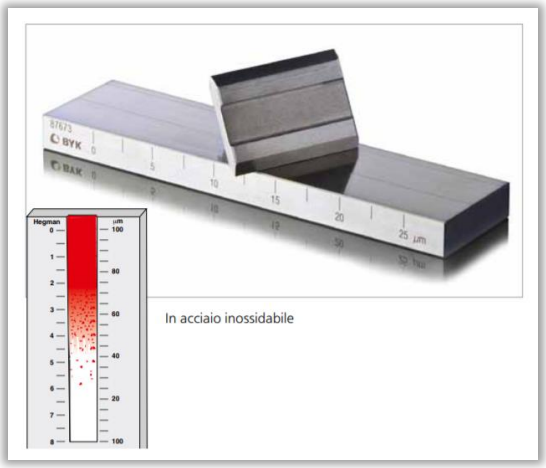

Figure 12. Kit component for Grindometer Test [9].

Again, it was considered necessary to repeat the test once a week for 5 weeks in order to check if HA particles could agglomerate over time, thus modifying the slurry viscosity.

3.3.3 Archimedean Density

For the calculation of the relative density and for the 3-point bending strength test, 3 of the 7 bars (2 x2.5x25 mm) of LithaBone 480E from the "Stability Tray" job were used.
The fab-file used to print the bars and the green samples obtained can be seen in Figure 2 and Figure 6, respectively.

The density of the material is calculated on the basis of Archimedes' Principle which states:

"*The upward buoyant force that is exerted on a body immersed in a fluid, whether fully or partially submerged, is equal to the weight of the fluid that the body displaces*" [12].

For this test we used special scales and a Sartorius density determination kit YDK 01 (Figure 13).

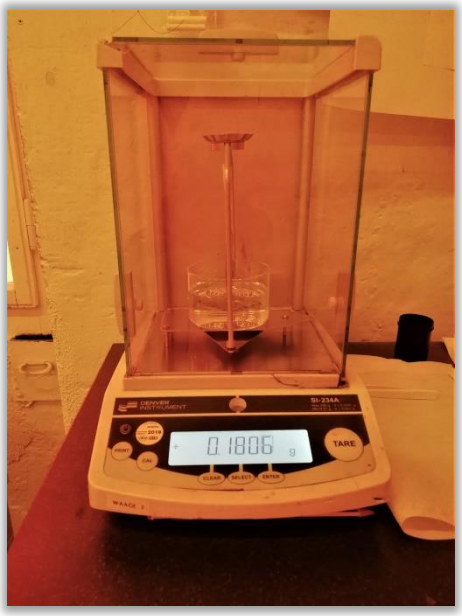

Figure 13. Sartorius density determination kit YDK 01.

For each test, 3 of the 7 bars of the same print job were used; the samples were weighed in air, water and in a wet state, and the average of the 4 measurements was taken for each state.
To determine the mass of the component in water, the sample was placed on the lower part of the scales and submerged in distilled water. To reduce the surface tension and avoid the unwanted formation of bubbles, two drops of liquid soap were added to the water container.
Finally, before proceeding with the calculation, the water temperature was measured with a thermometer.
The relative density was calculated using the equation (3):

$$\rho(s) = \frac{W(a)\cdot[\rho(l) - \rho(a)]}{\rho(w)\cdot[W(a) - W(l)]} + \rho(a) \qquad (3)$$

ρ (s) = density of the solid ($g \cdot cm^{-3}$)
ρ (l) = density of the liquid ($g \cdot cm^{-3}$)
ρ (a) = density of air ($g \cdot cm^{-3}$)
W(a) = Weight of the solid in air (g)
W (l) = Weight of the solid in liquid (g)
ρ (w) = density of the water ($g \cdot cm^{-3}$)

3.3.4 3–Point Bending Strength

3 - Point Bending Strength is the most widely used test to measure the uniaxial tensile strength of brittle materials ceramics [13].
It is a destructive testing method to determine the maximum bending strength of materials. The instrument used was MTS Electromechanical Universal Testing Systems (see Figure 14), equipped with a load cell with a maximum capacity of 1 kN; TestWorks 4 Software Training was used to analyze the results.
In line with the literature, rectangular test pieces were used because they are deemed better suited to this test.
The b×h cross-section specimen was placed centrally on two cylindrical supports at a distance l from each other and was subjected to a load at l/2, which moved perpendicular to the specimen at a speed defined by the operator.
At the loading point, the upper surface of the specimen is subjected to compression, while the lower surface is subjected to traction.
The test ends when the specimen breaks.
As an alternative to the 3-Point Bending Strength test, there is also the 4-Point Bending Strength test, where a double loading point is used.
The force measured at the moment when the test body breaks is called Ultimate Tensile Stress (UTS, σ) and is described by Navier's equation (4) [14]:

$$\sigma = \frac{3\,l}{2\,b\,h^2} F \qquad (4)$$

l = distance between the two cylindric supports (m)
b = section width of the bar (m)
h = section height of the bar (m)
F= force applied (N)

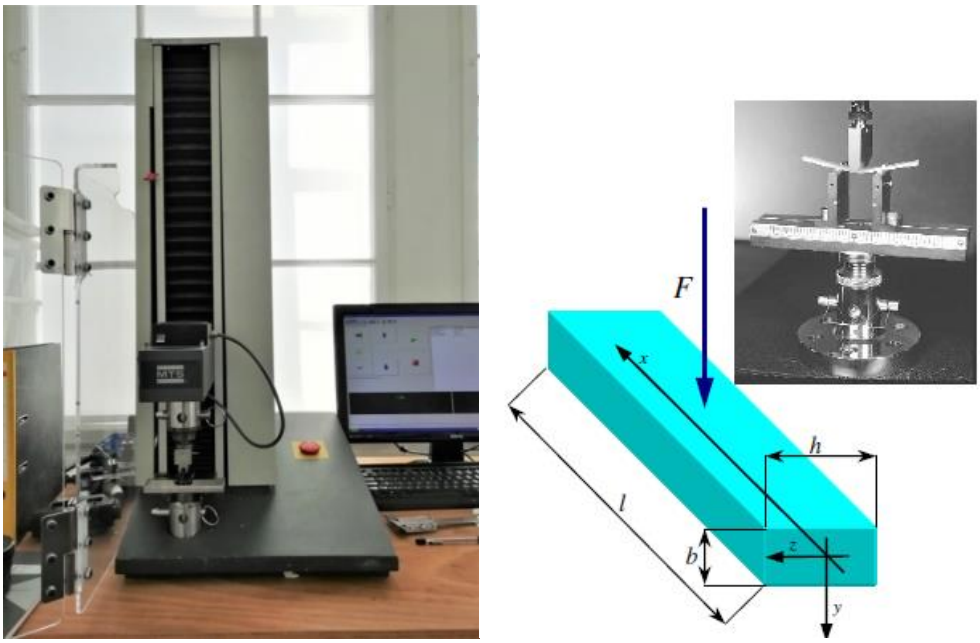

Figure 14. Equipment used and geometry of the sample.

3.3.5 Shrinkage Factor

Whenever the green bodies are sintered, there is a shrinkage of the structure caused by the evaporation of the binder and the densification of ceramic particles. It is necessary to calculate the shrinkage of the samples so as to obtain final scaffolds of the desired size

In order to evaluate the shrinkage factor, 18 LithaBone 480E bars were printed, all with the same size 2x2.5x2 mm (Figure 15 A)). Of these, 5 were chosen and were measured pre and post sintering along the three axes: X, Y, Z. (Figure 15 B)).

The shrinkage rate was calculated using the following equation (5):

$$\text{Shrinkage Factor (\%)} = \left(\frac{\text{Vb} - \text{Va}}{\text{Vb}}\right) * 100 \qquad (5)$$

V_b: volume before sintering

V_a: volume after sintering

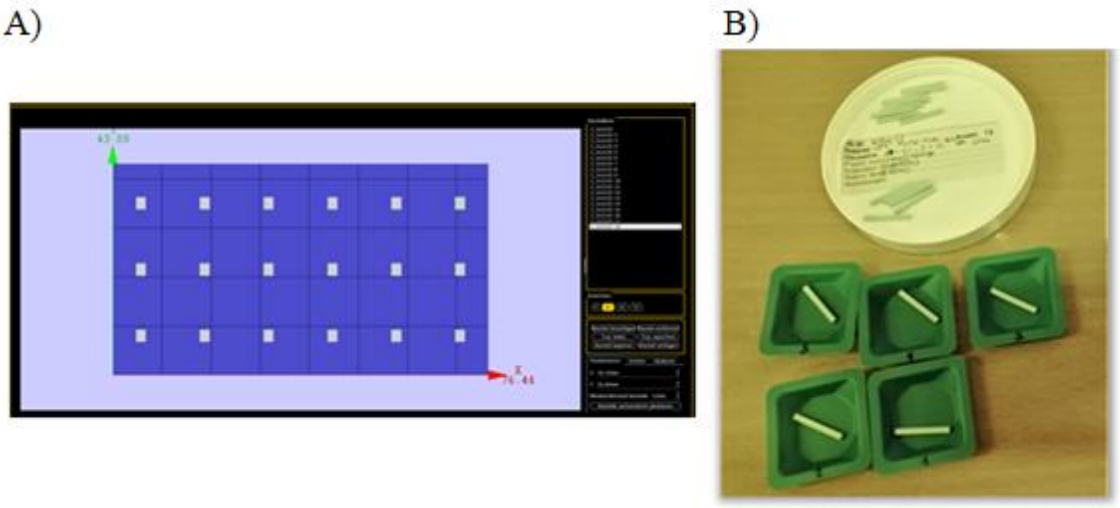

Figure 15. A) Fab –file; B) 5 out of 18 printed bars selected for the calculation of the shrinkage factor.

3.4 Design specifications for printing

In order to obtain a good final product, it is necessary to consider the properties of the slurry and the process parameters. Depending on the material, different results could be obtained with respect to the possibility of printing holes of a certain size or overhangs.
In order to discover strengths and weaknesses of the slurry, some additional tests were performed, as summarized in Table 3.

Table 3. Virtual Tray of fab-file for the LithaBone 480E.

1. Wall Thickness	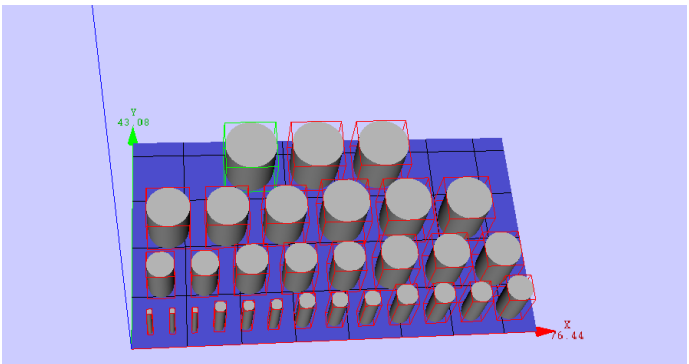
2. Aspect Ratio	

	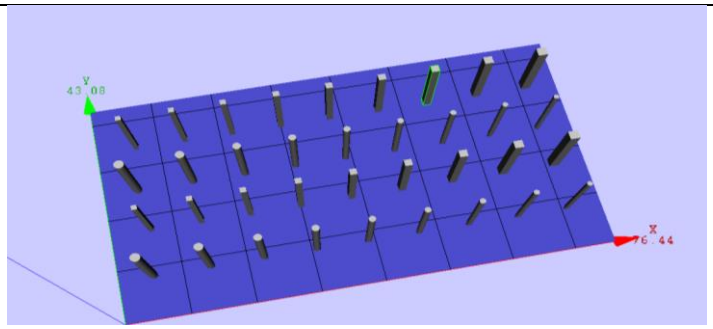
3. Overhangs	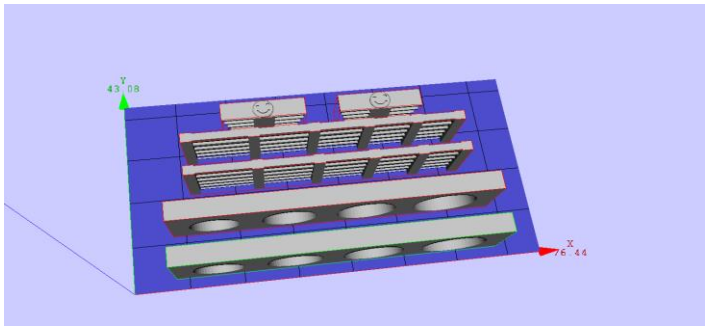
4. Minimal Feature and overpolymerization	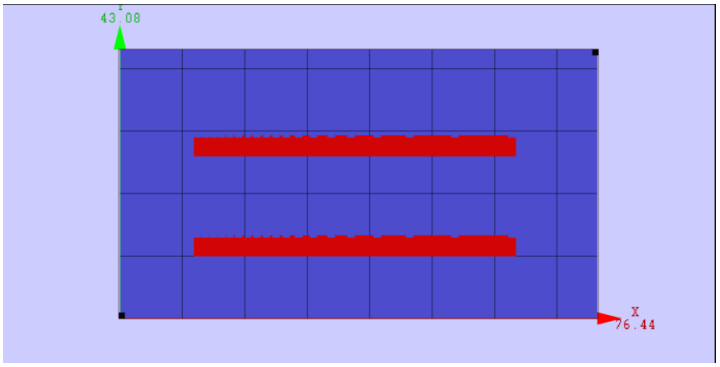

3.4.1 Wall Thickness

The term "wall thickness" literally means the distance between a surface and its opposite. Referring to porous scaffolds, the concept can be exemplified by taking an anatomical term and, by wall thickness, indicating the thickness of a single "trabecula".

This parameter is important to ensure that the final 3D trabecular structure is not formed by trabeculae that are too fragile and unsuitable for the printing parameters. Low wall thickness values (i.e. very thin trabeculae) can be obtained if the slurry has good stiffness properties; however, thin trabeculae are very fragile and could break during printing. In order to evaluate the wall thickness, cylinders with a height of 10 mm and diameter from 1 mm to 10 mm were produced.

The minimum wall thickness was evaluated by considering the non-sintered cylinder with the smallest printed diameter without defects, while the greatest diameter of the non-sintered sample

presenting no cracks after sintering was considered to calculate the maximum wall thickness. Cracks and other defects can often be due to a non-volatile binder which fails to evaporate completely, thus generating stress that could lead to breakage.

3.4.2 Aspect Ratio

The aspect ratio is the ratio between the height and the diameter of the sample in question. In order to evaluate the maximum aspect ratio, 18 square base bars and 18 cylindrical base bars were constructed, all with a height of 15 mm and a diameter/perimeter from a minimum of 0.833 mm to a maximum of 1.5 mm, and an aspect ratio from 2 to 18.

The samples were examined under an optical microscope before sintering to evaluate the presence of cracks on the surface.
In order to increase the visibility of any defects, the light was directed obliquely on the samples.
The maximum aspect ratio will be considered to be that for which the sample has no surface blur.

3.4.3 Overhangs

The purpose of this test was to evaluate the achievability and printing limitations of overhangs and pores.
Overhangs represent one of the most difficult challenges for SLA because their presence increases the risk of obtaining an unstructured final object.
Two types of overhangs were considered:

- **H-overhangs** (Figure 16): the achievability of printing overhangs connected to a supporting structure on both sides was evaluated. The various overhangs differed from each other both in length and thickness. In this case, printed and sintered samples were checked for fractures and conformity to the desired shape without any detachment from the vertical supporting structure.

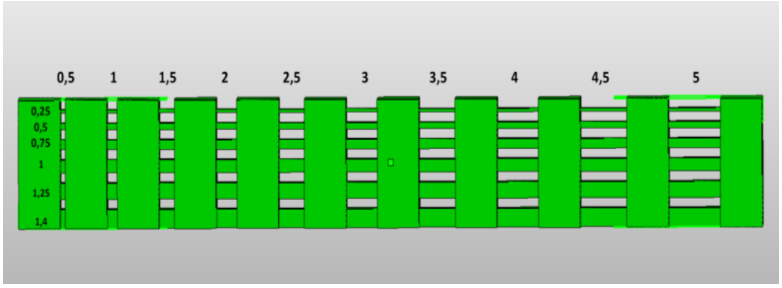

Figure 16. H-Design of overhangs. The numbers listed horizontally indicate the length of the different overhangs (in mm); the numbers listed vertically indicate their thickness (in mm).

- **T-overhangs** (Figure 17): these overhangs are only connected to the supporting structure on one side and therefore have a much higher probability than the H - overhangs of deforming and detaching during printing.
  In this case, the ability to maintain parallelism between the overhangs and the building platform was evaluated. If the speed of polymerization and the stiffness of the material is optimized, the overhangs will be printed correctly; otherwise, they may be structurally inaccurate, deformed (mainly at the outer end) and/or even broken.

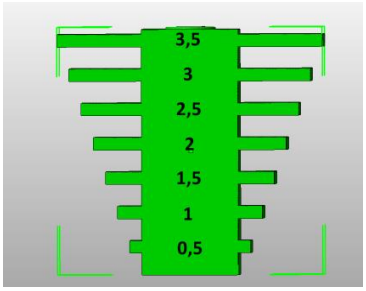

Figure 17. T – Overhangs Design.

- **Diameter** (Figure 18): it is often necessary to make porous scaffolds, especially when they are intended for use in BTE, as in this case. It is therefore essential to understand to what extent small or large pores with a certain diameter may be achieved.
  The purpose of this test was to ascertain whether it was possible to print the desired diameter with a precise circumference and no grooves. Obtaining holes with serrations is frequent when the diameters are relatively large, whereas small pores must be checked for occlusions.

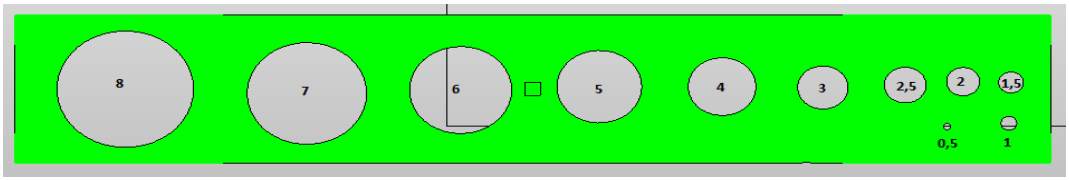

Figure 18. Diameter Design.

3.4.4 Minimal feature and overpolymerization

In order to check Minimal Wall Thickness, two identical test bases with many small protrusions of increasing width from left to right were printed.
The theoretical width of the pillars (µm) is given by the number of pixels (Figure 19) multiplied by the pixel size (machine dependent);
Given the fragility and the small size of the protrusions, the sample, once printed, is not detached from the building platform but cleaned directly above it and then evaluated under an optical microscope.

This test assesses:

- Material stiffness: Low stiffness values mean that smaller pillars are not printed correctly. The test is considered positive if all small protrusions adhere perfectly to the building platform and do not show any defects and/or deformations.

- Printing accuracy and overpolymerization: overpolymerization problems that may be due to an excessive amount of photoinitiator in the slurry formula or an overlong exposure to light. Pixel-dependent overpolarization values are calculated with respect to the width measured in μm. If possible, the width of the pillars is measured at different points of the central area.

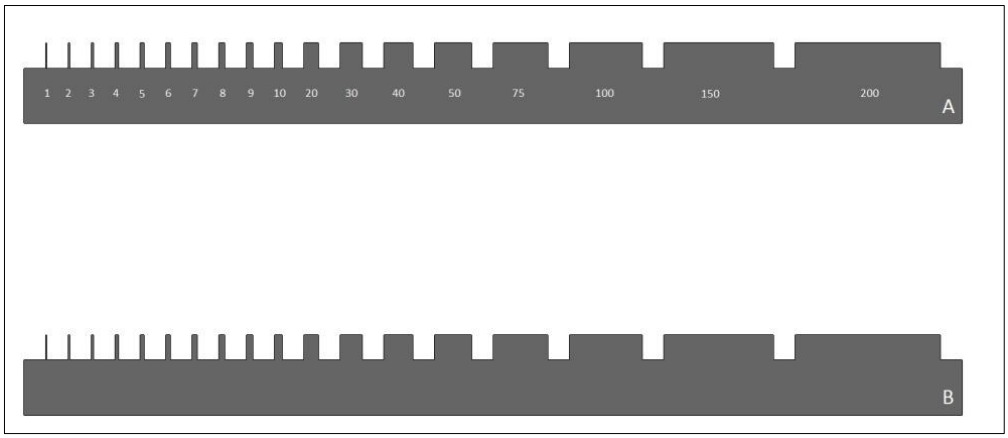

Figure 19 . Minimal features illustation (the numeration corresponds to the number of pixels).

3.5 Scaffold Design & Manufacturing

3.5.1 Solid Cylinders

Before printing the porous scaffolds obtained from 45 ppi commercial polymeric sponge µ-CTs images, LithaBone 480E slurry was used to print non-porous hollow cylinders with the same height and diameter as the one chosen for the porous cylinders (h 10 mm and d 5 mm), with aspect ratio of 2:1.
Three printing jobs were set up and, for each job, 45 cylinders were produced for a total of 135 cylinders.
The geometrical parameters of the 3 different sets of cylinders are:

1. Set of cylinders: 45 cylinders, h 10 mm d 5 mm; distance ext.-int. circumference = 1 mm
2. Set of cylinders: 45 cylinders, h 10 mm d 5 mm; distance ext.-int. circumference = 1.5 mm
3. Set of cylinders: 45 cylinders, h 10 mm d 5 mm; distance ext.-int. circumference = 2 mm (Figure 20).

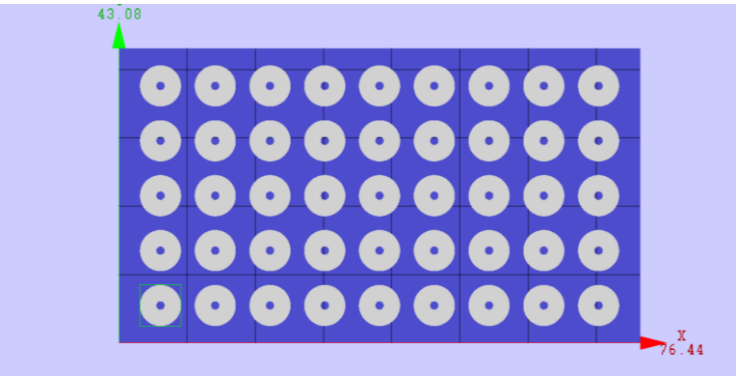

Figure 20. Virtual Tray of Fab-file, 3rd set of cylinders: 45 cylinders, h 10 mm d 5 mm; distance ext.-int. circumference = 2 mm.

3.5.2 From Cubic Porous Scaffolds to Cylindrical Porous Scaffolds

In order to obtain a 3D porous matrix closely resembling the architecture of spongy bone (cancellous bone), a CAD file created from 45 ppi commercial polymeric sponge µ-CT images was used. It is worth highlighting that this was the first time that µ-CT was coupled with DLP to produce bone-like bioceramic scaffolds in Lithoz.
The InVesalius software allowed us to reconstruct the 3D profile of the polymeric sponge starting from 771 two-dimensional BMP (.bmp) files, thus obtaining an almost cubic 3D scaffold (4.72 x 5.15 x 5 mm), with a porosity of 81.8%. (Figure 21. A)).

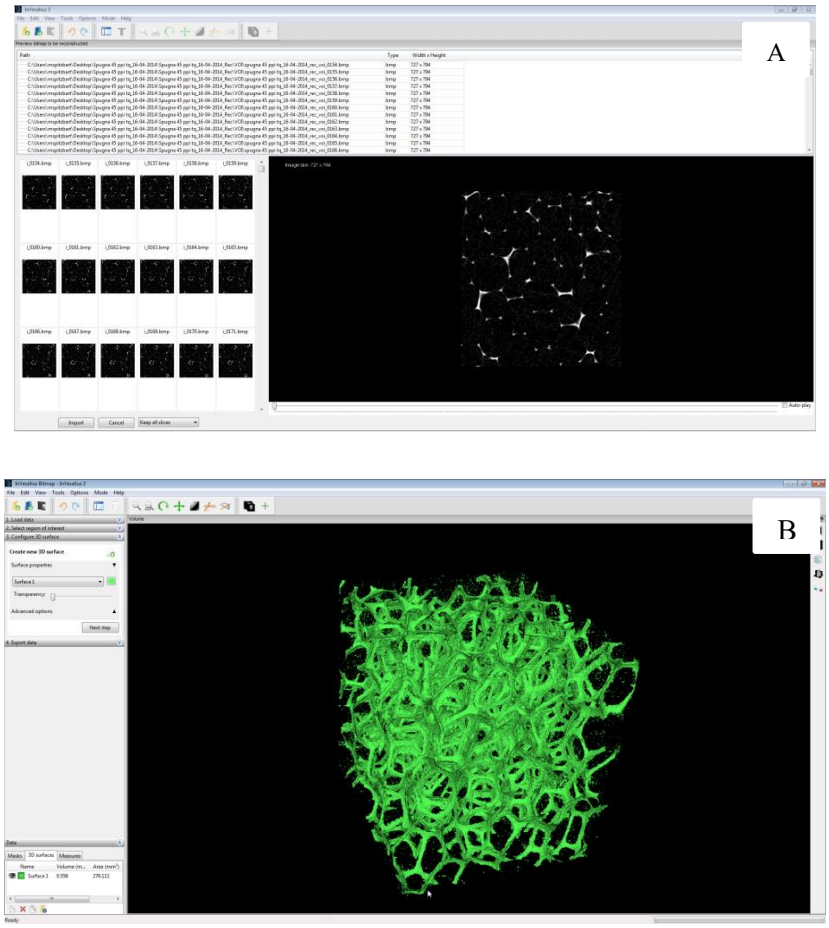

Figure 21. A) Selection and import of .bmp file; B) Reconstruction of the 3D architecture of cubic sponge .

InVesalius software is widely used in various fields of engineering, archaeology, industrial applications, as well as in medicine and dentistry, to assist physicians in diagnosis and subsequent surgical planning [15].
InVesalius imports files in DICOM (Digital Imaging Communication in Medicine) format, including NIfTI, PAR/REC, BMP, TIFF, JPEG and PNG formats [15], obtained from magnetic resonance imaging (MRI), computed tomography (CT), ultrasound, or electrocardiogram examinations.

In order to obtain scaffolds of the most suitable size and geometry for characterization tests required in BTE, it was decided to build them in a cylindrical shape and aspect ratio 2:1, as recommended by the literature. This was possible by superimposing longitudinally on the primordial cubic structure (Figure 21. B)) its exact and overturned copy.
Moreover, in order to obtain a cylinder, the circle inscribed on the square base was considered.
The final dimensions were 5x5x10 mm, with a porosity slightly greater than the previous one, of about 83.4%.
In order to obtain scaffolds which were printable and not too fragile, due to the high porosity and thin trabeculae, the thickness of the structure was increased by 25% in both cases.

The main steps for obtaining cylindrical scaffolds from cubic scaffolds are shown in Figure 22 The precise parameters of two scaffolds are listed in Table 4.

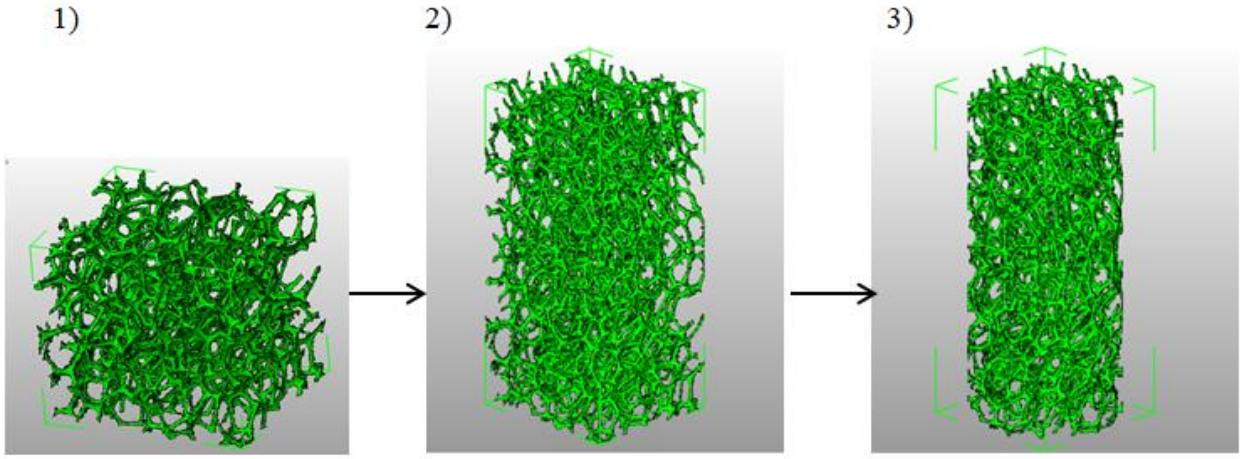

Figure 22. STLs files visualized in Autodesk Netfabb Premium 2019. 1) cubic sponge; 2) Doubled Cubic sponge; 3) Cylindric sponge with aspect ratio 2:1 .

Table 4. Parameters of the STLs of created geometries.

Parameters	**Cubic Sponge**	**Cylindrical Sponge**
Length (mm)	4.72	5.0
Width (mm)	5.15	5.0
Height (mm)	5.0	10
Contouring offset (µm)	+ 25	+ 25
% Porosity	81.8	83.4

The setup is a DLP system with a bound surface that uses a LED radiation source in the blue visible region. Before printing, the surface of the building platform was coated with a special foil provided by Lithoz to increase adhesion between the building platform and the first layer created.
The most important parameters are summarized in Table 5. The first 5 layers utilize different parameters from all the others, in order to avoid the formation of air bubbles and improve the adhesion of the layers with the building platform.
Figure 23 shows fab-file created with Cerafab (DP) for cubic porous scaffolds and fab-file for cylindrical porous scaffolds.

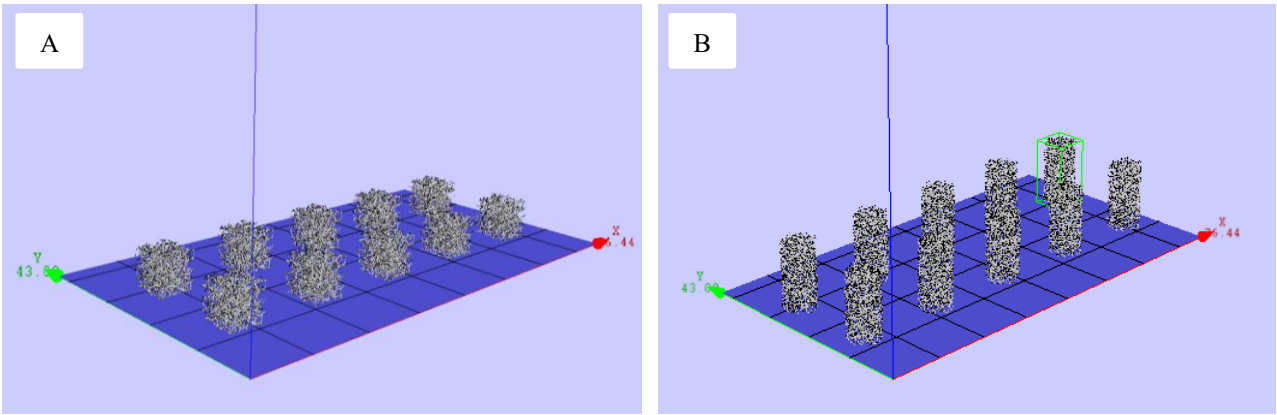

Figure 23. A) Virtual Tray of fab-file for porous cubic scaffolds; B) Virtual Tray of Fab –file for porous cylinder scaffolds (For greater clarity, only 10 of the 18 shelves actually present in the image are displayed).

For each print job 10 cubic scaffolds were manufactured simultaneously for a total of 30 scaffolds. 18 cylindrical scaffolds were created during each print job for a total of 90 scaffolds.

Table 5. Parameters for the manufacture of the cubic and cylindrical scaffolds.

Parameters	**Value**
Pixel size	40 µm
Layer height	25 µm
Slurry height	175 µm
Shrinkage compensation factor (xy)	1.206
Shrinkage compensation factor (z)	1.25
Contour offset	25 µm
Ambient Temperature	25 °C
Number of starting layers	5
Back light exposure	1.400 s
DLP energy start	100 mJ / cm^2
DLP energy general	90 mJ / cm^2
Exposure time starting layers	1.894 s
Exposure time main layers	1.769 s
Expsure intensity starting layers	79.200 mW/ cm^2
Exposure intensity main layers	79.200 mW/ cm^2
Exposure energy starting layers	150.005 mJ/ cm^2
Exposure energy main layers	140.105 mJ/ cm^2

3.6 Analysis of Manufactured scaffolds

3.6.1 X-Ray Diffraction (XRD)

The X - Ray Diffraction (XRD) analysis is an analytical method for the study of the chemical composition and the crystalline phases within a solid sample. .
This test method is based on constructive interference between monochromatic X-rays and the powder or bulk sample.
X-rays are highly penetrating electromagnetic waves characterised by a wavelength (λ) between 10 nm and 0,01 nm [16].
In 1912, Max von Laue discovered that crystalline substances act as 3D diffraction gratings for X-ray wavelengths [17] and that the resulting diffraction spectrum contains fundamental information on the distribution of atoms, since the wavelength (about 1Å) of X-rays is comparable to the interatomic distance [16].
When an X-ray beam hits a solid material with a crystalline structure (i.e. formed by atoms ordered according to a lattice), it causes the vibration of the electrons surrounding a single atom and starts emitting electromagnetic radiation of wavelength λ in all directions.
Diffuse waves can interfere both constructively and destructively; if X-rays are reflected by a family of parallel and equidistant reticular atomic planes (d) and the optical path difference of the radiation between adjacent crystalline planes is equal to an integer number of wavelengths, then the interference is constructive and can be described by Bragg's law (Equation 5) [16]:

$$n\lambda = 2d \sin \theta \qquad (5)$$

λ= radiation wavelength
θ = of X-ray incidence
d = interplanar distance (distance between parallel crystalline planes).
n = whole number indicating the order of reflection

Bragg's law allows us to univocally identify the mineral phase of the sample and determine the size d.
When the X-rays reach the surface of the sample, they are processed and counted to produce a diffraction spectrum according to position 2θ.
Since each material has a unique set of d-spaces, the conversion of diffraction peaks into d-spaces allows the identification of the material [17].
Generally, d-spaces are compared with standard reference models.
The devices used to determine the diffraction spectrum and then analyze the crystalline structures of the materials are called X-ray diffractometers.
The X-ray diffractometer consists of 3 main components:

1. **Cathode Ray Tube**: heats a filament to produce electrons. By applying an appropriate voltage, the electrons are accelerated towards a target and bombard it. When the electrons

reach sufficient energy to remove the electrons from the target's inner shell, characteristic X-ray spectra are produced [17].

2. **Sample holder** : container in which a thin, homogeneous layer of sample powder is placed [17].

3. **X-ray detector** : records and processes the signal produced by constructive interference [17].

The diffractometers may have different geometries according to the relative position between detector, source and sample; the most common is that of Bragg-Brentano in which detector and source rotate simultaneously around the stationary sample (Figure 24) [16].

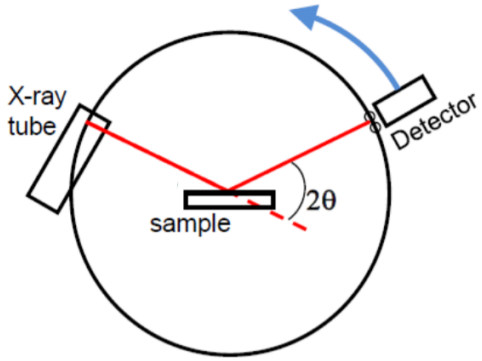

Figure 24. Schematization of Bragg – Brentano diffractometer.

The XRD analysis was performed on LithaBone 480E powder using a PANalytic diffractometer with Bragg-Brentano chamber. The XRD spectra were analysed using XPert - Pro, a data analysis software which compares the spectrum of unknown material with standards contained in a database. The operating conditions are shown in Table 6.

Table 6. Operating conditions for XRD tests.

Anod material	Cu
Generator Voltage	40 kV
Tube Current	40 mA
2θ range	10° - 70°
Wavelength (λ)	0.15 nm

3.6.2 Scanning Electron Microscopy (SEM) and Energy Dispersive Spectroscopy (EDS)

The scanning electron microscope (SEM) connected to an energy-dispersive microanalytical system (EDS) is an easy and versatile analysis method for the analysis of the morphology and composition of the sample [18].
Unlike the optical microscope, SEM uses high speed electrons as a radiation source. The electrons, having a much shorter wavelength than photons, reach far better resolution levels than those achievable with an optical microscope [18].
The signals produced by the electrons impacting on the samples are made up of secondary electrons, which are captured by a detector and converted into electrical signals, backscattered electrons (useful for EDS) and diffracted backscattered electrons and photons.
Generally, secondary electrons are used to produce SEM images and obtain morphological information [19].
A classical SEM microscope allows us to analyze a surface area of the sample ranging from 1 cm to 5 μm wide, with a magnification ranging from 20X to about 30,000X and a spatial resolution in the range of 50 - 100 nm.
The main components of a SEM microscope are (Figure 25):

1. Data output devices / TV scanner
2. Detectors for signals of interest
3. Stage
4. Electron Source (“Gun”)
5. Electron Beam
6. Infrastructure Requirements (Vacuum System, Cooling System, Vibration – free floor, Room free of ambient magnetic and electric fields)

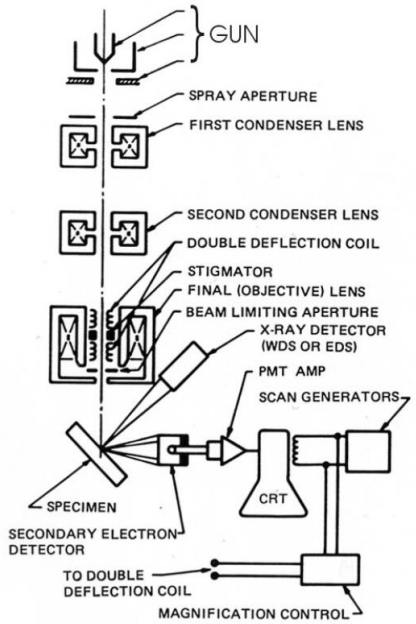

Figure 25. Schematic SEM representation [19].

The samples must be in a solid state and of such a size as to fit the microscope chamber. Electrically insulating samples have to be coated with a thin layer of conductive material (e.g. carbon, gold, chromium or other metals) [19]. Making the surface of the sample conductive will avoid creating a very disturbed image [20].
The SEM analysis is "non-destructive", i.e. the characteristics of the sample are not altered during the test and therefore the test can be repeated several times [19].
EDS therefore allows us to obtain compositional, chemical and structural information of the sample [18].
The elemental microanalysis SEM-EDS allows us to obtain both a qualitative analysis of the sample composition, either over a wide area or by focusing the scanning of the electron beam at a specific point [22], and a semi-quantitative analysis of the elemental composition of the sample and a mapping of the distribution of the elements detectable in the sample [19].
Thanks to EDS spectrometers, it is simple to quickly acquire the complete emission spectrum and identify the different elements that make up the sample and their proportions [18].

The samples analyzed were attached to SEM metallic stabs using a conductive glue. Samples were prepared under a hood due to the toxic potential of the glue. The samples had to be sputter-coated with a thin layer of chromium (~10 nm) in order to make them electrically conductive, which is necessary to high-quality SEM-EDS analyses (Figure 26).

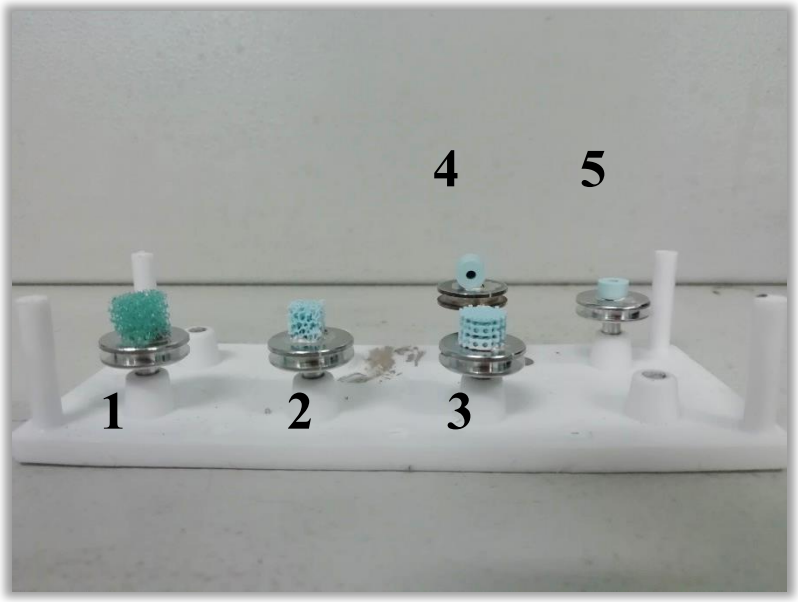

1. Commercial Sponge 45 ppi
2. Cubic Sponge
3. Stability Tray cylinder
4. Broken Cylinder
5. Fracture surface

Figure 26. Samples for SEM and EDS analysis.

Using the Benchtop SEM microscope (JCM - 6000Plus Versatile Benchtop SEM JEOL) (Figure 27) 5 different samples were subjected to morphological analysis and compositional characterization.

Figure 27. Benchtop SEM (JCM – 6000Plus Versatile Benchtop SEM JEOL) used for morphological analysis and compositional characterization of scaffolds.

References

[1] A. R. L. Francisco, “User guide CeraFab 7500,” J. Chem. Inf. Model., vol. 53, no. 9, pp. 1689–1699, 2013.

[2] A. D. Lantada, A. De Blas Romero, M. Schwentenwein, C. Jellinek, and J. Homa, “Lithography-based ceramic manufacture (LCM) of auxetic structures: Present capabilities and challenges,” Smart Mater. Struct., vol. 25, no. 5, 2016.

[3] I. Potestio, “Lithoz: How lithography-based ceramic AM is expanding the opportunities for technical ceramics,” Powder Inject. Mould. Int., vol. 13, no. 2, pp. 2–5, 2019.

[4] Z. Liu et al., “Additive manufacturing of hydroxyapatite bone scaffolds via digital light processing and in vitro compatibility,” Ceram. Int., vol. 45, no. 8, pp. 11079–11086, 2019.

[5] “Viscosità - Wikipedia.” [Online]. Available: https://it.wikipedia.org/wiki/Viscosità. [Accessed: 25-Apr-2020].

[6] “What is the difference between shear thinning and shear thickening and newtonian fluid? - Quora.” [Online]. Available: https://www.quora.com/What-is-the-difference-between-shear-thinning-and-shear-thickening-and-newtonian-fluid. [Accessed: 27-Apr-2020].

[7] “Rheological measurements :: Anton Paar Wiki.” [Online]. Available: https://wiki.anton-paar.com/it-it/fondamenti-della-reologia/misura-con-reometro/. [Accessed: 27-Apr-2020].

[8] Galvan, F. R., V. Barranco, J. C. Galvan, S. Batlle, Sebastian FeliuFajardo, and García, “Polymeric Additive Manufacturing: The Necessity and Utility of Rheology,” Intech, vol. i, p. 13, 2016.

[9] N. Standard and L. Byk-gardner, “Grindometri,” pp. 181–182.

[10] P. Description, “Grindometers,” pp. 1–2.

[11] “Grindometer - Wikipedia.” [Online]. Available: https://en.wikipedia.org/wiki/Grindometer. [Accessed: 08-May-2020].

[12] “Principio di Archimede - Wikipedia.” [Online]. Available: https://it.wikipedia.org/wiki/Principio_di_Archimede. [Accessed: 27-Apr-2020].

[13] M. R. Mitchell et al., “Flexural Strength of Ceramic and Glass Rods,” J. Test. Eval., vol. 37, no. 3, p. 101649, 2009.

[14] G.Petrucci, “‘Lezioni di Costruzione di Macchine’: Proprietà Dei Materiali E Prove Meccaniche.” pp. 1–18.

[15] P. Junqueira et al., “InVesalius User Guide,” p. 130, 2007.

[16] D. N. G. Mormone A., Piochi M., “Rapporti Tecnici: Identificazione e stima quantitativa delle fasi in campioni polverizzati.,” Issn, vol. 279, pp. 1–20, 2014.

[17] “Diffrazione di raggi X in polvere (XRD).” [Online]. Available: https://serc.carleton.edu/research_education/geochemsheets/techniques/XRD.html. [Accessed: 28-Apr-2020].

[18] L. Miraglia, “Caratteristiche del sistema analitico SEM-EDS valutazione dell’accuratezza e della precisione delle analisi eseguite su standard internazionali di minerali e vetri,” Rapp. Tec. INGV, vol. ISSN 2039, no. 233, pp. 1–20, 2012.

[19] “Microscopia elettronica a scansione (SEM).” [Online]. Available: https://serc.carleton.edu/research_education/geochemsheets/techniques/SEM.html. [Accessed: 28-Apr-2020].

[20] M. Ottica, “Slides ‘La cristallografia Analisi Strutturali.’” .

[21] “Come funziona l’analisi EDX nel microscopio elettronico a scansione(SEM) | Microscopia Elettronica da banco.” [Online]. Available: http://www.microscopiaelettronicadabanco.it/analisi-edx-nel-microscopio-sem. [Accessed: 29-May-2020].
[22] “Microanalisi EDS.” [Online]. Available: https://www.tec-eurolab.com/eu-it/microanalisi-eds.aspx. [Accessed: 29-Apr-2020].
[23] Lithoz GmbH, “Lithoz Available Materials.”, 2019, pp.1-9, 2019.

Chapter 4

Results and discussion

The objective of this thesis project was the realization of highly reproducible HA-porous scaffolds, for the regeneration of cancellous bone by applying a new approach based on a combination between tomographic imaging and additive manufacturing.
Specifically, μ-CTs images of commercial polyurethane sponges were used as trabecular model in combination with Digital Light Processing technology to ensure high standardization and quality of the manufacturing process while remaining faithful to the natural trabecular architecture of the biological tissue.
The porous scaffolds, originally produced in cubic shape and subsequently as cylinders, were designed and printed at Lithoz GmbH (Vienna) using their ceramic manufacturing system; they then underwent morphological and chemical characterization at the DISAT laboratory of the Politecnico di Torino (Turin, Italy).

4.1 Printing and sintering of ceramic components

CeraFab 7500 machine, developed by Lithoz GmbH, was used to realize a total of 120 highly porous scaffolds which respected the particular architecture of the original CAD model.
As explained in the previous chapters, CeraFab machines are based on DLP- based SLA. Compared to classic SLA, where point-by-point scanning of the cross-section of each layer takes time, the DLP device exposes the entire layer to selective light exposure, drastically reducing production time without sacrificing resolution.
While working at Lithoz, many efforts were made to optimize the printing parameters and investigate the properties and limitations of the new LithaBone 480E photocurable slurry in order to achieve an intelligent and marketable solution for bone defect regeneration.
As explained in *Chapter 2*, SLA printed ceramic materials need to be treated at high temperature in order to remove the binder and sinter the inorganic particles.
After printing, remnants of uncured slurry were removed from the green bodies by applying compressed air and using a cleaning agent provided by Lithoz.
Especially for porous scaffolds, this procedure required a great deal of care, due to the extreme fragility of the structure.
The cleaning of the ceramic parts may affect the properties of the final product; in fact, the use of compressed air and the mechanical rubbing treatment to remove the uncured slurry may subject the

green bodies to stresses, thus affecting the sintering outcome and the properties of the final product [1].
Both the evaporation of the organic matrix and the sintering of the green bodies were carried out in a Nabertherm P330 furnace for 99 hours at a variable temperature speed between 0.42 and -1.62 K/min. The maximum sintering temperature of 1300 °C was maintained for 2 hours.
The green bodies, initially grey-white in colour, changed colour to light blue after sintering likely due to the presence of manganese (Mg) traces inside the HA powder.
Y. Li et al., noted that HA containing manganese changes its color to blue after sintering at high temperature in oxidizing atmosphere as a result of the oxidation of manganese ions within the crystalline structure of HA [2].
In addition, several types of samples produced, including non-porous cylindrical scaffolds, showed surface cracks after sintering.
The presence of cracks on sintered ceramic structures is not uncommon; this can be caused by a poorly volatile binder whose formula still needs to be refined, but also by heat treatment, maybe too fast, or by certain manufacturing parameters used [3].
The cleaning agent used to clean the scaffold surface from excess slurry can also contribute to the formation of these defects [1]; it would therefore be preferable to avoid excessive use of these agents, which could lead to the structure swelling and consequent residual internal stresses.
Moreover, the images shown in Figure 1 show that all the fractures which formed were parallel to the building platform, and therefore in the same direction as the construction of the layers; this could mean that the adhesion between the individual layers may not be sufficient to withstand the stresses to which the sample is subjected during the thermal process.
In addition, it is worth mentioning that as the thickness of the samples increases, the mass transport phenomena become more limited, leading to the consequent accumulation of solvents and/or products of degradation; this causes an inevitable increase in pressure which may cause cracks in the artefact [4].

Figure 1. Examples of surface cracks in sintered samples of different geometry.

Table 1 summarises the main print jobs carried out at Lithoz GmbH.

Table 1. Overview of main print jobs carried out at Lithoz GmbH with LithaBone 480 E slurry and CeraFab 7500 machine.

JOB ID	Starting Data	N. of layers for sample	N. of samples	Working time (h)
Testing Bars for shrinkage Factor	30.10.2019	1251	18	17.00
Overhangs	31.10.2019	600	6	8.00
Stability Tray 1° week	05.11.2019	250	13	3.28
Aspect Ratio	06.11.2019	600	36	8.00
Wallthickness	07.11.2019	400	30	5.45
Stability Tray 2° week	11.11.2019	250	13	3.28
Minimal Feature and overpolymerization	12.11.2019	40	2	0.39
Cubic Sponges	13.11.2019	250	10	3.42
Cubic Sponges	13.11.2019	250	10	3.42
Cubic Sponges	14.11.2019	250	10	3.42
Stability Tray 3° week	18.11.2019	250	13	3.28
Cylinders_set 1	18.11.2019	500	45	6.49
Cylinders_set 2	19.11.2019	500	45	6.49
Cylinder Sponges	19.11.2019	500	18	7.06
Cylinder Sponges	20.11.2019	500	18	7.06
Cylinder Sponges	20.11.2019	500	18	7.06
Cylinder Sponges	21.11.2019	500	18	7.06
Cylinders_set 3	21.11.2019	500	45	6.49
Stability Tray 4° week	25.11.2019	250	13	3.28
Cylinder Sponges	25.11.2019	500	18	7.06
Stability Tray 5° week	02.12.2019	250	13	3.28

4.2. LithaBone 480E- Slurry Characterization

LithaBone 480E, provided by Lithoz, was produced using commercial HA powder homogeneously mixed with a photocurable organic binder system.
The HA powder, previously used by Lithoz for the creation of the LithaBone 400 slurry, had a purity above 95%, a theoretical density of 3.156 g/ cm^3 and complies with the specification for hydroxyapatite as an implant material, according to the ASTM F1085 - 03 [5].

A 5-week "Stability tray test" job was set up during which the rheological properties of the uncured slurry, maximum grind size, its relative density and the ultimate tensile strength were studied. Moreover, the possibility of printing different geometries with interconnected and controlled pore size was investigated.
Samples needed for the density measurement and the 3-point bending strength test were printed using the preset "stability tray" fab-file. The "Stability tray" required the production of 7 bars with dimensions of 2×2.5×25 mm to perform the 3-point bending strength test; 4 cubic samples for the relative density test and 2 cylinders with ordered porous architecture, all depicted in Figure 2.

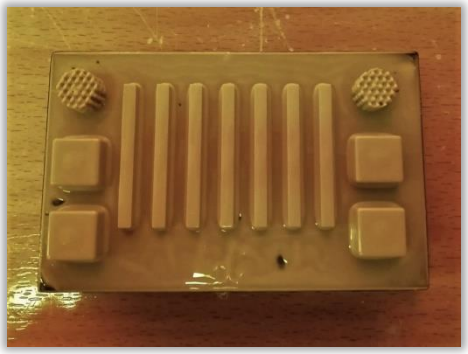

Figure 2. “Stability tray” samples, newly printed and still on the building platform.

After sintering, both the bars and the cuboids presented surface cracks (see Figure 1); since the cubes were particularly defective, it was decided to use the compact bars for both for the density test and the 3-point bending strength test.

4.2.1 Viscosity Test

Low viscosity and stable rheological behaviour are very important requirements for DLP materials [1]; an inadequate slurry viscosity may lead to problems during printing , thus affecting the properties of the final structure [6].

The rheological behaviour of LithaBone 480E slurry was investigated by an RCM Rotational Rheometer, setting a constant shear rate $\dot{\Upsilon} = 50\ s^{-1}$ and a rotation time of 08"40"'.
The viscosity was measured at T= 25°C and T= 40°C in order to evaluate the viscosity decrease as the temperature increases.
The results obtained are illustrated in Table 2.

Table 2. Viscosity results at T=25°C and T=40°C.

	η (Pa·s)	
	T= 25°C	**T= 40°C**
Week 1	12.45	6.51
Week 2	13.44	7.79
Week 3	-	7.98
Week 4	13.37	8.21
Week 5	13.87	7.79

An average viscosity was recorded equal to **13.3 Pa·s** and **7.7 Pa·s** with **T=25 °C** and **T=40 °C**, respectively.

As an example, Figure 3 shows graphs obtained from the first rheological test performed using non-light cured slurry.

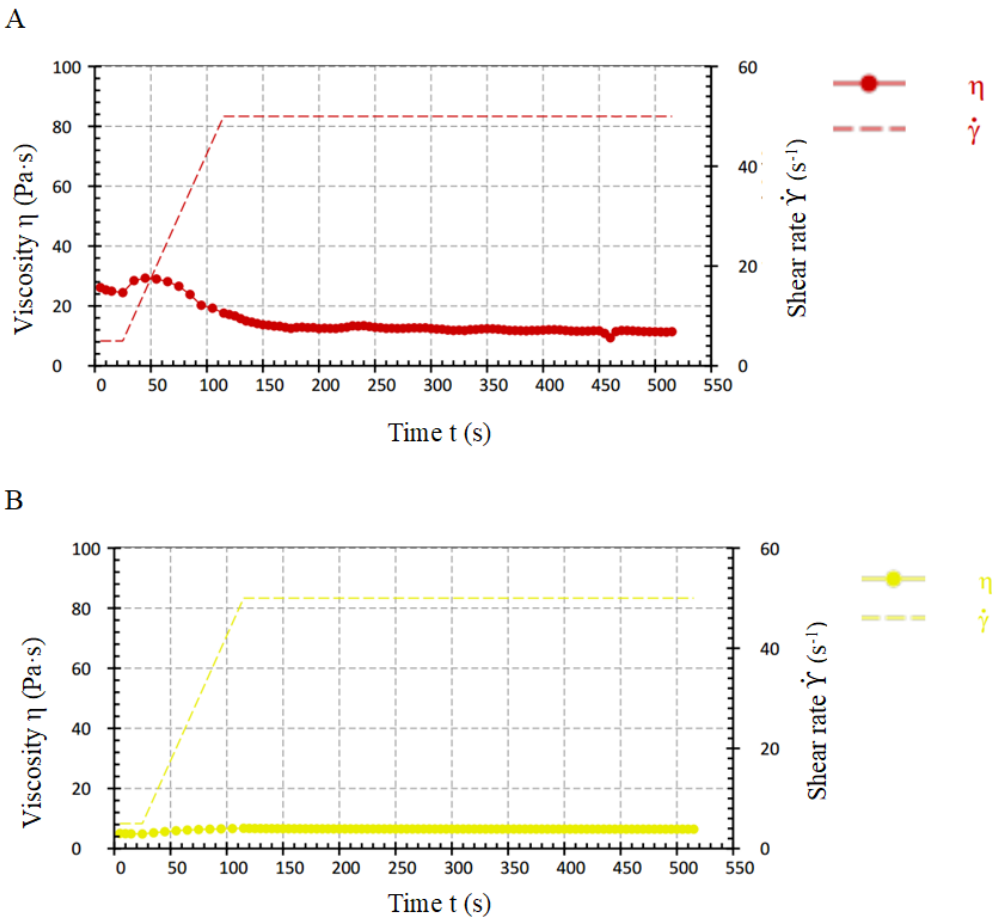

Figure 3. Graph illustrating LithaBone 480E slurry viscosity vs time "Stability Tray - 1st week" A) T= 25°C; B) T=40 °C.

As expected, the graphs above show that, by increasing the temperature, viscosity values decrease; moreover, for T=40 °C (Figure 2.B)), a constant trend of the curve was observed for the whole rotation time, while, for T=25 °C (Figure 2.A)), the curve initially presents higher viscosity values that decrease as the shear rate increases, highlighting a pseudoplastic (shear thinning behaviour) of the slurry.
The viscosity of LithaBone 480E slurry is similar to the viscosity of other materials developed by Lithoz adapted to be used with DLP process. In particular, LithaBone 480E viscosity is comparable to the viscosity of LithaBone 400 (η= 6.0-12.0 Pa·s for T=20°C and a shear rate of 50 s^{-1}) [5]. This fact, together with other data found in the literature [7]confirms that LithaBone 480E slurry is suitable to be used for DLP printing.
In other studies, lower viscosity values were obtained (around 3.0 Pa·s) but a shear rate of 100 s^{-1} was applied [8].
Comparing the values reported in Table 2, it is evident that the viscosity of the material remained approximately constant upon the whole duration of the stability test (5 weeks).
Temporal stability and low slurry viscosity ensure better chances of obtaining satisfactory printing results.
In order to facilitate and optimize the printing process, it is also important for the slurry not to be too viscous , otherwise the production of complex geometries may be difficult to achieve [1].
In fact, the probability of obtaining defective scaffolds increases as the slurry viscosity increases [1].
If the viscosity had been too high, it would have been necessary to change the initial slurry formula by changing the ratio of the organic part to ceramic particles.
Another common problem concerns the formation of clots: HA powders, indeed, have a high surface energy and tend to easily agglomerate to form larger particles.
However, it is possible to control this effect by increasing the concentration of dispersant, because the liquid phase tends to keep the particles at a distance, improving the fluidity of the slurry and decreasing its viscosity; at the same time, the ratio between powder and binder cannot be excessively reduced in order not to affect the mechanical properties of the final product [9]; moreover, if the viscosity is too low, it would be almost impossible to print in a controlled way because of the wetting properties of the fluid [1].
In order to obtain satisfactory printing results and adjust the low viscosity with the rheological behaviour - shear thinning, a compromise is required as it is thus fundamental to appropriately combine the photosensitive organic components with the powder content [1].

4.2.2 Grindometer Test

By using a grindometer we investigated the presence of agglomerates in the dispersion and their average size in order to estimate the degree of dispersion of ceramic particles inside the binder and their behaviour over time; sometimes, the finely dispersed powders in the organic matrix agglomerate over time and negatively affect the viscosity of the slurry; in fact, even the solid content of the slurry may have an impact on the rheological behaviour of the suspension [1].

Tendency to particle agglomeration was monitored over a 5 week period: the stability test showed that the LithaBone 480E slurry was stable, with minimal tendency to form clots and agglomerates. In particular, the size of larger particle agglomerates was around **6 µm**.

4.2.3 Archimedean Density

Using the Archimedes method, the density of LithaBone 480E samples was measured using sintered bars whose dimensions were 2 x 2.5 x 25 mm, printed using "stability tray" fab-file. These samples, like the cuboids that originally meant to be used, also had cracks and small surface defects.The results obtained from the 5 tests are summarized in Table 3. The test was performed by immersing the samples into distilled water at 24 °C and the temperature was measured each time by mean of a thermometer.

Table 3. Results of the Relative Density Test obtained using the Archimedes method.

Job ID	ρ_r 1 ($g \cdot cm^{-3}$)	ρ_r 2 ($g \cdot cm^{-3}$)	ρ_r 3 ($g \cdot cm^{-3}$)	Avg Density (ρ_r) %	Std Dev
Stability Tray 1° week	89.53	89.59	89.29	**89.47**	0.16
Stability Tray 2° week	90.74	90.86	91.08	**90.89**	0.17
Stability Tray 3° week	88.23	87.28	88.10	**87.87**	0.52
Stability Tray 4° week	86.50	86.34	86.69	**86.51**	0.13
Stability Tray 5° week	85.92	85.6	85.44	**85.65**	0.24

LithaBone 480E has an average relative density equal to $\rho_r = 88 \pm 0.61$ % and **porosity = 12 %.**

If we compare this result with other examples of relative slurry density for DLP, we will notice that the density obtained in the present work is lower than typical values reported in the literature; generally, in fact, density values measured with the Archimedes method are reported to be higher than 93% and there is a very low percentage of porosity due to interstitial microporosity [6], [9]. This may be due to the presence of surface microcracks on the test samples, that inevitably decreased the density of the material.
It is essential to obtain high density values to ensure the mechanical integrity of the scaffolds. Especially for ceramics, high density can be related to a low number of defects in the microstructure, which increas the strength of the material [10].

4.2.4 3-Point Bending Strength

Table 4 shows the results obtained during the 3-point bending strength test.
The 7 bars printed each week with "Stability tray" fab-file were used as samples.
Due to surface defects in the bars, the 5 measurements showed widely varying average figures. Surface cracks appeared after sintering, and this did not allow effective and comparable test results to be obtained; in fact, it was reported that test results are greatly influenced by the surface conditions of the sample, its density and grain size [8].

Table 4. Data obtained from 3-point bending strength using sample bars.

JOB ID	σ 1 (MPa)	σ 2 (MPa)	σ 3 (MPa)	σ 4 (MPa)	σ 5 (MPa)	σ 6 (MPa)	σ 7 (MPa)	Avg σ (MPa)	Std Dev
Stability Tray 1° week	62.8	76.5	80.3	68.3	84	80.4	75.4	**76.2**	4.9
Stability Tray 2° week	41.9	46.2	47.4	41.4	40.8	39.2	44.2	**42.9**	2.2
Stability Tray 3° week	64.6	51.9	52.9	71.8	56.9	62.8	44.7	**57.8**	5.7
Stability Tray 4° week	64.2	69.5	59.2	40.7	76.7	63.7	61.7	**63.7**	3.8
Stability Tray 5° week	54.4	74.9	54.6	75.3	59.3	76.4	40.4	**63.7**	10.6

An average Ultimate Tensile Strength (UTS) was obtained from the 5 measurements equal to **60.86 ± 5.4 MPa**

It is reasonable to attribute the large-scale variations between the different measurements to the presence or absence of cracks on the samples. In addition, the mechanical properties of synthetic HA, like almost all ceramics, largely depend on the type of processing performed, granulometry values, and the distribution and size of the micropores [11], making it difficult to directly compare this result with other examples in the literature.Table 5 summarizes the results obtained from the study performed on LithaBone 480E slurry.

Table 5. Technical Data for LithaBone 480E.

Powder	
Purity (%)	≥ 95
Complies with the specification for hydroxyapatite as implant material (ASTM F1085 - 03)	Yes
Slurry	
Viscosity [1] (Pa·s)	7.7 – 13.3
Max. Grind size (µm)	6
Sintered ceramic	
Theoretical density (g/cm³)	3.16
Relative density (%)	88
Porosity (%)	12
Colour	light blue
Three-point bending strength (MPa)	60.86

[1] Value was determined at a constant shear-rate of 50 s^{-1} at 40°C and 25°C, respectively.

4.2.5 Printing Feasibility Test for Porous Architectures.

Two cylinders of diameter d = 8 mm and height h = 6 mm were printed in order to check the feasibility of printing porous architectures with a controlled and ordered macropore geometry.
In order to do this, it was necessary to optimize both printing parameters and slurry composition, as discussed in the previous sections. The structure was free of defects and even after sintering, surface cracks did not appear as they did on the other samples (Figure 4), thus indicating the suitability of both LithaBone 480E slurry and printing settings.
Optical microscope and SEM analyses confirmed the success of the print: in fact, no pores were occluded and there were no defects along the circumference.
After sintering, pores became smaller due to the material shrinkage upon thermal treatment: the initial pore diameter, indeed, was around 750 µm, compared to the 600-650 µm pores observed in the sintered structure.
The geometry of the pores is perfectly hexagonal even after sintering; the trabecular architecture is precise and there are not those splays at the contact points that are frequent in the Robocasting technique for example.
The structure has a very high resolution degree, thanks to the intrinsic properties of DLP technology.
These considerations remained valid throughout the entire inspection period.

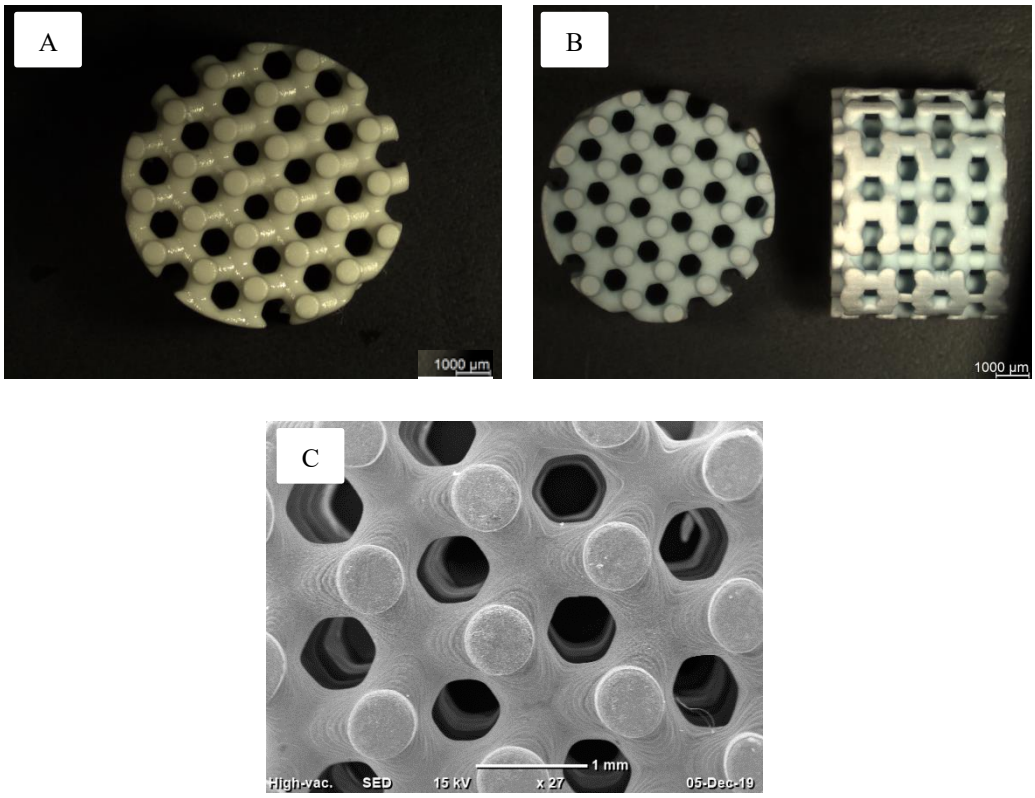

Figure 4. A) Cylinder before sintering; B) Cylinder after sintering; C) SEM Image of the porous architecture of cylinder.

4.2.6 Shrinkage Factors

The shrinkage factor was calculated using non-porous sintered test bars measuring 2×2.5×25 mm. The test involved the production of 18 bars, printed vertically with respect to the building platform, each bar consisting of 1251 layers, with a total printing time of 17 hours.
Five of the 18 printed bars were randomly? selected and measured along the three axes both before and after sintering in order to calculate the shrinkage factor caused by the high temperature thermal treatment.
Table 6 shows the theoretical dimensions of the bars, the lengths along the three axes, before and after sintering.

Table 6. Dimension of bars before and after sintering.

Fab-file	Before sintering	After sintering
X direction: 2 mm **Y direction: 2.5 mm** **Z direction: 25 mm**	Avg X direction: 2.61 Avg Y direction: 3.17 Avg Z direction: 31.19	Avg X direction: 2.16 Avg Y direction: 2.64 Avg Z direction: 25.11

The shrinkage factor was **1.206** along the x, y axes and **1.250** along the z axis.

A shrinkage of around 17% in xy directions and 19% in z directions were measured.
In this circumstance the shrinkage of the sample is low and above all, it is almost uniform in all three directions if we compare it to other studies found in literature, in which shrinkage of more than 30% was recorded [12]. This indicates that the sintered parts contract uniformly in the plane and there is not one direction more subject to stress than another.

4.3 Analysis of design specification for printing

The following tests aimed to study the feasibility of making objects with specific characteristics and a delicate 3D structure and to evaluate the printability of samples with pores of certain diameters and the strengths and weaknesses of the LithaBone 480E slurry.
In fact, depending on the material, different results could be obtained concerning the possibility of printing scaffolds with specific geometry.
Test as wall thickness, for example, allows to understand the capability to print thin or thick trabeculae and this is important when scaffolds with very thin trabeculae will be printed.
For every test described below, the same printing and post-printing parameters were used.

4.3.1 Wall Thickness

The term “wall thickness" literally means the distance between a surface and its opposite, and it is important to consider it to ensure that the final 3D trabecular structure is not formed by trabeculae that are too fragile and unsuitable for the printing parameters.
Figure 5 shows that both the green bodies with the smaller diameter and the green bodies with the larger diameter have no surface defects and the diameters corresponds to the theoretical ones of 1 mm and 10 mm, respectively. The same assessment can be extended to all cylinders in other dimensions.
After sintering, surface cracks appeared on all cylinders with a diameter d>3 mm.
This test indicates that a maximum feasible wall thickness is approximately equal to 3 mm.

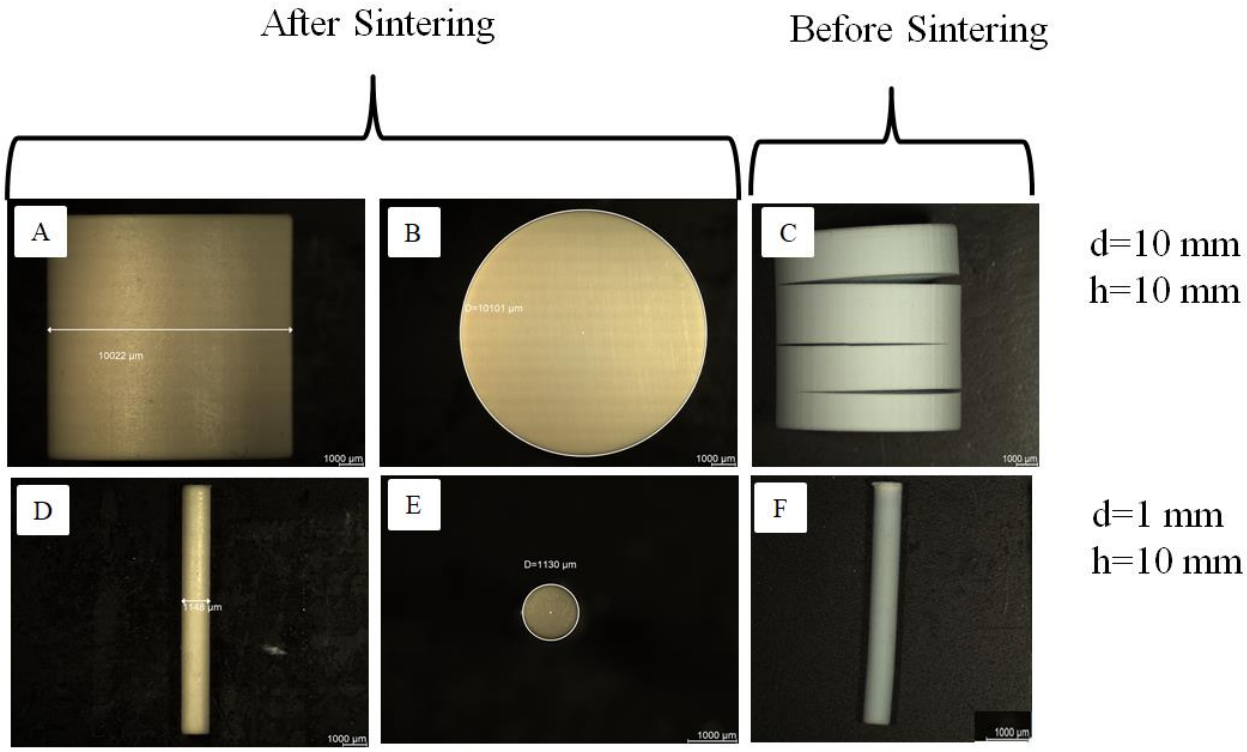

Figure 5. Wall thickness test: Cylinder d=1 mm h=10 mm and Cylinder d=1 mm h=10 mm Pre–sintering and Post–sintering. Images obtained with Opto S\N KL LCD optical microscope.

All fractured specimens have cracks parallel to the individual layers, and these increase as the wall thickness increases. This phenomenon is mainly due to the difficulty of the binder and other products of degradation to escape during sintering.

4.3.2 Aspect Ratio

The assessment of maximum aspect ratio was made on samples not yet sintered, to check for possible "blurring" due to a low level of stiffness of the slurry. The aspect ratio of the various samples varied from 10 (h=5 mm, d=0.833 mm) to 18 (h=15 mm, d=1.5 mm); particular attention was paid to samples with a high aspect ratio, as there is a greater possibility of finding defects as the aspect ratio increases. All components were analysed under the optical microscope and no defects were found on any type of sample. The maximum aspect ratio obtained was 18 and corresponded to the sample height of 15 mm and diameter/perimeter 0.833 mm.

Figure 6 shows the two samples with square base and cylindrical base of maximum aspect ratio.

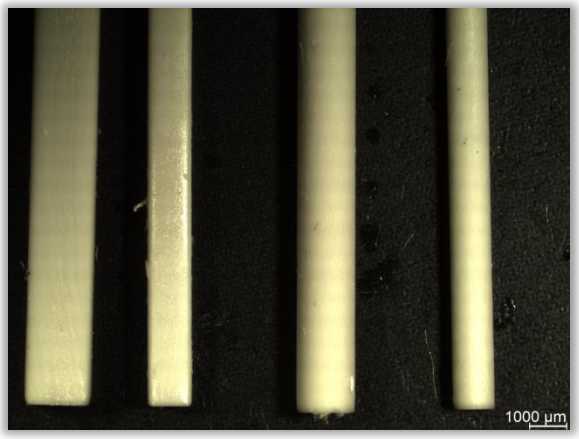

Figure 6. Samples with Aspect Ratio = 18.

This test confirms the satisfactory rigidity of the material and its suitability for printing fine structures with a high aspect ratio and without defects that could cause a low mechanical stability of the final structure.

4.3.3 Overhangs

The purpose of this test was to evaluate the achievability and printing limitations of overhangs and pores. Two equal samples were prepared to check the achievability of printing overhangs connected to a supporting structure on both sides and 2 samples to check overhangs that have only one point of contact with the supporting structure.
The samples, once printed and cleaned (Figure 7), were analysed under an optical microscope in their non-sintered state.

Figure 7. Overhangs test (green bodies).

4.3.3.1 H – Overhangs

Figure 8 shows overhangs with 0.5 mm and 1 mm length: in this case, the printing process was not successful as the actual thickness was different from the desired one. Moreover, 6 overhangs were almost fused into one. This was likely attributed to an excessive over-polymerization that did not allow to obtain the established dimensions.
On the other hand, longer overhangs were printed correctly; the only defect was found for the 4.5 mm long and 0.25 thick overhangs, which broke during the printing process.

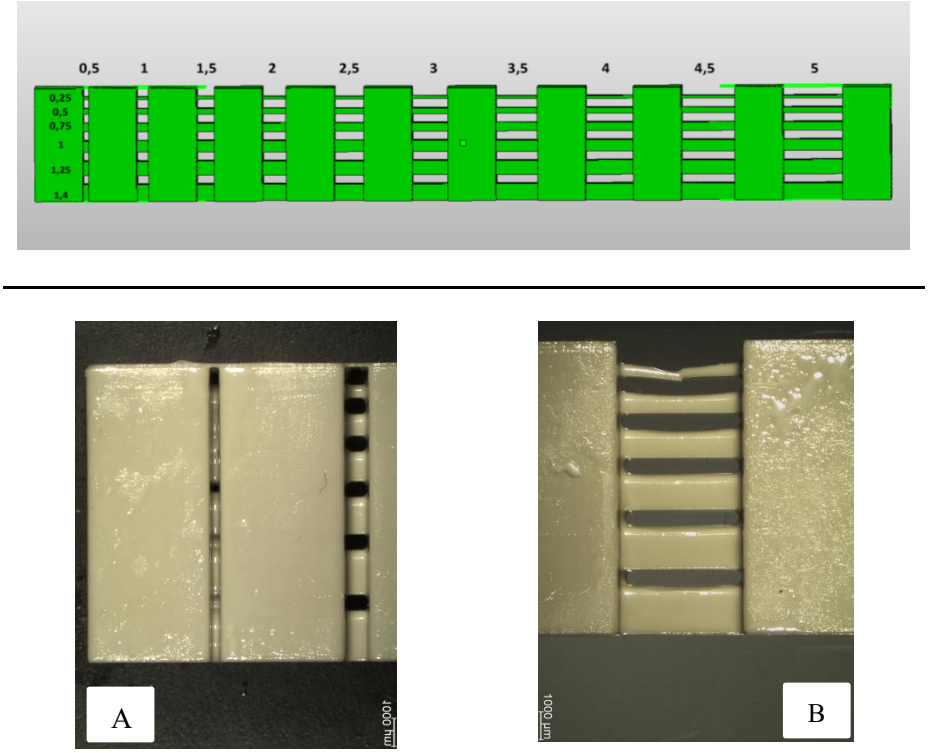

Figure 8. A) Overhangs measuring 0.5 mm; B) Overhangs measuring 4.5 mm.

4.3.3.2 T – Overhangs

Figure 9 shows that all the T-overhangs remained intact after being printed and after the uncured slurry removal. However, the longer overhangs, did not respect the theoretical thickness as it gradually increased closer to the ends.

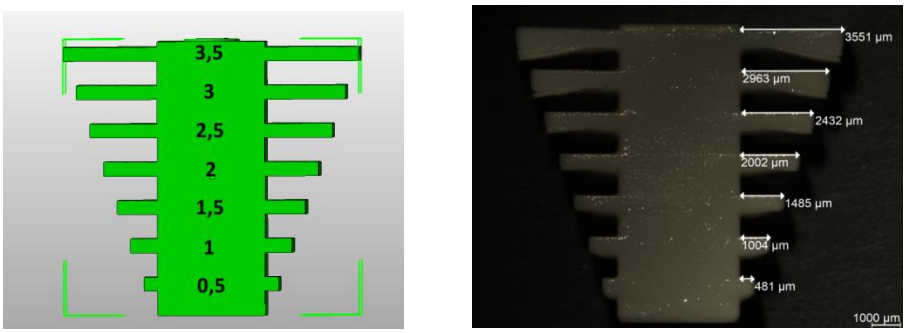

Figure 9. T – Overhang.

4.3.3.3 Diameter

Figures 10 show the larger diameter pores and the smaller diameter pores of the printing design. All pores larger than 0.5 mm in diameter were printed correctly, while the 0.5 mm diameter pore was completely occluded. This result may also be due to excessive over-curing and inaccurate removal of excess slurry during the cleaning procedure.

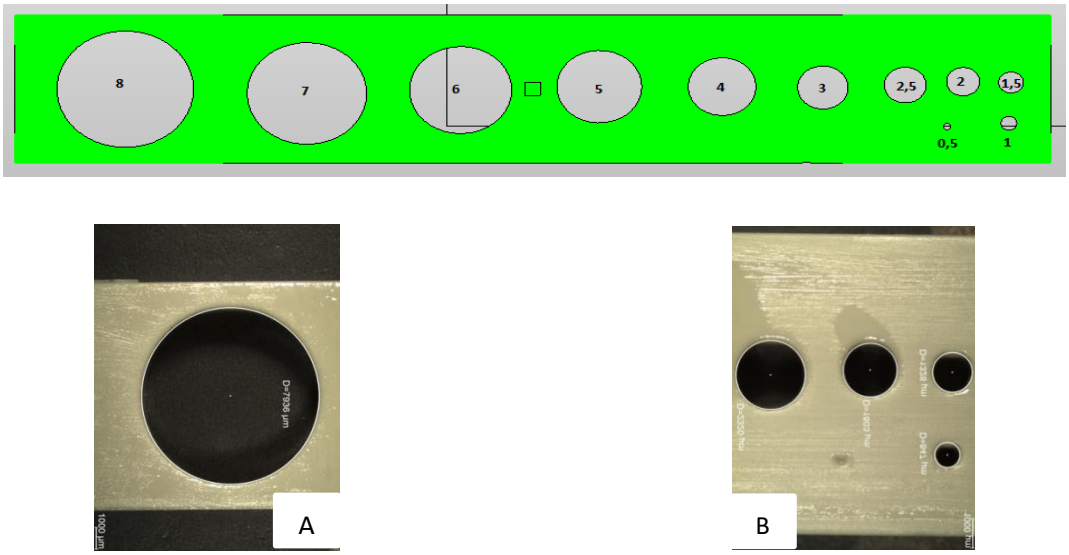

Figure 10. A) 8 mm diameter hole; B) Hole diameters from 0.5 to 2.5 mm.

4.3.4 Minimal Feature and over-polymerization

This test was performed to evaluate slurry over-polymerization during photopolymerization.
Light scattering effects can cause the curing of a larger area than that originally exposed to the DLP system [3].
Figure 11 shows the sample after being cleaned on the building platform and some details obtained with an optical microscope.

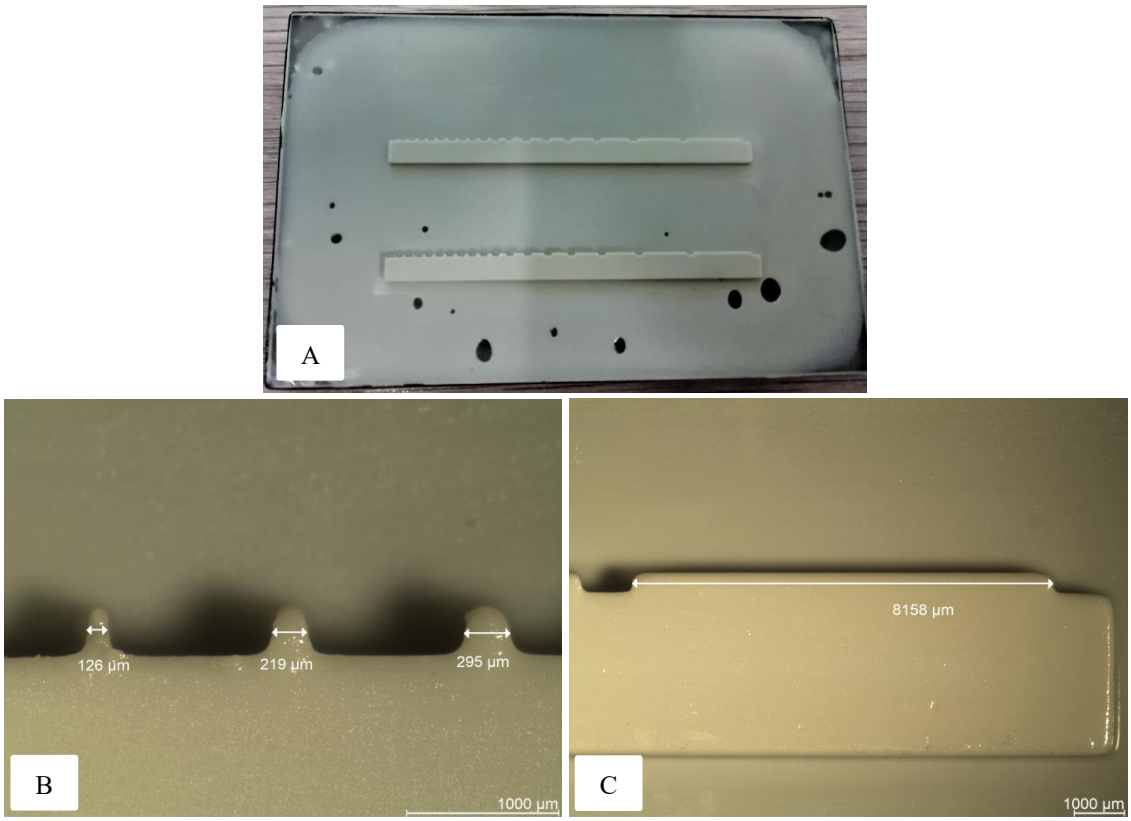

Figure 11. A) Minimal features test printed and cleaned from excess slurry directly on the building platform; B) Elements from 1 to 3 pixels; C) Element of 200 pixels.

The elements were almost double the theoretical width; for example, the first element (figure B) should have been about 40 µm wide. High levels of overpolymerization may be due either to a light intensity which was too high or to an excessive exposure time to light.
No incomplete or broken elements were recorded but they were blunted compared to the original design. The disappearance of peaks may be due to the cleaning process: in fact, due to the extreme fragility of the green body, surface defects to the structure may appear due to the use of an excessive amount of cleaning agent or air brush.

4.4 Analysis of samples

The results obtained from the LithaBone 480E slurry analysis confirmed that the suspension was appropriate for DLP process; it exhibited satisfactory and stable rheological characteristics and no excessive shrinkage. Most samples with a high wall thickness had surface cracks after sintering and some were even broken. On the contrary, better results were obtained for the printing of fine structures with a high aspect ratio and the printing of overhangs and holes of different diameters; in particular, there were no printing problems for holes of larger diameter ($d > 4$ mm), which were perfectly circular; even holes whose diameter was $1 \text{ mm} < d < 4$ mm were printed correctly. Only the hole of diameter $d = 0.5$ mm was completely occluded.

Once the analysis of the LithaBone 480E slurry was completed, the study moved on to the construction and the characterization of the scaffolds.

4.4.1 Hollow cylinders

Given that the results obtained in the wall thickness test indicated that it was impossible to print compact cylinders of diameter d>3 mm, we focused on the manufacture of dense hollow-cylindrical scaffolds with external diameter of 5 mm. .

Three different sets of hollow-cylinders were printed, each one including 45 samples composed of 500 overlapping layers. Each jobe required 6.49 h to be concluded. The dimensions and characteristics of the 3 different printed sets were:

1. Set 1: 45 cylinders h = 10 mm d = 5 mm; distance ext-int circumference = 1 mm
2. Set 2: 45 cylinders h = 10 mm d = 5 mm; = distance ext-int circumference =1.5 mm
3. Set 3: 45 cylinders h = 10 mm d = 5 mm; distance ext-int circumference = 2 mm

None of the 3 sets yielded satisfactory results; even cylinders in Set 1 (Figure 12), whose wall thickness was inferior, presented surface cracks post-sintering.

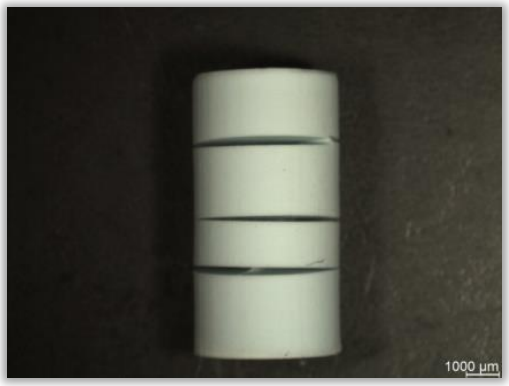

Figure 12. Sintered cylinder, Set 1: h = 10 mm d = 5 mm; distance ext-int circumference = 1 mm.

Figure 13 shows the SEM images of the fracture surface obtained.
As expected, the type of fracture is typical of fragile materials. The crack is clean and in line with the direction of construction of the layer.
A cross section of the cylindrical scaffold shows the layered structure typical of the layer-by-layer construction by DLP technology.

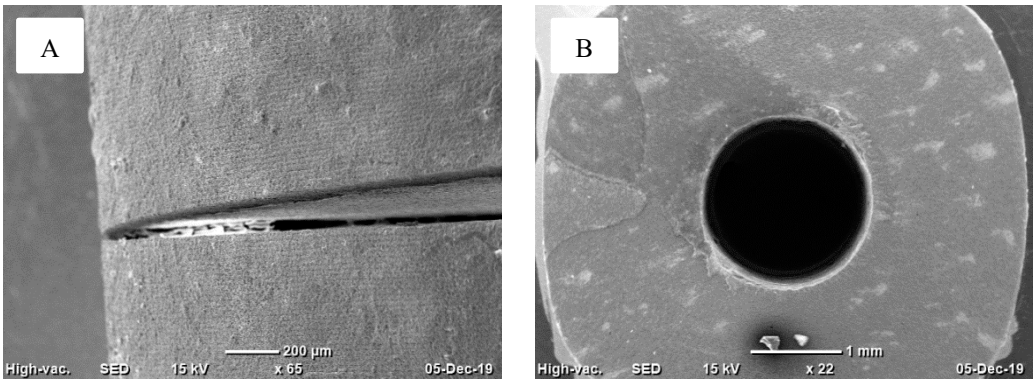

Figure 13. A) Details of the crack on the cylindrical sample; B) cross-section of the cracked cylinder. Images obtained from SEM analysis.

4.5 Characterization of porous scaffolds

4.5.1 Sponge-derived scaffolds

Figure 14 shows the main steps required for the production of porous-trabecular like scaffolds, from the processing of polyurethane foams µ-CTs images using InVesalius software, to the creation of the fab-file to be sent to the CeraFab 7500 machine, and finally to the printing of the scaffolds and their cleaning and sintering.

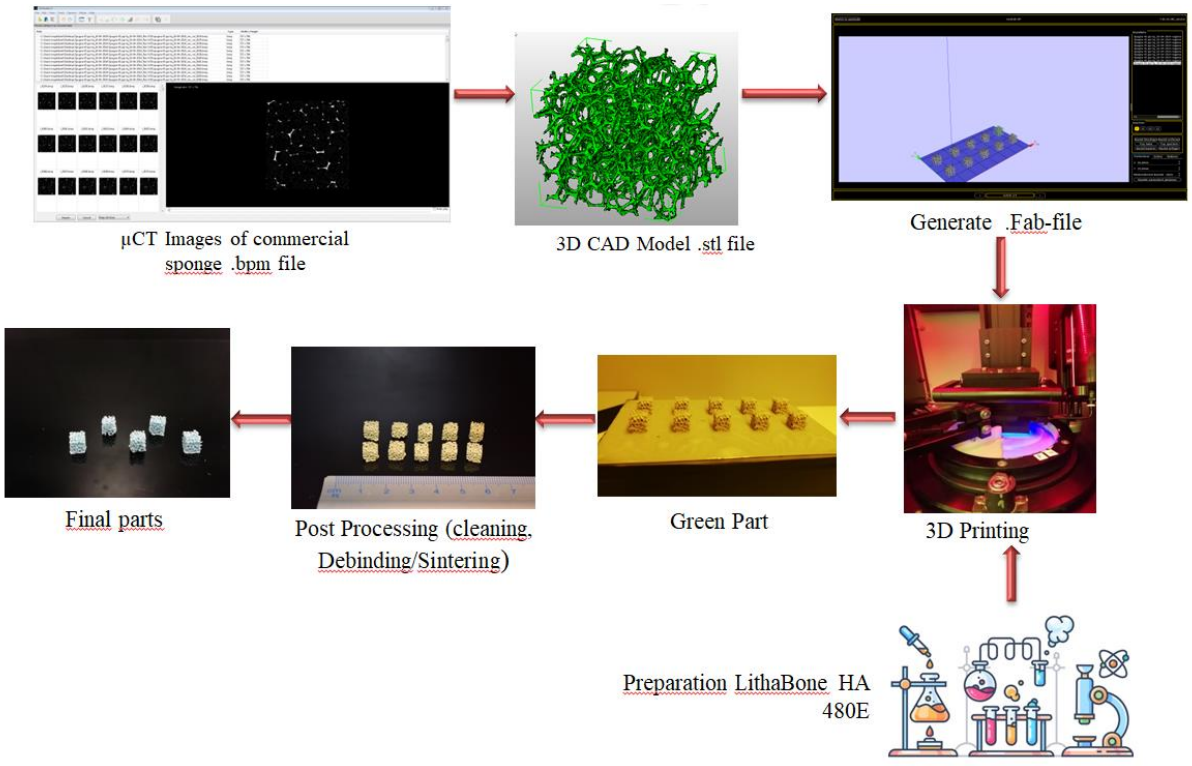

Figure 14. Main steps in the production of porous scaffolds.

We decided to use a CAD model for commercial sponge that simulates the trabecular architecture of spongy bone tissue.
Figure 15.A and B illustrate, respectively, an SEM image acquired with Benchtop SEM JEOL of the polymeric commercial sponge sample from which the μ-CTs image was obtained, and an SEM image of a human trabecular bone.

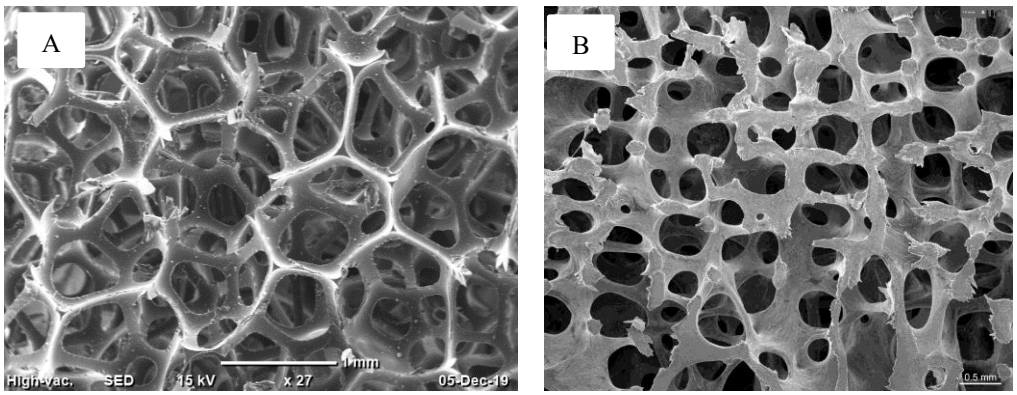

Figure 15. A) SEM image of the polymeric commercial sponge sample; B) SEM micrographs of natural cancellous bone [13].

In order to obtain a thickness of the scaffold trabeculae which was more similar to the thickness of the bone trabeculae, it was necessary to set the contouring to + 25 μm during the creation and fine-tuning of the CAD file. This not only served biomimetic purposes, but also ensured successful printing and a better mechanical response: such highly porous scaffolds with a fine trabecular architecture would otherwise risk breaking during the additive printing process and/or flake during cleaning.
Initially the dimensions of the cubic scaffolds produced were 4.72×5.15×5 mm; later, modifying the geometry of the initial CAD file, cylindrical scaffolds with an aspect ratio of 2:1 and dimensions 10×5 mm were printed.
Figure 16 shows the porous cubic and cylindrical scaffolds, just printed and not yet removed from the building platform, as well as various cylindrical and cubic scaffolds cleaned from excess slurry. A total of 30 cubic and 90 cylindrical scaffolds were printed.

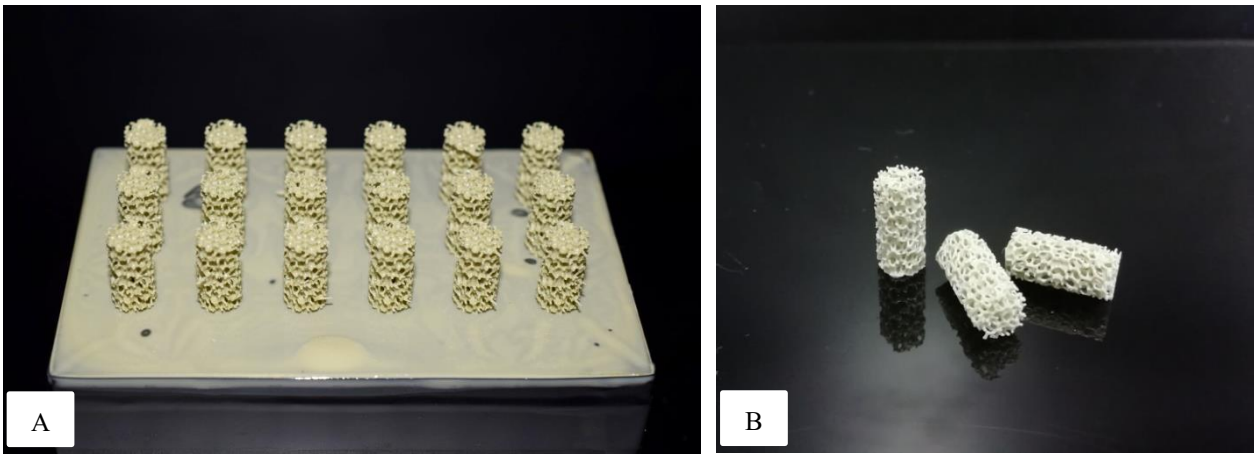

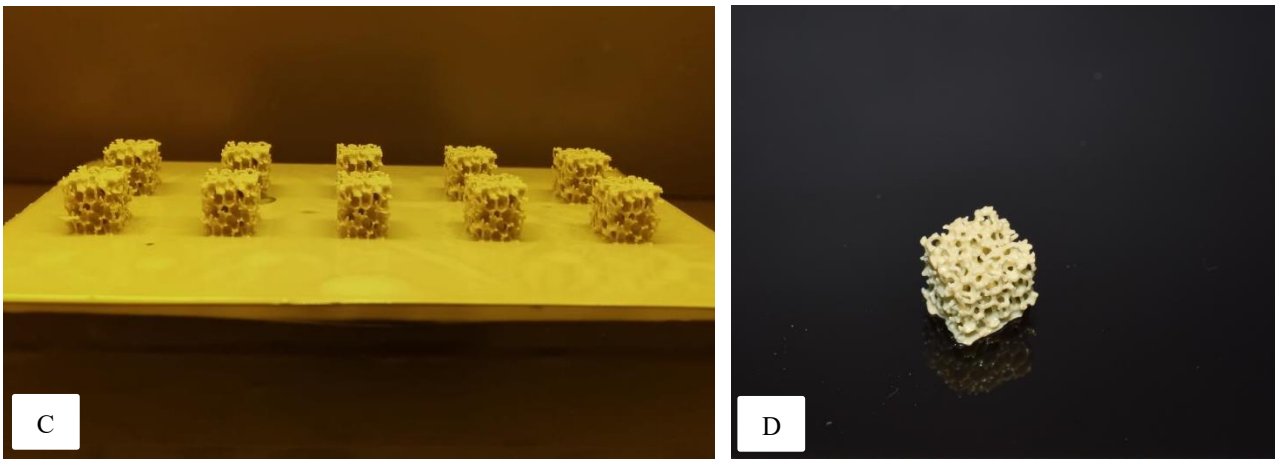

Figure 16. A) Cylindrical scaffolds on the building platform; B) Various samples of cylindrical scaffolds after having been cleaned from the uncured slurry; C) Cubic scaffolds on the building platform, D) Cubic scaffold after having been cleaned of excess uncured slurry.

Despite their high porosity, the scaffolds withstood the printing process and no samples detached from the building platform.

Figure 17 illustrates the trabecular structure of the scaffolds in more detail: it may be noted that the walls of the samples are extremely thin and, consequently, the unsintered scaffolds are extremely fragile. Due to their intrinsic fragility, the green bodies were difficult to manipulate, requiring a great deal of attention and caution during the cleaning process. Despite this, most of the uncured slurry was successfully removed using compressed air in combination with a cleaning agent, and no defects were present after cleaning.

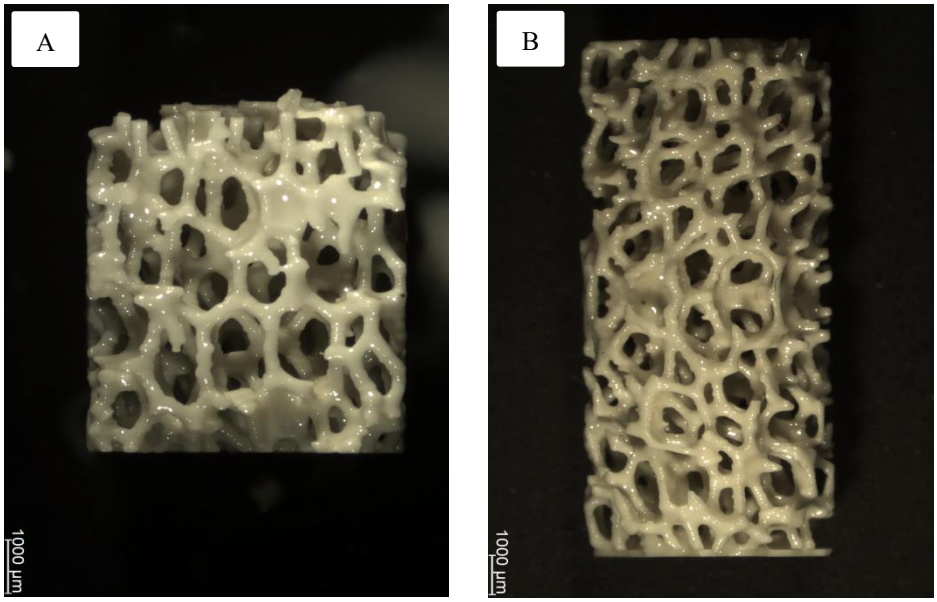

Figure 17. Images of cubic (A) and cylindrical scaffolds (B) obtained with optical microscope Opto S\N KL LCD.

Figure 18 shows the final scaffolds after 99 h of sintering.
Neither of the two different scaffold geometries showed cracks or other surface defects, thanks to the high porosity of the scaffold; the binder evaporated easily during sintering, without causing stress to the structure and increases in pressure.

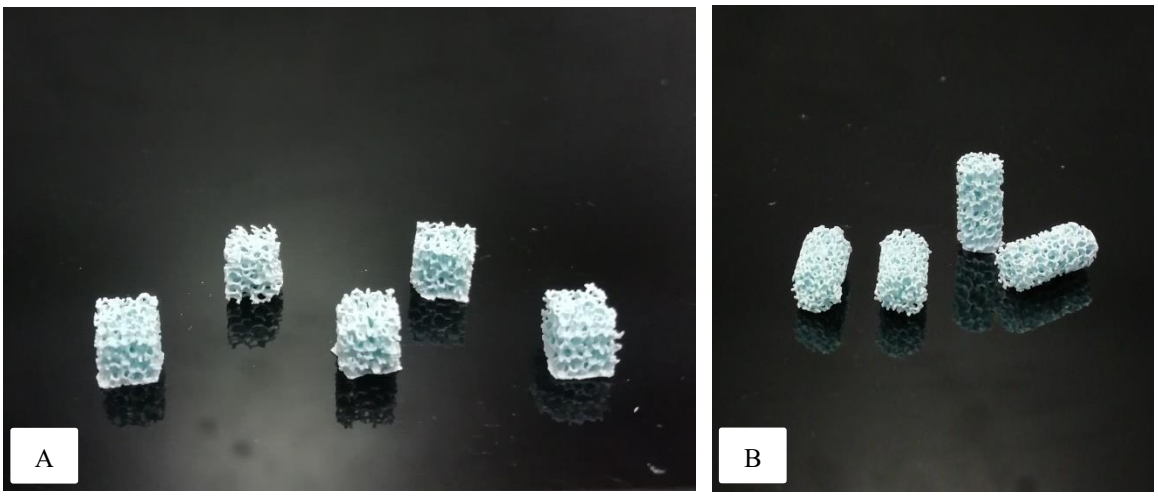

Figure 18. A)Sintered cubic scaffolds ; B) cylindrical scaffolds.

4.5.2 XRD Analysis-Assessment of Crystalline Phases

For the XRD analysis, some of the scaffolds produced were crushed to obtain a fine, homogeneous powder. The properties of the HA sintered powder were checked using a PANalytic diffractometer with Bragg-Brentano chamber in order to identify the crystalline phase of the powder and the possible formation of new phases due to the sintering process.
Figure 19 shows the XRD pattern obtained for the commercial HA powder used in this study after the sintering process and Table 7 summarizes the main features of the crystalline phase detected.

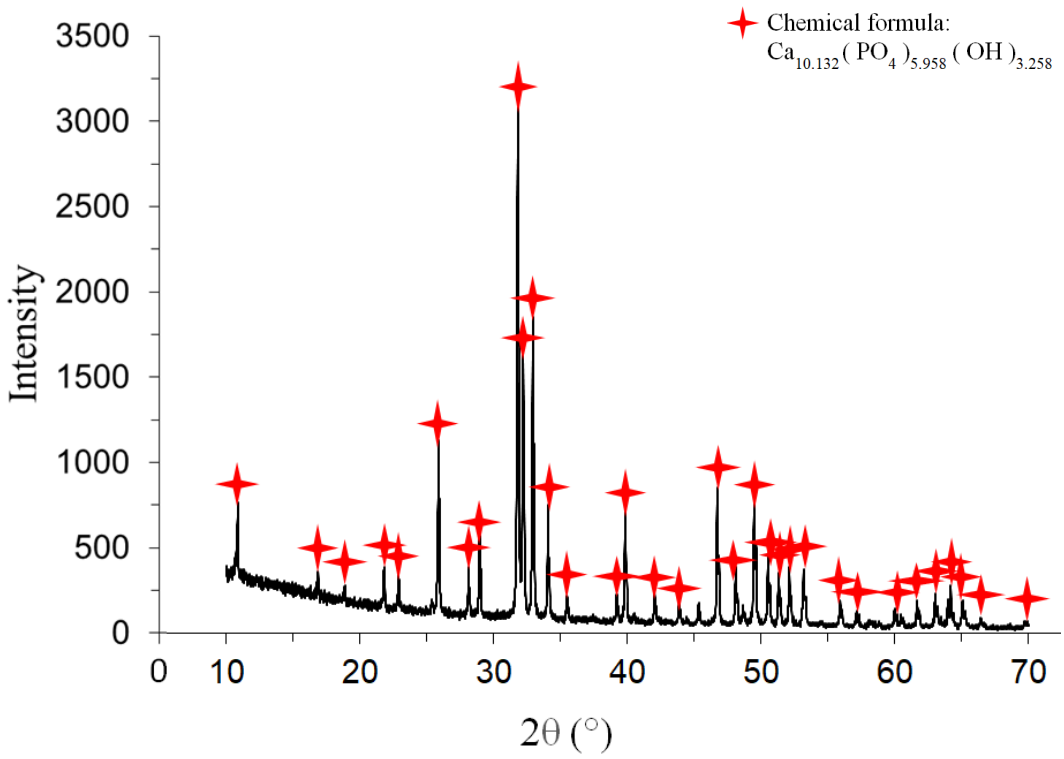

Figure 19. X-ray spectrum related to sintered HA powders utilized for scaffold production.

HA (ref. code 01-089-6439) was the only crystalline phase detected in the sample.
No new phase formed after sintering, and maintaining a temperature of 1300 °C for 2 h did not cause any dissociation of HA in TCP. The spectrum has distinct peaks and notes, indicating a material with a high crystalline content.
No impurities, traces of CaO or calcium phosphate phase residues were identified.

Table 7. Features of HA phase obtained by XRD analysis.

Name and Formula	
Reference Code	01-089-6439
Mineral name	Hydroxylapatite, syn
ICSD name	Calcium Phosphate Hydroxide
Empirical formula	$Ca_{10.132}H_{3.258}O_{27.09}P_{5.958}$
Chemical formula	$Ca_{10.132}(PO_4)_{5.958}(OH)_{3.258}$
Crystallographic parameters	
Crystal system	Hexagonal
Space group	P63/m
Space group number	176
Calculated density (g/cm^3)	3.23
Volume of cell (10^6 pm^3)	528.39
Quality	Calculated (C)

It is reported that high sintering temperatures allow to obtain a better crystalline quality, here confirmed by the high intensity of the characteristic peaks of the material. As reported in the study conducted by Zeng et al., HA sintered at low temperatures, t would not exhibit the typical diffraction peaks of the material. However, the same study states that too high sintering temperatures (T= 1250 °C) could lead to the dissociation of a portion of HA in α-TCP and β-TCP [12].
In the present work this phenomenon was not observed likely due to a good and precise slurry preparation and the high purity of starting HA powders [14]. Although α- TCP and β-TCP are resorbable and biocompatible, a single phase of HA has to be preferred because the presence of β-TCP could lead to the formation of CaO which is highly toxic [14].
In addition, the LithaBone 480E scaffold was already highly porous and thin, so it is reasonable to assume a suitable degradation rate for BTE applications. However, in vitro degradation tests would be necessary in order to confirm this theory.

All components of the organic matrix disappeared during sintering; this is highly advantageous as it limits the risk of cytotoxicity problems often linked to binder components [15].

4.5.3 Scanning Electron Microscopy (SEM)-Morphological Assessment

The morphological features of HA-scaffolds were assessed by SEM analysis (Benchtop SEM JEOL), paying special attention to pore morphology and interconnectivity, their size and the thickness of the trabeculae.
The morphology of the scaffold surface, the architecture of the pores and trabeculae are visible in figure 20.

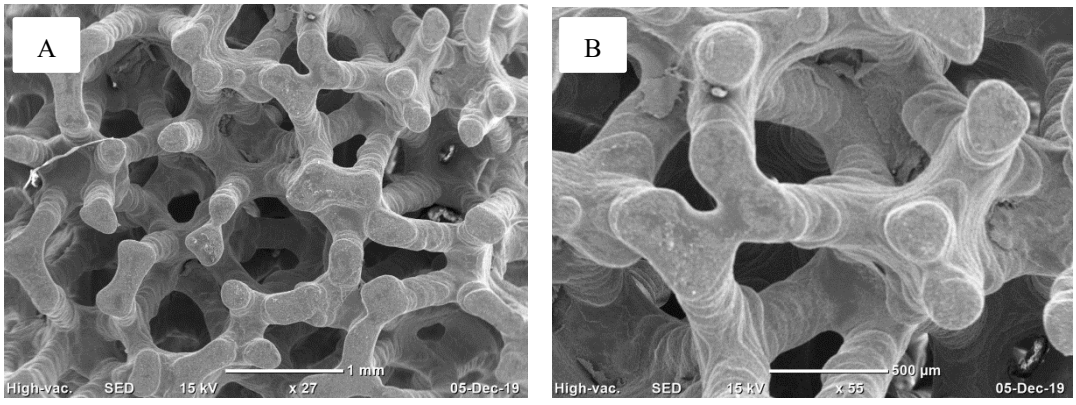

Figure 20. Images of the porous architecture of the scaffolds, obtained with Benchtop SEM JEOL: A) x27; B) x55.

Figure 20. A) shows a highly interconnected open-cell architecture; the samples had an open-cell structur, faithful to that of the starting CAD model, with a 3D dimensional interpenetrating network of pores and struts.

The average pore diameter size was **200-300 µm**; some pores have a larger diameter of up to **800 µm.**
It is recognized that scaffolds with 300 µm pores have a good balance between surface area and diffusion, supporting bone mineralization and blood vessel infiltration [13].
A pore diameter of 200-500 µm is considered to be the optimal measure to ensure osteoconduction and new bone formation of the trabecular and Hanversian types.
Table 8 shows some examples found in the literature where scaffolds with pore sizes between 200-500 µm speed up and improve the growth and mineralization of new bone tissue.

Table 8. Selection of scientific studies on the influence of bone growth in scaffolds with pores in the range between 200-500 µm.

References	**Authors**	**Aim**
[16]	E. Tsuruga, H. Takita, et al.	A HA Block with pore size of 300-400 µm results to have the optimal pore size for attachment, differentiation and growth of osteoblasts and vascularization.
[17]	J. Henkel, M. Woodruff, et al.	Pore interconnections and pores are prefferred to be at least 300 µm in diameter to allow sufficient scaffold vascularisation.
[18]	R.Perez, G.Mestres	Bigger pore size (>400 µm) allows a correct vascularization; pores < 400 µm allows the growth of fibrous tissue.
[19]	C. Murphy, M. Haugh	The better pores size for the adesion and proliferation of osteoblasts is > 300 µm
[20]	R. LeGeros	The best pore size of porous HA block to promove the bone formations is 300-400 µm

Pores of larger diameter, on the other hand, are considered unfavourable to the new formation of bone tissue and not suitable to ensure sufficient mechanical properties [21].
Despite this, an *in vivo* study conducted in 2006 by Von Doernberg et al., proved that scaffolds with random pore size distribution from 500 µm to 1200 µm promote bone regrowth [22].
A more recent study, focusing on the production of TCP-based scaffolds with DLP based on SLA and using the same CeraFab 7500 machine (Lithoz GmbH) used in this thesis work, shows that scaffolds with pore diameters between 700 µm and 1200 µm have good osteoconductivity properties *in vivo*. These scaffolds, however, unlike those made by Von Doernberg et al, have an organized microarchitecture, and a non-random pore distribution [21] .

In any case, a maximum pore diameter limit has not yet been definitively confirmed [21]. In the future, it would be desirable to implant pre-osteoblastic cells *in vitro* to control the osteogenic and osteoconductive properties of scaffolds with random pore diameter distribution between 200-800 μm.
Figure 20.B) shows details of the trabeculae forming the scaffold. They are full, homogeneous and approximately round in shape.
Figure 21 shows a visually compact microstructure, as can be seen from the minimal presence of intergranular pores. The ceramic particles are closely compacted, indicating a successful sintering of the scaffold.

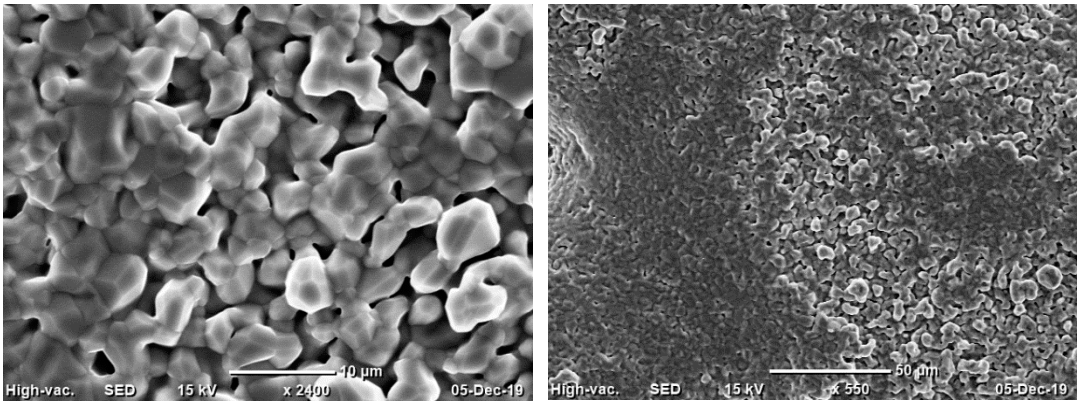

Figure 21. SEM Images of scaffolds surface (X 2400 and X 550).

4.5.4 Energy Dispersive Spectroscopy (EDS)- Compositional assessment

An EDS test was performed to evaluate the elemental composition of the scaffold in LithaBone 480E and to verify the correspondence between its actual and theoretical composition, checking for the absence of contaminants.
The composition of the scaffold was studied in five different areas to calculate the Ca/P ratio (Figure 21).
Table 9 summarises the atomic Ca/P ratio calculated for the five areas considered.
The average value in the five areas considered was **1.89 ± 0.092**, which is higher than the atomic ratio of stoichiometric HA (1.67); this is not surprising, however, because EDS underestimates P and the scaffold was produced using a commercial HA powder.
EDS analysis proved that no contaminants were introduced during the processing and the post-processing of the material, supporting the high reliability and the suitability of the whole manufacturing process for the production of highly standardized grafts for medical applications.

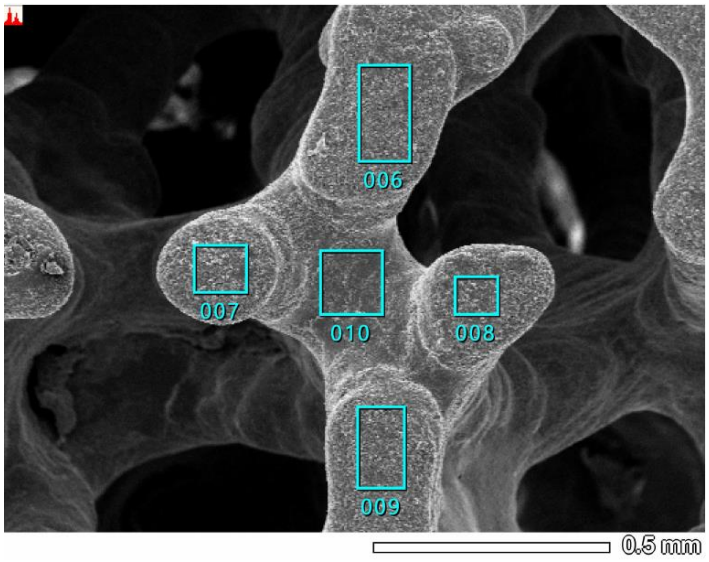

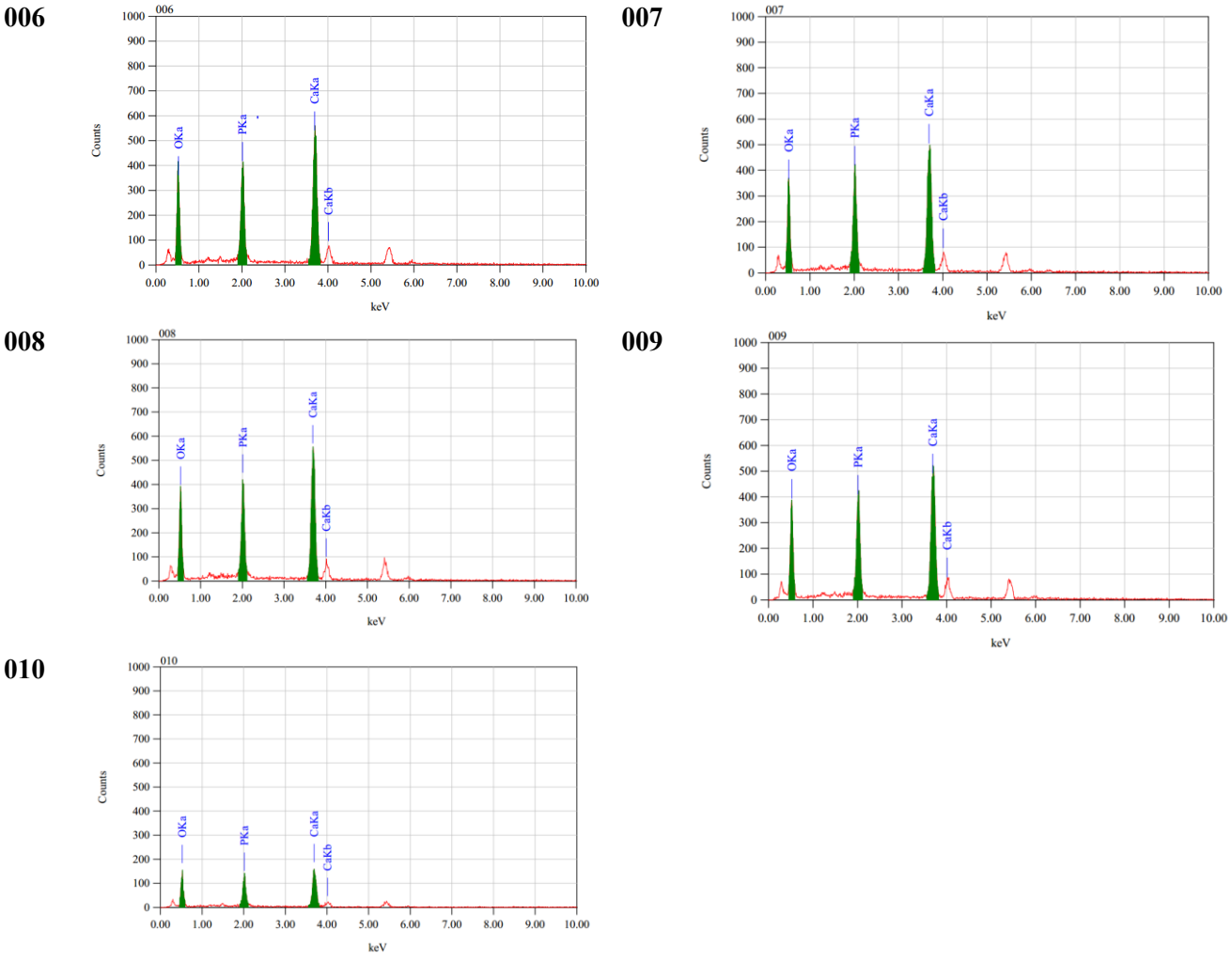

Figure 21. Compositional analysis of the LithaBone 480E scaffold using benchtop SEM.

Table 9. Ca/P atomic ratio relative to the five areas considered for the scaffold.

Area	Element	Atomic %	Ca/P atomic ratio
006	Ca	18	1.97
	P	9.15	
007	Ca	17.83	1.90
	P	9.35	
008	Ca	18.44	1.98
	P	9.30	
009	Ca	18.02	1.88
	P	9.56	
010	Ca	15.87	1.75
	P	9.07	
Averaged value: Ca/P atomic ratio=1.89 ± 0.092			

Conclusion

The present thesis work has been carried out in Lithoz GmbH (Austria) and then in DISAT laboratory of the Politecnico di Torino (Italy), due to obtain and characterized porous ceramic scaffolds which can accurately reproduce the porous and interconnected structures of the cancellous human bone.

Thanks to the CeraFab system based on DLP process, 120 porous scaffolds were obtained (30 cubic scaffolds and 90 cylindrical scaffolds).

During the stay in Lithoz, much management has been dedicated to the definition of the slurry composition (LithaBone 480E) and its characterization. In particular, slurry stability was carefully evaluated over a period of 5 weeks, monitoring rheological properties (η=13.3 Pa·s at T=25 °C, and η=7.7 Pa·s at T=40°C), relative density (ρ_r = 88 ± 0.61%), maximum bending strength (60.86 ± 5.4 MPa) and agglomeration tendency of suspended ceramic particles.

Microstructural, compositional and morphological characterization of HA scaffolds was carried out at the DISAT laboratory of the Politecnico di Torino. HA was the only crystalline phase detected by X-ray diffraction (XRD), proving that no phase transitions occurred upon high temperature sintering treatment.

Scanning Electron Microscopy (SEM) morphological analysis revealed the presence of highly interconnected macropores in the range 200-800 μm; minimal interstitial porosity was observed, thus indicating that a good sintering level was achieved, fundamental to ensure good mechanical performances. Ca/P atomic ratio was 1.89 ± 0.092, really close to the stoichiometric one.

References

[1] E. Schwarzer, M. Götz, D. Markova, D. Stafford, U. Scheithauer, and T. Moritz, "Lithography-based ceramic manufacturing (LCM) – Viscosity and cleaning as two quality influencing steps in the process chain of printing green parts," J. Eur. Ceram. Soc., vol. 37, no. 16, pp. 5329–5338, 2017.

[2] Y. Li, C. P. A. T. Klein, X. Zhang, and K. de Groot, "Relationship between the colour change of hydroxyapatite and the trace element manganese," Biomaterials, vol. 14, no. 13, pp. 969–972, 1993.

[3] G. Mitteramskogler et al., "Light curing strategies for lithography-based additive manufacturing of customized ceramics," Addit. Manuf., vol. 1, pp. 110–118, 2014.

[4] C. Schmidleithner, "Master Thesis Additive Manufacturing of Tricalcium Phosphate Scaffolds for Bone Tissue Engineering," Vienna University of Technology.

[5] Lithoz GmbH, "Lithoz Available Materials." Austria, pp. 1–9, 2019.

[6] Z. Liu et al., "Additive manufacturing of hydroxyapatite bone scaffolds via digital light processing and in vitro compatibility," Ceram. Int., vol. 45, no. 8, pp. 11079–11086, 2019.

[7] C. Feng et al., "Additive manufacturing of hydroxyapatite bioceramic scaffolds: Dispersion, digital light processing, sintering, mechanical properties, and biocompatibility," J. Adv. Ceram., vol. 9, no. 3, pp. 360–373, 2020.

[8] F. Scalera, C. Esposito Corcione, F. Montagna, A. Sannino, and A. Maffezzoli, "Development and characterization of UV curable epoxy/hydroxyapatite suspensions for stereolithography applied to bone tissue engineering," Ceram. Int., vol. 40, no. 10, pp. 15455–15462, 2014.

[9] Y. Yao, N. Sha, and Z. Zhao, "Highly Concentrated Hydroxyapatite Suspension for DLP Printing," IOP Conf. Ser. Mater. Sci. Eng., vol. 678, no. 1, pp. 1–8, 2019.

[10] R. W. Davidge, "Mechanical Properties Of Ceramic Materials," Contemp. Phys., vol. 10, no. 2, pp. 105–124, 1969.

[11] P. D. Beattie and J. M. Bishop, "Characterization of Porous Hydroxyapatite," J. Intell. Robot. Syst. Theory Appl., vol. 22, no. 3–4, pp. 255–267, 1998.

[12] Y. Zeng et al., "3D printing of hydroxyapatite scaffolds with good mechanical and biocompatible properties by digital light processing," J. Mater. Sci., vol. 53, no. 9, pp. 6291–6301, 2018.

[13] "Normal Bone - Bone Research Society." [Online]. Available: https://boneresearchsociety.org/resources/gallery/12/#top. [Accessed: 04-Jun-2020].

[14] F. Gervaso, F. Scalera, S. Kunjalukkal Padmanabhan, A. Sannino, and A. Licciulli, "High-performance hydroxyapatite scaffolds for bone tissue engineering applications," Int. J. Appl. Ceram. Technol., vol. 9, no. 3, pp. 507–516, 2012.

[15] F. P. W. Melchels, J. Feijen, and D. W. Grijpma, "A review on stereolithography and its applications in biomedical engineering," Biomaterials, vol. 31, no. 24, pp. 6121–6130, 2010.

[16] E. Tsuruga, H. Takita, H. Itoh, Y. Wakisaka, and Y. Kuboki, "Pore size of porous hydroxyapatite as the cell-substratum controls BMP-induced osteogenesis," J. Biochem., vol. 121, no. 2, pp. 317–324, 1997.

[17] J. Henkel et al., "Bone Regeneration Based on Tissue Engineering Conceptions-A 21st Century Perspective," Bone Res., vol. 1, pp. 216–248, 2013.

[18] R. A. Perez and G. Mestres, “Role of pore size and morphology in musculo-skeletal tissue regeneration,” Mater. Sci. Eng. C, vol. 61, pp. 922–939, 2016.
[19] C. M. Murphy, M. G. Haugh, and F. J. O’Brien, “The effect of mean pore size on cell attachment, proliferation and migration in collagen-glycosaminoglycan scaffolds for bone tissue engineering,” Biomaterials, vol. 31, no. 3, pp. 461–466, 2010.
[20] R. Z. LeGeros, “Properties of osteoconductive biomaterials: Calcium phosphates,” Clin. Orthop. Relat. Res., no. 395, pp. 81–98, 2002.
[21] C. Ghayor and F. E. Weber, “Osteoconductive microarchitecture of bone substitutes for bone regeneration revisited,” Front. Physiol, vol. 9, pp. 1–10, 2018.
[22] M. C. von Doernberg et al., “In vivo behavior of calcium phosphate scaffolds with four different pore sizes,” Biomaterials, vol. 27, no. 30, pp. 5186–5198, 2006.

Chapter 5

Conclusions and future developments

The aim of this thesis work was the realization of standardized and highly reproducible porous HA scaffolds for bone tissue engineering applications.
The first part of the thesis work was carried out at Lithoz GmbH, an Austrian company located in the capital, Vienna.
The activity at Lithoz mainly focused on the production of both dense and porous, highly-performant ceramic structures by Digital Light Processing (DLP) based on stereolithography (SLA) technology.
Differently from classic SLA, based on a point-to-point UV laser irradiation that creates a predefined structure, DLP technology uses a blue light source in the visible and a DMD (digital mirror device) chip as a dynamic mask to polymerize one layer at a time. In this way, the manufacturing of the scaffold occurs more rapidly without loss of resolution by polymerizing a photosensitive suspension composed of ceramic particles homogeneously dispersed within an organic matrix containing reactive monomers and a solvent. The chain reaction, which takes place over a short period of time, forms the desired matrix of monomers capable of binding the ceramic particles and forming the so-called "green body".
The CeraFab 7500 was the machine utilized for this process; it actually represents the first commercially-available printer (Lithoz GmbH) with a resolution of 5 μm to 100 μm along the z-axis and 40 μm along the x, y-direction.
The possibility to process biocompatible, bioreabsorbable and osteoconductive ceramic materials, such as HA and TCP, as well as the opportunity to create mechanically resistant 3D structures with a high resolution while optimizing working time and quantity of material, make this manufacturing approach really appealing in BTE field. HA ($Ca_{10}(PO4)_6(OH)_2$)) is known to be one of the most thermodynamically stable CaPs upon processing and with high capacity to create a strong bond with natural bone in physiological conditions.
In this context, HA commercial powders, conform to the ASTM F1085 – 03 specification for hydroxyapatite as implant material, were used as starting material for scaffold manufacturing.
The new LithaBone 480E slurry was developed at Lithoz GmbH and its main properties and time-dependent behavior were investigated.
A 5-week "Stability tray test" job was set up to investigate the rheological properties of the uncured slurry, maximum grind size, as well as its relative density and ultimate tensile strength..
A fab-file stability trays was used to print 7 bars, 4 cubic samples and 2 cylinders with ordered porous architecture.

Ceramic bars were produced for the 3-point bending strength test (ultimate tensile strength), cubic samples for the density test and the porous cylinders to check the feasibility of printing porous samples without defects.
However, after sintering, cuboid specimens, showed more severe surface cracks with respect to sintered bars; for this reason, it was decided to use compact bars for both density and flexural tests.
The porous samples, on the other hand, did not show any kind of defect even over the course of the weeks, thus proving the suitability of the tested slurry to be used for DLP-based printing of porous 3D architectures.
The viscosity of the slurry, measured by RCM Rotational Rheometer, was found to be 13.3 Pa·s and 7.7 Pa·s at T=25 °C and T=40°C, respectively.
The fineness of grind was also determined by grindometer test by checking the presence of large dispersed particles or agglomerates . The maximum grind size detected was 6 μm; as the size did not change over the weeks, the intrinsic stability of the suspension, and, in particular, the tendency of ceramic particles not to agglomerate were confirmed.
Using the Archimedes method, the relative density was measured: this was $\rho_r = 88 \pm 0.61\%$ and porosity was 12 %.
This density was lower than other results obtained in the literature, but in this case, the result may have been compromised by the presence of cracks on the surface of the specimens. The same consideration can also be made for the results obtained during the 3-point bending strength test in which an average Ultimate Tensile Stress of 60.86 ± 5.4 MPa was calculated.
In order to assess the shrinkage factor, non-porous sintered test rods of 2×2.5×25 mm were used; the shrinkage factor was found to be 1.206 along the xy axes and 1.250 in z axis.
The results obtained from the LithaBone 480E slurry analysis confirmed the suitability of the suspension for DLP printing process; indeed, it exhibited satisfactory and stable rheological characteristics and no excessive shrinkage upon heating.
Most of the samples with a high wall thickness revealed evident surface cracks after sintering, leading sometimes even to the complete breakage of the structure. In contrast, better results were obtained when fine structures with a high aspect ratio were printed, as well as when printing overhangs and holes of different diameters.
The design of the finale trabecular-like porous scaffolds was based on a CAD model created by reconstructing μ-CTs images of an open-cell commercial polymeric sponge.
The objective was the printing of cubic and cylindrical geometry (with aspect ratio 2:1) able to imitate the specific characteristics of bone tissue, in order to obtain a heterogenic geometry that would result in a structure biomimically similar to the trabecular architecture of the spongy bone.
The InVesalius software was used to create the CAD file of the sponge with cubic geometry and size 4.72×5.15×5 mm; then a second file was created to print cylindrical scaffolds with aspect ratio 2:1 and size 10×5 mm.
A total of 30 cubic scaffolds and 90 cylindrical scaffolds were printed.
Despite the high theoretical porosity derived from the initial CAD file (>80%), the scaffolds resisted the printing process and there was no sample detachment from the building platform.
The green bodies underwent a sintering process conducted in a Nabertherm P330 furnace for 99 h at a variable temperature speed between 0.42 and -1.62 K/min. The maximum sintering temperature of 1300 °C was maintained for 2 hours.

The scaffolds were then characterized at the DISAT laboratory of the Politecnico di Torino by X-ray diffraction (XRD), scanning electron microscopy (SEM) and energy dispersion spectrometry (EDS) to assess crystalline phases, morphological features and elemental composition, respectively.
XRD analysis confirmed the presence of a highly crystalline HA phase as the only crystalline phase within the material, thus proving that sintering at high temperatures did not cause any kind of chemical modifications and phase transitions.
SEM morphological analysis revealed a compact microstructure and minimal presence of intergranular pores, an indication of successful sintering. The scaffold had an average pore size between 200-300 μm to 800 μm. An atomic ratio Ca/P =1.89 ± 0.092 was calculated from the EDS analysis, very similar to that of stoichiometric HA.

On the basis of the results obtained, further studies deserve to be carried out in order to:

- Evaluate the mechanical properties of the scaffolds by investigating their compressive strength and overall reliability of the manufacturing process by determining the Weibull modulus in compression loading mode.

- Conduct bioactivity and degradability tests in SBF (Simulated Body Fluid) and Tris-HCl buffer solution, respectively, in order to predict the *in vitro* bioactivity of the scaffolds and evaluate the degradation rate in contact with the physiological environment.

- Investigate the biological properties of the scaffold and the cellular rooting capacity by *in vitro* cellular tests.

- Further optimize the printing parameters and the slurry formula, and especially improve the binder composition in order to avoid the formation of surface cracks after sintering.
  Indeed, it is strongly believed that a deeper knowledge of slurry behavior under the effect specific printing parameters could be helpful in managing material behavior upon high temperature thermal treatments, thus improving the performance of the final scaffold.

Ringraziamenti

Desidero esprimere la mia più sincera gratitudine al Professor Francesco Baino e alla Professoressa Enrica Verné per avere dimostrato sin dal primo giorno estrema disponibilità, aiuto e fiducia nei miei confronti, e soprattutto per avermi dato la possibilità di svolgere questo lavoro di tesi che mi ha permesso di crescere sia in ambito lavorativo che umano.
Un grosso grazie va alla Dott.ssa. Elisa Fiume che mi ha accompagnata per tutto il lavoro svolto presso il laboratorio DISAT e per tutto il periodo di scrittura tesi, ma anche per aver permesso che si creasse un rapporto di stima al di là dell'ambito lavorativo, per i numerosi e preziosi consigli e per l'estrema pazienza che ha sempre dimostrato durante tutto il progetto.
A loro devo un sentito riconoscimento per avermi insegnato che il duro e meticoloso lavoro alla fine ripaga, che le sfide vanno colte e che se la strada è lunga e frastagliata allora è quella giusta!

Vorrei ringraziare di cuore il Dr. Martin Schwentenwein per avermi dato la straordinaria possibilità di lavorare in un ambiente dinamico, efficiente e stimolante come Lithoz. L'esperienza trascorsa in azienda è stata una delle più belle che mi siano capitate e farò tesoro di tutto ciò che mi è stato gentilmente insegnato.

Un grazie particolare va a Patricia che con pazienza e disponibilità mi ha accompagnato per tutto il periodo di lavoro in Lithoz. Sempre dolce e disponibile con me, le sono enormemente grata per tutto l'aiuto che mi ha dato. Spero che in futuro le nostre strade si rincroceranno…

Il più grande ringraziamento va alla mia famiglia: Babbo, Mamma, Simone.
Le mie colonne portanti, la mia forza e la mia più grande soddisfazione.
A loro dedico tutto.

"Stay hungry, stay foolish"

Steve Jobs, Stanford University, 2005